UNIVERSITÄT OSNABRÜCK

Department of Physics

Influence of growth conditions on magnetic, electronic and structural properties of ultrathin Co-based oxide films

Kevin Ruwisch, M.Sc.

Dissertation (kumulativ)

zur Erlangung des Doktorgrades (Dr. rer. nat.)

vorgelegt am Fachbereich Physik der Universität Osnabrück

Osnabrück, January 2023

Examiners:

Prof. Dr. Joachim Wollschläger
Dr. Karsten Küpper

Contents

1 Introduction **1**

2 Theoretical background **3**
2.1 Periodic structures - single crystals and thin films . . . 3
2.1.1 Single crystals . . . 3
2.1.2 Bravais lattices . . . 4
2.1.3 Lattice planes . . . 4
2.1.4 Reciprocal lattice . . . 4
2.1.5 Epitaxial film growth . . . 5
2.1.6 Lattice mismatch and crystallographic defects . . . 6
2.2 X-ray diffraction . . . 8
2.2.1 Bragg and Laue condition . . . 8
2.2.2 Kinematic diffraction theory . . . 9
2.3 X-ray reflectivity . . . 14
2.4 Low-energy electron diffraction . . . 16
2.5 X-ray photoelectron spectroscopy . . . 17
2.5.1 General information . . . 18
2.5.2 Spectral features . . . 20
2.5.3 Quantitative analysis and depth profiling . . . 21
2.6 X-ray absorption spectroscopy . . . 23
2.7 X-ray magnetic circular dichroism . . . 23
2.7.1 Sum rules . . . 24
2.7.2 Charge-transfer multiplet theory . . . 25
2.8 Matter in magnetic fields . . . 26
2.8.1 Basic principles . . . 26
2.8.2 Magnetism in solids . . . 27
2.8.3 Magnetization curves . . . 30
2.8.4 Domain formation . . . 30
2.8.5 Collective magnetic ordering . . . 33
2.9 Superconducting quantum interference device . . . 34
2.9.1 Superconductivity . . . 34
2.9.2 Flux quantization . . . 34
2.9.3 Josephson effect . . . 35
2.9.4 SQUID sensor . . . 36

3 Investigated materials **37**
3.1 Substrate material . . . 37
3.1.1 Magnesium oxide - MgO . . . 37
3.1.2 Strontium titanate - $SrTiO_3$ . . . 37
3.1.3 Magnesium aluminate - $MgAl_2O_4$ . . . 38
3.2 Film material . . . 39
3.2.1 Magnetite - Fe_3O_4 . . . 39
3.2.2 Cobalt ferrite - $CoFe_2O_4$ . . . 39

3.2.3 Nickel cobaltite - $NiCo_2O_4$ . . . 40
3.2.4 Antiphase boundaries in ferrites . . . 40

4 Experimental setups **43**
4.1 Sample preparation . . . 43
4.2 Surface characterization . . . 44
4.2.1 LEED - Experimental setup . . . 44
4.2.2 XPS - Experimental setup . . . 45
4.3 Experimental setups at synchrotron radiation facilities . . . 46
4.3.1 Generation of synchrotron radiation . . . 46
4.3.2 HAXPES - Experimental setup . . . 47
4.3.3 (GI)XRD and XRR - Experimental setup . . . 48
4.3.4 XAS/XMCD . . . 49
4.4 SQUID magnetometry . . . 50

5 Interface Magnetization Phenomena in Epitaxial Thin $Fe_3O_4/Co_xFe_{3-x}O_4$ Bilayers **53**
K. Ruwisch[1], J. Thien[1], T. Pohlmann[1,2], M. Hoppe[1,2], F. Bertram[2], K. Kuepper[1], and J. Wollschläger[1]
The Journal of Physical Chemistry C ***117****, 42, 23327–23337 (2021)*

6 Real-time Monitoring the Growth of Epitaxial $Co_xFe_{3-x}O_4$ Ultrathin Films on Nb-Doped $SrTiO_3$(001) via Reactive Molecular Beam Epitaxy by Means of Operando HAXPES **55**
K. Ruwisch[1], T. Pohlmann[1,2], F. Bertram[2], C. Schlüter[2], A. Gloskovskii[2], K. Kuepper[1], and J. Wollschläger[1]
Materials ***2022****, 15, 2377*

6.1 Introduction . . . 55
6.2 Materials and Methods . . . 56
6.3 Results and Discussion . . . 57
6.3.1 HAXPES . . . 57
6.3.2 XRD . . . 62
6.4 Conlusions . . . 63

7 Influence of Oxygen Plasma on the Growth and Stability of Epitaxial $NiCo_2O_4$ Ultrathin Films on Various Substrates **65**
K. Ruwisch, A. Alexander, T. Pollenske, K. Kuepper, and J. Wollschläger
Materials ***2022****, 15, 6911*

7.1 Introduction . . . 65
7.2 Materials and Methods . . . 66
7.3 Results and Discussion . . . 67
7.3.1 LEED . . . 67
7.3.2 Soft-XPS . . . 68
7.3.3 XRR . . . 69
7.3.4 XRD . . . 70
7.3.5 HAXPES . . . 72
7.4 Conclusions . . . 74

8 Summary and outlook **75**

9 List of publications **77**

Literature **79**

1 Introduction

Today's world faces several problems at once. On the one hand, steadily growing amounts of data are being produced that need to be stored securely and, on the other hand, there is a shortage of energy which is associated with immense costs for electricity, for example. The goal must therefore be to make the storage of data as energy-efficient as possible. One way to ensure this is to use so-called spintronic components [1]. Here, in contrast to conventional electronic components, the spin of electrons is used to process data [2]. Today, the application of spintronics is already established in the field of magnetoresistive read heads for hard disk drives [3] or in the field of magnetoresistive random-access memory (MRAM) [4]. The origin of spintronics can be traced back to the discovery of the giant magnetoresistance (GMR) effect by the research groups of Albert Fert [5] and Peter Grünberg [6] in the late 1980s. They observed that the electrical resistance of two ferro/ferrimagnetic materials separated by a non-magnetic conducting layer depended highly on the relative angle of the magnetizations of both layers. In fact, the two magnetization states can be used to represent the binary values 0 and 1, as used in computer science for storage media [7].

Another effect based on the spin of electrons is tunneling magnetoresistance (TMR), discovered by Michel Jullière in 1975 [8]. The TMR effect could only be produced by Jullière at very low temperatures, and later the works of Moodera *et al.* [9] and Miyazaki *et al.* [10] demonstrated that the effect could be used at room temperature. The GMR and TMR effects are very similar due to their structure (two ferro/ferrimagnetic layers separated by an insulating material). Here, the non-conducting film acts as a tunnel barrier. As a spintronic device, this is then called a magnetic tunneling junction (MTJ), based on TMR. In this context, magnetic oxides are of highest interest for spintronic applications, since they possess tunable electronic and magnetic properties. Half-metals are particularly suitable for this purpose, due to their predicted complete spin polarization at the Fermi level. As an electrode material, probably the most prominent candidate is magnetite (Fe_3O_4), since it is a transition metal oxide with ferrimagnetic order and a predicted spin polarization of 100 % [11]. The generation of highly spin-polarized currents could be very likely, however, in practice, the observed effects are lower than theoretically predicted [12–14], which could be explained by interface effects [15, 16]. Furthermore, nickel cobaltite is widely mentioned in the literature as another interesting material for spin injection layer, but its spin polarization is reported to be only −73 % [17, 18]. Therefore, it is of utmost importance to better understand e.g. interface effects of these promising materials and to adapt them to the required conditions. Another possibility is the application of so-called spin filters, in which a layer of magnetic insulators acts as a tunnel barrier. A commonly used material is $CoFe_2O_4$ [19]. In a magnetic insulator, electrons with a certain spin orientation have a higher probability to overcome the tunnel barrier because the energy levels are split in the conduction band. Nevertheless, the fabrication of cobalt ferrite ($CoFe_2O_4$) as a tunnel barrier is not so easy in practice, because during the fabrication, e.g., lattice defects are induced, which in turn affect the magnetic and structural properties and could also change the insulating characteristic of the layer.

In the context of multilayer systems, as they occur for example in the GMR effect, interface effects like exchange bias or exchange-spring exist. At the interface between a magnetically soft and magnetically hard material, it is possible that the magnetically soft phase rotates reversibly with respect to the magnetically hard phase in the presence of small magnetic fields. This is caused by the exchange-spring process. This phenomenon has been observed in $CoFe_2O_4/CoFe_2$

nanoparticles [20, 21] and ultrathin bilayers [22], among others. In particular, in the application of spin filters or spin-tunnel junctions, such combinations of magnetically soft/hard bilayers are of highest interest [23–25], also because the exchange-spring effect can be controlled by electric fields [26]. From this point of view, it is incredibly important to understand this exchange coupling in order to adapt and tailor the material system according to the respective requirements.

Based on this motivation, the crystalline, epitaxial growth of ultrathin magnetite, cobalt ferrite and nickel cobaltite layers is characterized in this thesis in connection with their structural, chemical and magnetic properties with the help of various investigation methods. In the following chapter 2 the necessary theoretical basics of the employed methods, as well as additional physical backgrounds helpful for the understanding are explained. Afterwards, in chapter 3 the presentation of the materials used in this thesis is given. In order to better understand the experimental setups, an explanation of the measurement methods used here is provided in chapter 4. In the following chapters 5 to 7 the experimental results are presented. Chapter 5 is about the preparation and characterization of $Fe_3O_4/CoFe_2O_4$ bilayers with different film thicknesses. In particular, the focus of the study here is on the magnetic properties and the cationic distribution within the layers in dependence of the stoichiometry of the cobalt ferrite layers using superconducting quantum interference sensing (SQUID) and X-ray magnetic circular dichroism (XMCD). In situ characterization of the layers is performed by low energy electron diffraction (LEED) and X-ray photoelectron spectroscopy (XPS). The X-ray reflectivity (XRR) measurement method is used to control the layer thicknesses. To obtain further depth-resolved information about the chemical composition the method angle-resolved hard X-ray photoelectron spectroscopy (AR-HAXPES) is used. The results are published in *The Journal of Physical Chemistry C* **125**(42), 23327–23337 (2021) [27].

For a better understanding of the formation of cobalt ferrite films, chapter 6 deals with the early stages of the growth of cobalt ferrite that occurs at different oxygen partial pressures. The chemical composition is investigated using HAXPES. Furthermore, XRR and X-ray diffraction (XRD) experiments provide additional information on the structure of the grown films in addition to the chemical properties. The results are published in *Materials* **15**(7), 2377 (2022) [28].

Finally, in chapter 7, the material system is changed and the fabrication of thin nickel cobaltite films using reactive and oxygen plasma assisted molecular beam epitaxy is investigated. This fabrication method is a novel approach compared to previous studies and is still quite poorly understood. Again, in situ characterization of the films is performed by LEED and XPS. Subsequent XRR and XRD experiments provide information about the structural composition of the films. Finally, AR-HAXPES experiments provide information on whether the films are homogeneous even in deeper layers and about the chemical composition. The results are published in *Materials* **15**(19), 6911 (2022) [29]. In the last chapter 8, a summary of all results of this work is given and an outlook provides possibilities for further research on this topic.

2 Theoretical background

In this chapter, the necessary theoretical background required for this thesis is presented. If necessary, further literature is referred to at the particular points. First, periodic structures are explained for a basic understanding of crystals and the growth of thin films is discussed. This is followed by a description of X-ray diffraction, and then the closely related method of X-ray reflectivity is explained. This is followed by the method of low energy electron diffraction, before the spectroscopic measurement methods X-ray photoelectron spectroscopy, X-ray absorption spectroscopy and the associated X-ray circular dichroism are explained. Finally, magnetism is treated, first describing the magnetic fundamentals and then the associated method of the superconducting quantum interference device.

2.1 Periodic structures - single crystals and thin films

The following chapter deals with the theoretical basics of periodic structures. For this purpose, single crystals and Bravais lattices are discussed first, followed by lattice planes. Then the reciprocal lattice is introduced and the different growth modes are explained. Finally, lattice mismatches and crystallographic defects are discussed.

2.1.1 Single crystals

The ideal crystal is an infinite periodical arrangement of identical structural elements. The whole symmetry of the crystal can be described by the so-called unit cell. It is based on the periodicity of the structural elements. By three linearly independent vectors $\vec{a}$, $\vec{b}$ and $\vec{c}$ the translation can be determined by

$$\vec{R}_n = n_a\vec{a} + n_b\vec{b} + n_c\vec{c} \quad \text{with} \quad n_a, n_b \text{ and } n_c \in \mathbb{Z}. \tag{2.1}$$

As only the translational symmetry must be accomplished there are various ways to choose a unit cell describing the same crystal lattice. A primitive unit cell is the unit cell with the smallest possible volume. In order to describe the crystal structure correctly, in addition to the information about the lattice, information about the position of the individual atoms within the unit cell must also be given, especially if there is more than one atom in the unit cell. For j atoms the vector

$$\vec{r}_j = u_j\vec{a} + v_j\vec{b} + w_j\vec{c} \quad \text{with} \quad 0 \leq u_j, v_j, w_j \leq 1, \tag{2.2}$$

with u_j, v_j and w_j as the respective coordinates of the j-th atom can be defined. After linear combination

$$\vec{r}_{\text{atom}} = \vec{R}_n + \vec{r}_j \tag{2.3}$$

defines a vector from which any atom in the unit cell can be reached. Fig. 2.1 shows an exemplary two-dimensional crystal lattice to visualize the equations introduced before.

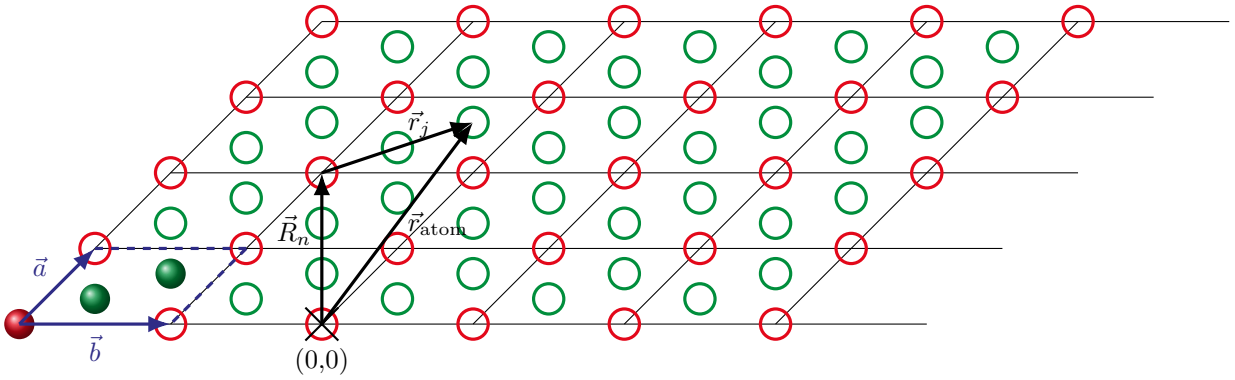

Fig. 2.1: Sketch of a two dimensional crystal with primitive lattice vectors $\vec{a}$ and $\vec{b}$ spanning a primitive unit cell (blue) with three base atoms (red and green). Using vectorial superposition of the vectors $\vec{R}_n$ and $\vec{r}_j$, any atomic position $\vec{r}_{\mathrm{atom}}$ within the unit cell can be reached. Adapted from [30].

2.1.2 Bravais lattices

Crystal structures can be classified into seven different crystal systems cubic, tetragonal, orthorhombic, hexagonal, trigonal, monoclinic and triclinic, if different symmetry properties are used on the basis of the crystal lattice and only the symmetry of the point group is considered. These are translation, rotation and inversion. With additional translation operations, seven more centered unit cells are added to the previous primitive types. These are face-centered, body-centered and base-centered. All in all, this results in a total of 14 possible so-called Bravais lattices. For an illustrative presentation, please refer to the literature [31].

2.1.3 Lattice planes

In order to describe the directions and planes in a crystal it is necessary to introduce a uniform notation. Considering the crystal axes a, b and c, a lattice plane (cf. Fig. 2.2) can be spanned from three lattice points which do not lie on a straight line. The orientation of the plane in relation to the crystal axes is determined by the intersection points with them. From the intersection points m_i their reciprocals are formed and multiplied by the smallest possible factor p, so that the fraction becomes an integer. Each triplet of numbers (hkl) uniquely describes a set of parallel mesh planes and is called called Miller indices. Equivalent crystal planes are designated with curly brackets, e.g. $\{hkl\}$, whereas the specification of a crystal direction is written in the notation $[hkl]$. Again, an equivalent crystal direction can be specified, in which case angle brackets $\langle hkl \rangle$ are used. Negative Miller indices are indicated by a dash above the numbers, e.g. $(\bar{h}kl)$.

2.1.4 Reciprocal lattice

For investigation of crystal structure it is helpful to define the so-called reciprocal lattice. By definition,

$$\vec{a}^* = \frac{2\pi}{V_\mathrm{u}} \cdot \left(\vec{b} \times \vec{c}\right), \quad \vec{b}^* = \frac{2\pi}{V_\mathrm{u}} \cdot (\vec{c} \times \vec{a}) \quad \text{and} \quad \vec{c}^* = \frac{2\pi}{V_\mathrm{u}} \cdot \left(\vec{a} \times \vec{b}\right) \tag{2.4}$$

are the reciprocal basis vectors, where V_u describes the volume of a unit cell. In terms of illustration, this means that the reciprocal basis vector $\vec{a}^*$ is orthogonal on the spanned plane of the vectors

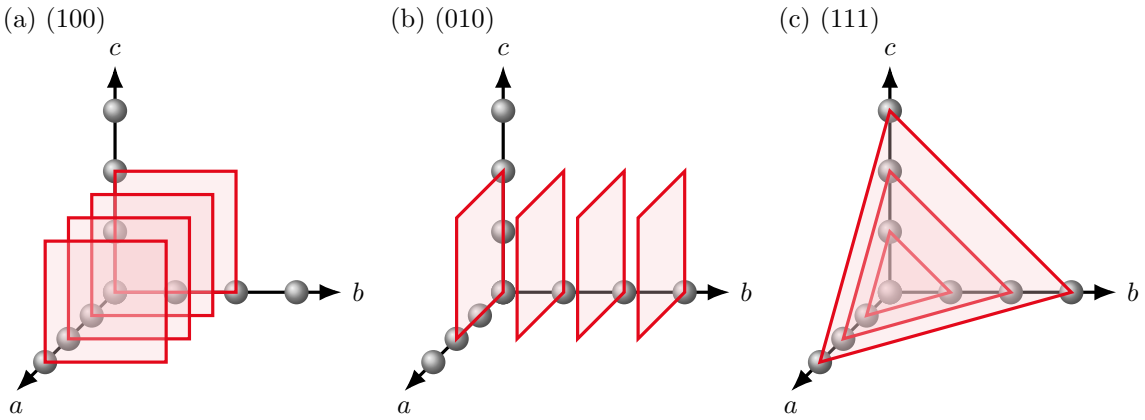

Fig. 2.2: Examples of three different lattice planes in a cubic lattice. Shown are in (a) the (100)-, in (b) the (010)- and in (c) the (111)-crystal plane. Adapted according to [32].

$\vec{b}$ and $\vec{c}$ of the crystal lattice. It follows that the reciprocal lattice vector

$$\vec{G}_{hkl} = h\vec{a}^* + k\vec{b}^* + l\vec{c}^* \quad \text{with} \quad h,k,l \in \mathbb{Z} \tag{2.5}$$

is perpendicular to the lattice planes (hkl). The magnitude of the reciprocal lattice vector can also be expressed by

$$\left|\vec{G}\right| = \frac{2\pi}{d_{hkl}}, \tag{2.6}$$

where d_{hkl} is the distance between two net planes.

To describe a periodic surface structure, one can conceive of it as a two-dimensional lattice, to which in turn a reciprocal lattice is defined. In this case, there is no periodicity perpendicular to the sample surface, so the reciprocal lattice vector can be taken to be infinitely small. This results in diffraction rods perpendicular to the surface.

The reciprocal lattice vector simplifies accordingly to

$$\vec{G}_{hk} = h\vec{a}^* + k\vec{b}^* \quad \text{with} \quad h,k \in \mathbb{Z}. \tag{2.7}$$

For the reciprocal basis vectors therefore applies

$$\vec{a}^* = 2\pi \cdot \frac{\vec{b} \times \vec{n}}{A_\mathrm{u}} \qquad \vec{b}^* = 2\pi \cdot \frac{\vec{a} \times \vec{n}}{A_\mathrm{u}}, \tag{2.8}$$

with $\vec{n}$ as normal vector and A_u the area of the unit cell.

2.1.5 Epitaxial film growth

Epitaxy is the oriented growth of crystalline layers on single crystalline substrates. If the materials of the layer and substrate are identical, it is called homoepitaxy. If the materials are different, it is called heteroepitaxy. In general, the growth behavior depends on kinetic and thermodynamic processes. A distinction is made between three different growth modes, which will be discussed in more detail below.

Frank-van-der-Merwe (layer-by-layer) growth

The film and substrate atoms are more strongly bonded to each other than the atoms of the film are to each other. Only after a closed monolayer has formed, the film atoms grow on top of each other and then form another layer.

Volmer-Weber (island) growth

The opposite case occurs when the bond between the atoms of the film is stronger than the bond between substrate and film atoms. This is referred to as island growth, in which high islands first form before the film closes.

Stranski-Krastanov (layer-plus-island) growth

If a combination of the two growth modes mentioned above occurs, this is referred to as is the layer-plus-island growth. Here, closed layers are initially formed up to a certain film thickness, followed by the growth of islands.

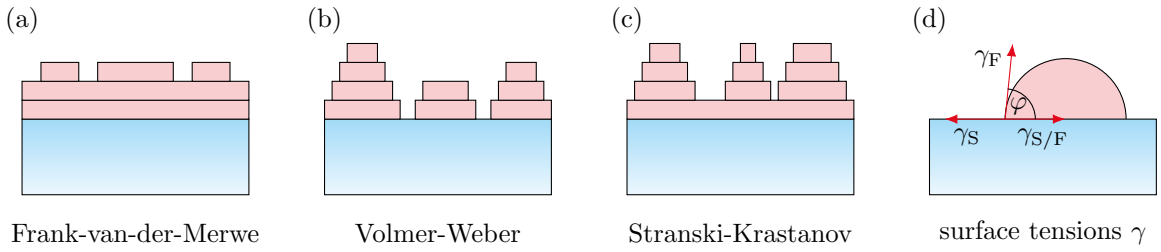

Fig. 2.3: Schematic representation of the three growth modes of a thin film (red) on a substrate (blue). (a) Franck-van-der-Merwe (layer-by-layer), (b) Volmer-Weber (island), and (c) Stranski-Krastanov (layer-plus-island) growth. (d) shows the correlation between surface and interface tensions associated with the wetting angle φ. Inspired by [33].

The different growth modes can be explained in terms of the surface or interface tension γ. Here, γ represents the work that must be applied to form a surface. With the so-called island wetting angle φ, the following equilibrium of forces can be established.

$$\gamma_S = \gamma_{S/F} + \gamma_F \cos(\varphi), \tag{2.9}$$

with γ_S as the surface tension of the substrate, $\gamma_{S/F}$ the interface tension of the substrate and film interface and γ_F as the tension of the film. For a wetting-angle of 0°, Eq. (2.9) becomes $\gamma_S \geq \gamma_{S/F} + \gamma_F$, which corresponds to layer-by-layer growth. In contrast to that, island growth forms for $\varphi > 0$ and $\gamma_S < \gamma_{S/F} + \gamma_F$ holds. For the layer-plus-island growth a mixture of the two conditions mentioned before, is obtained. First, it grows like layer-by-layer growth and after that, both the values of γ_S and $\gamma_{S/F}$ change during the process which makes this disadvantageous and island growth is obtained.

2.1.6 Lattice mismatch and crystallographic defects

When a crystalline film of a particular material is deposited on a crystalline substrate of another material, it is known as heteroepitaxy. Since substrate and film are made of different materials and therefore have different lattice constants, it is very rare that the growth is lattice-matched. The lattice mismatch f can be described by the equation

$$f = \frac{a_f - a_s}{a_s}. \tag{2.10}$$

Here a_f and a_s are the lattice constants of the film and substrate, respectively. Based on the lattice mismatch, a lateral and vertical strain can be specified, respectively. The lateral strain is defined as

$$\varepsilon_{\parallel} = \frac{a_{f,str} - a_f}{a_f} = \frac{\Delta a_f}{a_f}, \tag{2.11}$$

where $a_{f,str}$ and a_f describe strained and original film in-plane lattice constants, respectively. Analogous to the lateral strain, the vertical strain can also be specified via

$$\varepsilon_{\perp} = \frac{c_{f,str} - c_f}{c_f} = \frac{\Delta c_f}{c_f}, \tag{2.12}$$

where $c_{f,str}$ and c_f describe strained and original out-of-plane film lattice constants, respectively. The relationship between lateral and vertical strain can be described by the equation

$$\frac{\Delta c_f}{c_f} = \frac{2\nu}{\nu - 1}\frac{\Delta a_f}{a_f} \tag{2.13}$$

where ν indicates the Poisson ratio of the film material [34]. In addition to lateral lattice-matched growth, there is also so-called pseudomorphic growth and dislocated growth. The growth depends on the free energy density of the respective process. In the case of small mismatches, the strained film can adopt the in plane periodicity of the substrate and form the strain perpendicular to the substrate. For larger mismatches, so-called dislocations are induced in the film. Fig. 2.4 shows lattice-matched, pseudomorphic growth and growth with dislocations. With the equation

$$d_{dis} = \frac{a_f a_s}{|a_s - a_f|}, \tag{2.14}$$

the distance between dislocations can be calculated assuming complete relaxation.

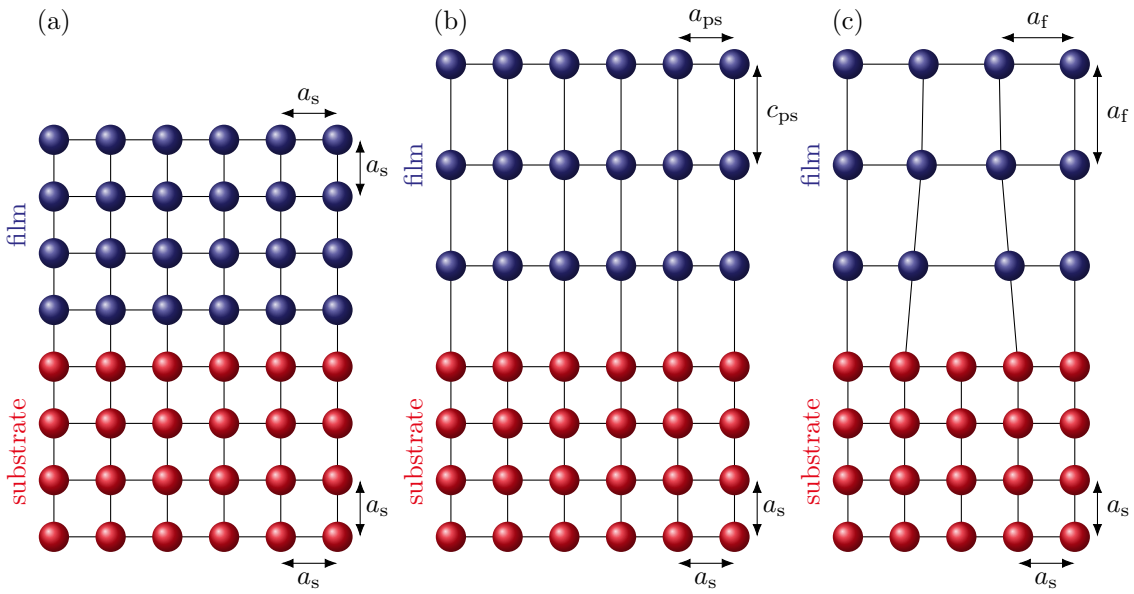

Fig. 2.4: Illustration of the different types of epitaxy. (a) Lattice-matched growth. Lattice constants of film a_f (blue) and substrate a_s (red) match. (b) pseudomorphic growth. Lattice constant in lateral direction matches and is stretched ($c_{ps} > a_f$), in vertical direction lattice constants of substrate and film match. (c) Dislocations occur in lower layers, leading to relaxed growth of the film. Adapted from [33].

As the layer thickness increases, the strain energy in the pseudomorphic layer increases as well. At a certain critical layer thickness, it is energetically more favorable to reduce the strain by dislocations. To calculate the critical layer thickness d_c, the model of Matthews and Blakeslee is applicable [35]. This is given by the formula

$$\frac{d_c}{b} = \frac{\left(1 - \nu\cos^2(\alpha)\right)\left(\ln\left(\frac{d_c}{b}\right) + 1\right)}{2\pi f(1+\nu)\cos(\lambda)}. \tag{2.15}$$

Wherein b describes the magnitude of the so-called Burgers vector, f is the lattice mismatch and ν is the Poisson ratio. α describes the angle between Burgers vector and the dislocation line, which is 90° if edge dislocations are under consideration. λ, on the other hand, describes the angle between the slip direction and the direction in the film plane perpendicular to the line of intersection of the slip plane with the interface.

The information for this chapter stems from [33, 36–38].

2.2 X-ray diffraction

For the investigation of crystalline materials, X-ray diffraction (XRD) is one of the most widely used methods. For this purpose, X-rays are scattered at the electrons bound to the atoms and their diffracted intensity is evaluated in the end. In the following chapter first the Bragg and Laue condition is discussed and then the kinematic diffraction theory will be explained, where first the scattering at a single electron is discussed and then the observation level is successively increased, until finally the diffraction at a thin film system is addressed.

2.2.1 Bragg and Laue condition

Fig. 2.5 illustrates the principle: At an angle ϑ the incident X-ray beam hits the periodic arrangement of atoms in a solid. The incident beam is reflected at the lattice planes, with distance d_{hkl}. This results in a path difference of $d\sin(\vartheta)$. For long-range, periodically arranged atoms, either constructive or destructive interference can occur due to scattering at different atomic positions. From the diffraction reflections that arise from constructive interference, a prediction can finally be made about the structure of the material. For reflections to arise, the Bragg equation

$$n\lambda = 2d_{hkl}\sin(\vartheta), \text{ with } n \in \mathbb{N} \tag{2.16}$$

must be satisfied. λ denotes the wavelength of the incoming X-ray beam. For the Bragg condition to be satisfied, this must be approximately in the range of atomic distances, i.e., in the range of a few angstroms. A generally useful description is also the so-called Laue condition [39], which is as follows:

$$\vec{q}\cdot\vec{a} = 2\pi h, \tag{2.17}$$
$$\vec{q}\cdot\vec{b} = 2\pi k, \tag{2.18}$$
$$\vec{q}\cdot\vec{c} = 2\pi l. \tag{2.19}$$

Here $h, k, l \in \mathbb{Z}$ are the so-called Miller indices as introduced in chapter 2.1.3. $\vec{q}$ describes the scattering vector and $\vec{a}, \vec{b}$ and $\vec{c}$ the three basis vectors of the crystal lattice. The scattering vector can be described by $\vec{q} = \vec{k}_\mathrm{f} - \vec{k}_\mathrm{i}$, i.e. the difference between incident ($\vec{k}_\mathrm{i}$) and outgoing ($\vec{k}_\mathrm{f}$) vector and constructive interference occurs when this scattering vector satisfies the Laue condition. For the consideration of diffraction phenomena the introduction of the reciprocal lattice has made itself

useful (cf. Chap. 2.1.4). Constructive interference always occurs if the scattering vector $\vec{q}$ coincides with a point in the reciprocal lattice, considering no absorption and an infinitely expanded crystal. This is illustrated by the Laue condition with reciprocal lattice vectors. It is

$$\vec{q} = h\vec{a}^* + k\vec{b}^* + l\vec{c}^* = \vec{G}_{hkl}. \tag{2.20}$$

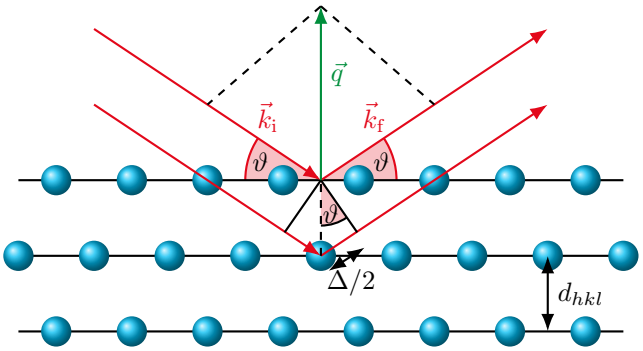

Fig. 2.5: Schematic representation of the Bragg condition for constructive interference. The scattering of an X-ray beam incident at an angle ϑ is observed. The incident beam ($\vec{k}_\mathrm{i}$) is reflected at the lattice planes, with distance d_{hkl}. The path difference $\Delta/2$ between the reflected beams ($\vec{k}_\mathrm{f}$) is here $d_{hkl}\sin(\vartheta)$. For an integer multiple of 2, the phase shift is zero and the reflected beams overlap. In this case, constructive interference occurs. Adapted from [40].

2.2.2 Kinematic diffraction theory

Using the Bragg and Laue conditions, only information about the periodicities in the crystal lattice can be obtained, since only the position of the constructive interference is described. For further investigations, the intensities of the diffracted X-rays must be considered in more detail. This will then also provide information about the arrangement of the atoms within the crystal lattice. The structure of the chapter is as follows: the observation level becomes progressively larger, from scattering of a single electron, to the scattering of an entire crystal.

Scattering at a single electron

Since the scattering cross section of electrons is much larger compared to the atomic nucleus, the X-rays are mainly scattered by the electrons. According to Thomson formula and considering dipole approximation [41–43], the amplitude of a wave can be described by

$$A(\vec{q}) = A_0 \frac{e^2\sqrt{P}}{m_\mathrm{e}c^2 R} e^{i\vec{q}\cdot\vec{r}_\mathrm{e}}. \tag{2.21}$$

In it A_0 is the amplitude of the incoming wave, e the elementary charge with the electron mass m_e, c the speed of light, as well as R the distance to the detector and P the polarization factor of the incoming wave.

Scattering at a single atom

An atom is generally surrounded by electrons. To obtain the scattering amplitude of this atom, the scattering contributions of the individual electrons must simply be summed up. Considering electrons in general as an electron density distribution with a distance between nucleus and electrons

$|\vec{r}|$, the amplitude of a wave scattered from the single atom is given by

$$A(\vec{q}) = A_0 C \int d^3 r \rho(\vec{r}) e^{i\vec{q}\cdot(\vec{r}+\vec{r}_{\text{atom}})} \tag{2.22}$$

$$= A_0 C f(\vec{q}) e^{i\vec{q}\cdot\vec{r}_{\text{atom}}}. \tag{2.23}$$

Therein $f(\vec{q})$ is defined as an atomic form factor giving the Fourier transform of the electron density of the atom. It is

$$f(\vec{q}) = \int d^3 r \rho(\vec{r}) e^{i\vec{q}\cdot\vec{r}}. \tag{2.24}$$

Assuming, which is quite valid here, that the electron distribution is spherical, the atomic form factor depends only on the absolute value of the scattering vector [44]. Reference [45] provides tabulated values for this.

Scattering at a single unit cell

A unit cell consists of several atoms. Applying this, analogous to the previous consideration, the scattering amplitude of the unit cell is obtained by summing up the contributions of all j atoms. It follows that

$$A(\vec{q}) = A_0 C \sum_j f_j(q) e^{i\vec{q}\cdot(\vec{R}_n+\vec{r}_j)} \tag{2.25}$$

$$= A_0 C F(\vec{q}) e^{i\vec{q}\cdot\vec{R}_n}. \tag{2.26}$$

Where $\vec{R}_n$ is the position of the unit cell and $\vec{r}_j$ is the position of the j-th atom within that unit cell. Like the atomic form factor, the so-called structure factor can be calculated via the relation

$$F(\vec{q}) = \sum_j f_j(q) e^{i\vec{q}\cdot\vec{r}_j}. \tag{2.27}$$

So here, similar to the previous section, all atomic form factors are summed and give the Fourier transform of the electron distribution in the unit cell. A closer look at the equation reveals that the structure factor depends, in particular, on the direction of the scattering vector $\vec{q}$.

Diffraction at a single crystal

A single crystal can be considered as a periodic arrangement of many unit cells in all three spatial directions ($\vec{a}, \vec{b}$ and $\vec{c}$). Thus, analogous to the previous sections, the scattering amplitude of the single crystal can be calculated by accumulating the intensities scattered at all unit cells. However, a phase shift between the scattered waves must be taken into account. This leads to the equation

$$A(\vec{q}) = A_0 C \sum_n F_n(\vec{q}) e^{i\vec{q}\cdot\vec{R}_n}. \tag{2.28}$$

The structure factors $F_n(\vec{q})$ defined earlier can be considered the same, assuming that the crystal is composed of identical unit cells. As described above, the unit cells are arranged periodically in the different spatial directions. If the number of unit cells is the same along each crystallographic

direction,

$$A(\vec{q}) = A_0\, C\, F(\vec{q}) \sum_{n_a=0}^{N_a-1} \sum_{n_b=0}^{N_b-1} \sum_{n_c=0}^{N_c-1} e^{i\vec{q}\cdot\left(n_a\vec{a}+n_b\vec{b}+n_c\vec{c}\right)} \tag{2.29}$$

$$= A_0\, C\, F(\vec{q}) \sum_{n_a=0}^{N_a-1} e^{in_a\,\vec{q}\cdot\vec{a}} \sum_{n_b=0}^{N_b-1} e^{in_b\,\vec{q}\cdot\vec{b}} \sum_{n_c=0}^{N_c-1} e^{in_c\,\vec{q}\cdot\vec{c}} \tag{2.30}$$

is obtained. If the sums are interpreted as a geometric series, the following rearrangement results for N_c, for example.

$$B_{N_c}(\vec{q}) = \sum_{n_c=0}^{N_c-1} e^{in_c\,\vec{q}\cdot\vec{c}} = \frac{1-e^{iN_c\,\vec{q}\cdot\vec{c}}}{1-e^{i\,\vec{q}\cdot\vec{c}}}. \tag{2.31}$$

The reordering for the special case along the direction N_c can be adapted to all directions. The diffraction intensity is obtained by squaring Eq. (2.31). It follows

$$S_{N_c}(x) = |B_{N_c}|^2(x) = \frac{\sin^2(N_c\,x/2)}{\sin^2(x/2)}, \tag{2.32}$$

wherein $\vec{q}\cdot\vec{c}$ has been replaced by x. Eq. (2.32) is also called the N-slit function. For the case $N = 6$ the function is shown in Fig. 2.6. The maximum intensity is N^2 with a periodicity of 2π. Between the main maxima, secondary maxima are formed, which are called fringes. The spacing of the minor maxima also has a 2π periodicity evenly divided among the number of unit cells. Scherrer's formula can be used to establish a relationship between full width at half maximum (FWHM) of main maxima and number of unit cells. It follows that

$$\mathrm{FWHM} = K_\mathrm{S}\frac{2\pi}{N}, \tag{2.33}$$

with the Scherrer factor $K_\mathrm{S} = 0.89$ assuming an ideally shaped crystal (cf. Chap. 2.1.1) [46].

For an ideal single crystal, there are infinitely many unit cells in each crystallographic direction. This distributes the total intensity to the main maxima. Using δ distributions consistent with Laue conditions, the amplitude can then be given as

$$A(\vec{q}) \sim A_0 C F(\vec{q}) \sum_h \sum_k \sum_l \delta(\vec{q}\cdot\vec{a}-2\pi h)\delta(\vec{q}\cdot\vec{b}-2\pi k)\delta(\vec{q}\cdot\vec{c}-2\pi l). \tag{2.34}$$

These discrete points are the so-called Bragg peaks.

Diffraction at a semi-infinite crystal

In reality, the theoretical considerations mentioned above do not occur. A real crystal is not infinitely spanned in all spatial directions, but has finite dimensions, especially due to its surface. If an X-ray beam hits a crystal surface, the beam penetrates into deeper crystal layers (in the µm range) due to weak interaction between matter and X-rays. The intensity of deeper layers also contributes to the total diffraction intensity, and here absorption processes are the reason for attenuation of intensity from deeper layers. The previous models of classical kinematic diffraction theory must therefore be reconciled and adjusted with the decreasing intensity of the X-rays, as they penetrate the crystal. If the penetration depth of the X-ray beam is much smaller than the thickness of the crystal, it is assumed to be semi-infinite along the crystal surface. For the substrates

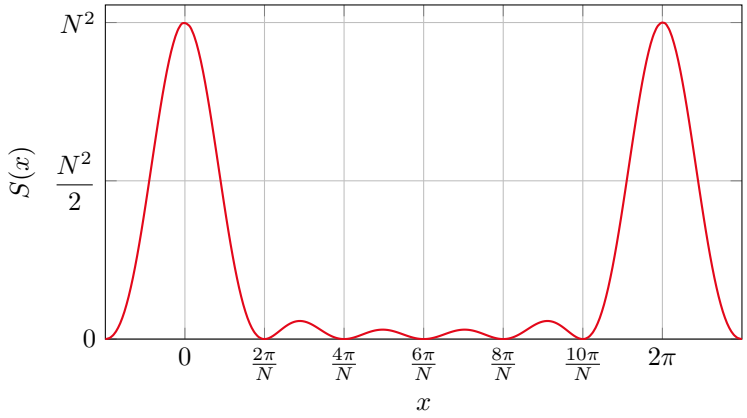

Fig. 2.6: The figure shows an example N-slit function for $N = 6$. The positions of the main maxima are at multiples of 2π and have a height of N^2. Between the main maxima, so-called fringes can be seen, which in turn form maxima and minima. The distance between the minima may be expressed as $2\pi/N$.

used in this work, this agrees. Assuming that absorption (ε) occurs in each of the layers, it follows that the amplitude is limited in the vertical direction. It is defined by

$$A_{\text{sub}}(\vec{q}) = A_0\, C\, F(\vec{q}) \sum_{n_a=0}^{N_a-1} e^{i n_a \vec{q}\cdot\vec{a}} \sum_{n_b=0}^{N_b-1} e^{i n_b \vec{q}\cdot\vec{b}} \sum_{n_c=-\infty}^{N_c(n_a,n_b)} e^{i\, n_c\, \vec{q}\cdot\vec{c}}\, e^{n_c \varepsilon}. \tag{2.35}$$

An exponential dependence is assumed therein for the absorption. By $N_c(n_a, n_b)$ the height of the layer, respectively in the direction of n_a and n_b can be modeled. This corresponds to the surface roughness. If the Laue conditions are satisfied (only Eq. (2.17) and (2.18) due to lateral consideration), it can be further written

$$A_{\text{sub}}(\vec{q}) = A_0\, C\, F(\vec{q}) \sum_{n_a=0}^{N_a-1} 1 \sum_{n_b=0}^{N_b-1} 1 \sum_{n_c=-\infty}^{N_c(n_a,n_b)} e^{i\, n_c\, \vec{q}\cdot\vec{c} + n_c \varepsilon} \tag{2.36}$$

$$= A_0\, C\, F(\vec{q}) \sum_{n_a=0}^{N_a-1} \sum_{n_b=0}^{N_b-1} \frac{e^{(i\,\vec{q}\cdot\vec{c}+\varepsilon) N_c(n_a,n_b)}}{1 - e^{-(i\,\vec{q}\cdot\vec{c}+\varepsilon)}} \tag{2.37}$$

$$= A_0\, C\, F(\vec{q})\, N_a N_b \frac{\left\langle e^{(i\,\vec{q}\cdot\vec{c}+\varepsilon) N_c(n_a,n_b)} \right\rangle}{1 - e^{-(i\,\vec{q}\cdot\vec{c}+\varepsilon)}}. \tag{2.38}$$

In the last step, the sums over n_a and n_b were replaced by an averaging over $N_c(n_a, n_b)$. If, in addition, the height distribution is approximated by a Gaussian function,

$$A_{\text{sub}}(\vec{q}) = A_0\, C\, F(\vec{q})\, N_a N_b \frac{e^{-\sigma^2(1-\cos \vec{q}\cdot\vec{c})}}{1 - e^{-(i\,\vec{q}\cdot\vec{c}+\varepsilon)}} \tag{2.39}$$

can be written in simplified form. Therein σ gives the root mean square (RMS) roughness of the surface [47, 48].

The intensities perpendicular to the surface are preserved if the Laue conditions are fulfilled in lateral directions. In the ideal case (no absorption, ideal infinite crystal) Bragg peaks are formed (see Fig. 2.7(a)). If the concept of a semi-infinite crystal is used, blurred reflections in orthogonal direction to the surface are formed, which form so-called crystal truncation rods (CTRs). Along a CTR, maximum intensities are found at the nominal Bragg peak positions. In the middle between

these are so-called anti-Bragg positions, which have minimum intensities.

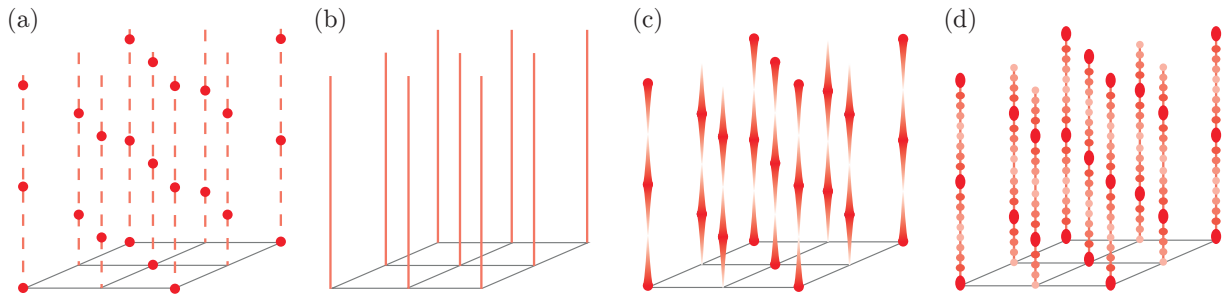

Fig. 2.7: Intensity distribution plot for selected crystalline structures in reciprocal space. (a) A 3D solid crystal with an infinite number of unit cells in the three spatial directions. Exact point-like diffraction spots at specific positions (Bragg peaks) are obtained. In order to compare the positions, the dashed lines serve as a guide for the eye. (b) A 2D crystal in 3D space forms diffraction rods. (c) In a semi-infinite (real) 3D crystal, the Bragg peaks are blurred in the direction vertical to surface and intensity minima are formed between the main maxima. (d) A thin crystalline film produces diffraction spots with intensity variations (fringes) in vertical direction. Adapted from [44, 47].

Diffraction at a crystalline thin film

Assuming that a thin film consists of only a few crystalline layers, absorption processes can again be neglected. Hence, a similar description to the previous section follows. The roughness of the layers results in different height distributions above (N_c^+) and below (N_c^-) the film. Exactly as in the previous section, these again depend on the lateral directions. For the amplitude of the diffracted wave,

$$A_{\text{film}}(\vec{q}) = A_0\, C\, F(\vec{q}) \sum_{n_a=0}^{N_a-1} 1 \sum_{n_b=0}^{N_b-1} 1 \sum_{n_c=N_c^-(n_a,n_b)}^{N_c^+(n_a,n_b)} e^{i\, n_c\, \vec{q}\cdot\vec{c}} \tag{2.40}$$

$$= A_0\, C\, F(\vec{q}) \sum_{n_a=0}^{N_a-1} \sum_{n_b=0}^{N_b-1} \frac{e^{i\,\vec{q}\cdot\vec{c}\,N_c^-(n_a,n_b)} - e^{i\,\vec{q}\cdot\vec{c}\,N_c^+(n_a,n_b)+1}}{1-e^{i\,\vec{q}\cdot\vec{c}}} \tag{2.41}$$

$$= A_0\, C\, F(\vec{q})\, N_a N_b \frac{\left\langle e^{i\vec{q}\cdot\vec{c}\,u_c^-}\right\rangle - e^{i\,\vec{q}\cdot\vec{c}\,\overline{N}_c}\left\langle e^{i\vec{q}\cdot\vec{c}\,u_c^+}\right\rangle}{1-e^{i\,\vec{q}\cdot\vec{c}}}, \tag{2.42}$$

is obtained. Furthermore, the mean value below the film is arbitrarily set to 0 and the mean value above the film is generally denoted by $\overline{N}_c$. From this follows for the amplitude (2.42), with u_c^+ and u_c^- as inaccuracies above, respectively below the film. An alternative notation is

$$A_{\text{film}}(\vec{q}) = A_0\, C\, F(\vec{q})\, N_a N_b \frac{e^{-\sigma_-^2(1-\cos(\vec{q}\cdot\vec{c}))} - e^{i\,\vec{q}\cdot\vec{c}\overline{N}_c} e^{-\sigma_+^2(1-\cos(\vec{q}\cdot\vec{c}))}}{1-e^{i\,\vec{q}\cdot\vec{c}}}, \tag{2.43}$$

assuming that the respective deviations have the form of a Gaussian function. σ_+ and σ_- are the upper and lower RMS roughnesses, respectively. All in all, the diffraction intensity of thin films can be described with diffraction peaks and intervening oscillations, as shown in Fig. 2.7(d).

Diffraction at a thin film system

In the previous considerations only single crystalline layers were considered. If the system to be examined is composed of several thin layers, the total diffraction signal is also composed by the

signal of the respective individual layers. For a thin film system consisting of substrate and i films the total amplitude is constituted from

$$A_{\text{system}}(\vec{q}) = A_{\text{sub}}(\vec{q}) + \sum_i \Theta_i e^{i\vec{q}\cdot\vec{p}_i} A_{\text{film},i}(\vec{q}) \,. \tag{2.44}$$

In this Θ_i is the so-called occupation factor, in which dislocations and impurities are considered. Furthermore, $\vec{p}_i$ gives the phase vector resulting from the interfacial vector $\vec{g}_j$ between the j-th and $(j+1)$-th layers and the phase shift $\overline{N}_{cj}\vec{c}_j$ caused by lower layers.

$$\vec{p}_i = \sum_{j=0}^{i-1} \vec{g}_j + \overline{N}_{cj}\vec{c}_j \tag{2.45}$$

will apply.

The information for this chapter stems from [44, 49, 50].

2.3 X-ray reflectivity

The measurement method of X-ray reflection (XRR) has become established for the determination of layer thicknesses of single and multilayer systems, as well as for the determination of roughnesses [51]. Similar to XRD (see Chap. 2.2), the intensity of X-rays reflected at surfaces or interfaces is measured. The angle of incidence is particularly small, it is usually $\alpha_\text{i} < 5°$. The principle of XRR is depicted in Fig. 2.8. If X-rays $\left(\vec{k}_\text{i}\right)$ hit the interface between two optical materials with

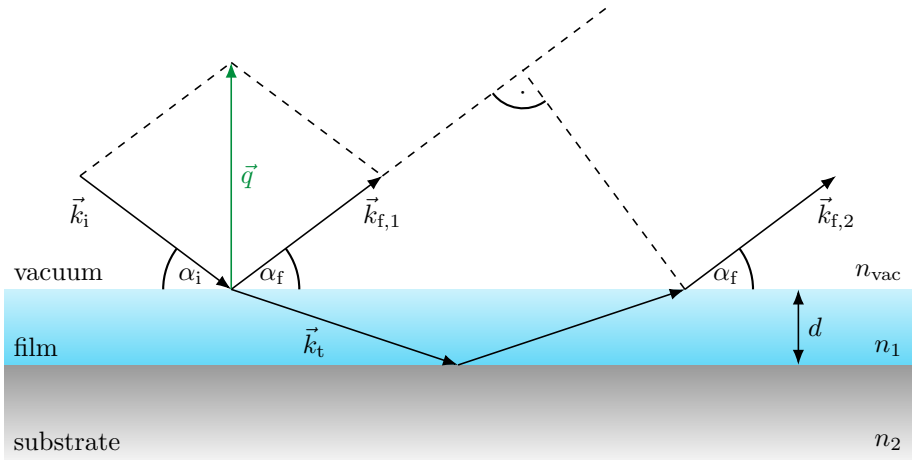

Fig. 2.8: Schematic sketch of the XRR principle. The incident wave $\vec{k}_\text{i}$ arrives at the film at an angle α_i. There, part of the wave $\left(\vec{k}_\text{f}\right)$ is reflected at an angle (α_f). Another part is transmitted $\left(\vec{k}_\text{t}\right)$, thus penetrating the film and hitting the substrate at an angle α_t. Due to the multiple scattering that occurs, the waves $\vec{k}_{\text{f},1}$ and $\vec{k}_{\text{f},2}$ can constructively or destructively interfere with each other. The scattering vector $\vec{q}$ is in any case perpendicular to the surface. Adapted from [52, 53].

refractive indices n_vac and n_1 at an angle of incidence α_i, a part of the X-rays is transmitted $\left(\vec{k}_\text{t}\right)$, the other part is reflected again at the angle of incidence $\left(\vec{k}_\text{f}\right)$. Thus $\alpha_\text{i} = \alpha_\text{f}$ is valid, therefore the scattering vector $\vec{q} = \vec{k}_\text{f} - \vec{k}_\text{i}$ is always perpendicular to the surface, so it has only a component in

z direction. This implies

$$q = q_z = 2k \sin(\alpha_\mathrm{i}) = \frac{4\pi}{\lambda} \sin(\alpha_\mathrm{i}) \,. \tag{2.46}$$

Depending on which kind of materials are irradiated, the complex refractive index

$$n = 1 - \delta + i\beta \tag{2.47}$$

changes. Therein $\delta = \lambda^2 r_\mathrm{e} \rho / 2\pi$ is the dispersion and $\beta = \lambda\mu/4\pi$ is the absorption of the respective material. In this, λ denotes the wavelength, r_e the electron radius, ρ the electron density, and μ the absorption coefficient. For flat angles of incidence smaller than the so-called critical angle α_c, total reflection occurs, thus no X-rays can penetrate the medium. The critical angle can be approximated by $\alpha_\mathrm{c} \approx \sqrt{2\delta}$, since $n < 1 = n_\mathrm{vac}$. By increasing the angle of incidence, the X-rays penetrate deeper and deeper into the layer and the reflected signal thus becomes smaller and smaller.

To normalize the reflected intensity (I_r) to the intensity of the incoming X-ray beam (I_i) one defines the so-called reflectivity $R = I_\mathrm{r}/I_\mathrm{i}$. This also corresponds to the absolute square of the complex reflection coefficient r. Analogously, the transmission $T = I_\mathrm{t}/I_\mathrm{i}$ is defined. Again, $T = |t|^2$ will be applicable. Using the Fresnel formulas

$$r = \frac{k_{\mathrm{i},z} - k_{\mathrm{t},z}}{k_{\mathrm{i},z} + k_{\mathrm{t},z}} \text{ and } t = \frac{2k_{\mathrm{i},z}}{k_{\mathrm{i},z} + k_{\mathrm{t},z}}, \tag{2.48}$$

r and t can be calculated without taking polarization into account [52], since for X-rays $n \approx 1$. In the Fresnel formulas, the vertical components, i.e. in z-direction, of $\vec{k}_\mathrm{t}$ and $\vec{k}_\mathrm{i}$ are given, respectively. It is

$$k_{\mathrm{i},z} = k \sin(\alpha_i) \quad \text{and} \quad k_{\mathrm{t},z} = k \sin(\alpha_\mathrm{t}) = k\sqrt{n^2 - \cos^2(\alpha_i)}. \tag{2.49}$$

In practice, layered systems often occur which consist of one or even several layers on the underlying substrate. In the following, the substrate is assumed to be infinitely thick. Scattering then occurs only at all interfaces and not at the backside of the substrate, due to the simplification made earlier. Lyman G. Parratt developed a recursive method in 1954 [54], which makes it possible to calculate the reflectivity of a multilayer system, taking into account the reflectivities of the respective individual layers. It is

$$R_{j-1,j} = \frac{r_{j-1,j} + R_{j,j+1} \exp(id_j q_\mathrm{j})}{1 + r_{j-1,j} R_{j,j+1} \exp(id_j q_j)}, \tag{2.50}$$

with $r_{j-1,j}$ the Fresnel reflection coefficient of the interface between $(j-1)$-th and j-th layers, d_j the thickness of the j-th layer, and q_j the j-th scattering vector [55].

Exemplary XRR curves for different models are shown in Fig. 2.9. They show the difference between a substrate response, the response of a single layer on a substrate, as well as the response of a multilayer system on a substrate. One can see that up to the scattering vector q_c, which corresponds to the critical angle α_c, occurs total reflection. It follows

$$q_\mathrm{c} = \frac{4\pi}{\lambda} \sin(\alpha_\mathrm{c}) \,. \tag{2.51}$$

In the single layer system, the reflected waves at the two interfaces interfere either constructively or destructively. This results in the so-called Kiessig-fringes. From the spacing of the oscillations

Δq, the thickness of the film can be inferred. It follows that

$$d \approx \frac{2\pi}{\Delta q}. \tag{2.52}$$

In the multilayer system, the waves interfere at all interfaces and overlap, so that it is no longer easy to determine a film thickness. For this reason, an in-house developed fitting tool [55] was used to simulate the experimental data with models. For this purpose, parameters such as layer thickness, dispersion/absorption, and interface roughness were varied to find the best possible fits. The

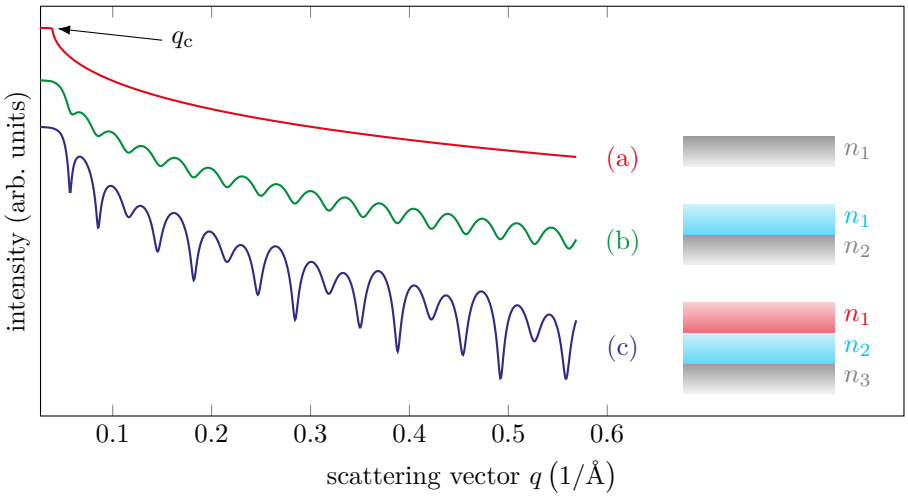

Fig. 2.9: Exemplary profile for theoretical XRR curves for different cases: (a) profile of a pure substrate. (b) Curve of a single layer on a substrate. (c) Curve of a two-layer system on a substrate. All materials have different refractive indices n_1, n_2 and n_3. The surrounding environment is always vacuum with a refractive index of $n_{\text{vac}} = 1$. q_c indicates the critical angle. To better compare the XRR curves they are vertically shifted. Idea and data taken from [40].

interface roughness σ has a considerable influence on the theoretical curve of the reflection curves and always occurs in real interfaces. The reason for the occurrence of roughness is, among other things, structural defects, causing an uneven interface and thus continuously changing the refractive index. In practice, the application of the Névot-Croce method has proven to be effective [56], whereby the Fresnel coefficient is given by

$$\tilde{r}_{j-1,j} = r_{j-1,j} \exp\left(-2k_{z,j-1}k_{z,j}\sigma_j^2\right) \tag{2.53}$$

can be modified. The exponential term causes an attenuation of the reflectivity and is called the Névot-Croce factor [56]. It should be noted, however, that this model is valid only for roughnesses that are very small relative to the respective layer thickness.

The information for this chapter can be found in [32, 52, 53, 57]. These references are also recommended as further reading.

2.4 Low-energy electron diffraction

Low-energy electron diffraction (LEED) is used to characterize crystal surface structure and morphology. The basic principle is electron diffraction, where the diffraction pattern of the interfering electron waves is interpreted. The resulting intensity distribution of the diffracted electron beam delivers information about the ordering on the surface and the structure of the surface unit cell.

In order to perform LEED measurements, the magnitude of the wavelength of the electrons used is very important. The so-called de-Broglie wavelength of the electron waves can be determined via

$$\lambda_{\mathrm{dB}} = \frac{h}{\sqrt{2m_{\mathrm{e}}E}}, \tag{2.54}$$

with h as Planck-constant, m_{e} the mass of the electrons and E the respective electron energy. For a diffraction pattern to appear, the backscattered electron waves must be of the same order of magnitude as the atomic distances in the crystal. This means that the electron waves should be in a range of about $1-2\,\text{Å}$, which corresponds to an electron energy of about $30-200\,\mathrm{eV}$. Considering electrons with such a low energy in combination with the inelastic mean free path in solids which is very small, this leads to a very high surface sensitivity.

Having this in mind, the surface contributing to the elastically backscattered electrons has only a two dimensional character, so the periodicity in the vertical direction can be neglected. Moving from real space to reciprocal space, the vertical lattice constant, which was infinite in real space, becomes reciprocal lattice points infinitely close to each other in reciprocal space. Hence it follows that during diffraction at a two dimensional lattice so called Bragg rods are observed. These have only in lateral direction a periodicity of the reciprocal lattice (cf. Fig. 2.7).

If the electron waves interfere constructively after being diffracted, diffraction spots appear in the LEED image. Constructive interference arises if the Laue condition for perpendicular incidence

$$\vec{q}_{\parallel} = \vec{k}_{\mathrm{f},\parallel} - \vec{k}_{\mathrm{i},\parallel} = \vec{k}_{\mathrm{f},\parallel} = \vec{G}_{\parallel} \tag{2.55}$$

is fulfilled. $\vec{q}_{\parallel}$ is described as the parallel scattering vector, $\vec{k}_{\mathrm{i},\parallel}$ the parallel component of the incoming wave vector, $\vec{k}_{\mathrm{f},\parallel}$ the parallel component of the wave vector of the scattered wave and $\vec{G}_{\parallel}$ the parallel reciprocal space vector. This means that every contribution perpendicular to the surface $\vec{q}_{\perp}$ has no effect on the Laue condition.

To visualize the Laue condition in 2D and the resulting emergence of reflections, the so-called Ewald construction (cf. Fig. 2.10) is used. This figure shows the Ewald construction for an incoming electron beam with the corresponding wave vector $\vec{k}_{\mathrm{i}}$ pointing along the (00) direction (normal incidence). Due to elastic scattering the radius of the Ewald sphere is determined by the magnitude of the wave vector $\left|\vec{k}_{\mathrm{i}}\right| = \left|\vec{k}_{\mathrm{f}}\right|$. The Laue condition states that diffraction spots arise only when the Ewald sphere intersects the reciprocal lattice rods. Since the angle of incidence of the electron beam is fixed in LEED experiments, the scattering conditions can only be obtained by changing the energy of the beam. Thus, if the energy of the electron beam is increased, the radius of the Ewald sphere also becomes larger. As a result, more diffraction rods are intersected and, therefore more reflections can be observed on the LEED screen at a higher energy.

The information for this chapter stems from [31, 33, 58].

2.5 X-ray photoelectron spectroscopy

In the following chapter, the method of X-ray photon spectroscopy (XPS) is introduced. For this purpose, basic information is first introduced after that spectral properties such as chemical shift or satellites are explained. Finally, in the last part, the quantitative evaluation and the property of the depth profiles are described.

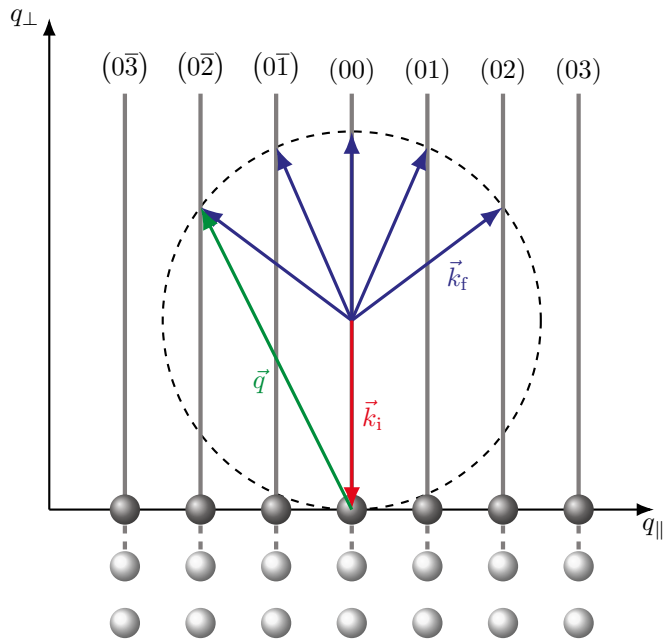

Fig. 2.10: Construction of the Ewald sphere, shown as a dashed circle, for diffraction on a two-dimensional lattice. The incoming wave vector $\vec{k}_i$ incident normal to the surface, as is usual for LEED experiments. The Ewald sphere is defined by all possible final wave vectors $\vec{k}_f$. Diffraction spots always occur only where the Ewald sphere, and therefore the scattering vector $\vec{q}$, intersects the diffraction rods (solid lines). For convenience only the plane with $h = 0$ is shown. Adapted from [40].

2.5.1 General information

In order to analyze the electronic structure of occupied states in surfaces, X-ray photoelectron spectroscopy is used. The basis for this phenomenon was the discovery of the photoelectric effect by Heinrich Hertz in 1887 [59]. He found that an electrostatically charged metal plate emits electrons faster when irradiated with UV light. In other words, an electron in the high-energy continuum state is released by a photon. The relation $E_{\mathrm{Ph}} = h\nu$ was further explained by Albert Einstein in 1905 [60]. In the absence of external effects, the electrons are in the ground state and are bound with binding energy E_b. By irradiation with photons there is the possibility that electrons with the kinetic energy E_{kin} are released. Here it is important that the excitation energy must be large enough to exceed the material-specific work function Φ_A. This results in the energy equation

$$E_{\mathrm{kin}} = h\nu - E_b - \Phi_A, \tag{2.56}$$

with Φ_A as

$$\Phi_A = E_{\mathrm{vac}} - E_F, \tag{2.57}$$

with E_F the Fermi energy and E_{vac} the energy in vacuum. From the foregoing equation, it can be seen that the binding energy can be determined in the experiment provided that E_{kin}, Φ_A and the respective excitation energy are known. For this purpose, the number of triggered electrons is measured as a function of kinetic energy. In order for the emitted electrons to be detected, the energy barrier of the spectrometer (Φ_{spec}) must also be exceeded. Hence, for the kinetic energy E'_{kin} at which the electrons are detected, it holds

$$E'_{\mathrm{kin}} = h\nu - E_b - \Phi_{\mathrm{spec}}. \tag{2.58}$$

Due to the conservation of energy, the binding energy measured by XPS is the energy difference between the initial state with n electrons and the final state with $n-1$ electrons. From this follows

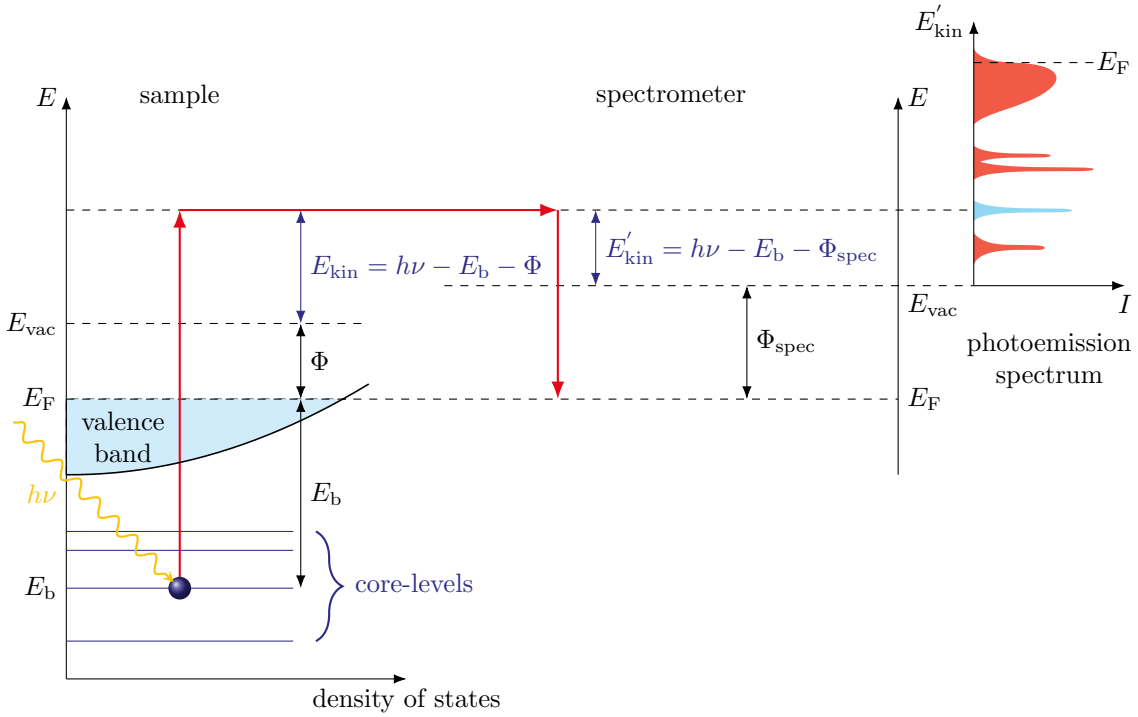

Fig. 2.11: Illustration of the photoelectron emission process using an energy level diagram. The left side shows the sample excited by X-rays with energy $h\nu$. This causes an electron to be emitted. The energy diagram of the spectrometer is drawn on the right side. Spectrometer and sample are set to the same potential so that the Fermi energies match. This allows the kinetic energy of the electron to be measured via $E_{\mathrm{kin}}^{'} = h\nu - E_{\mathrm{b}} - \Phi_{\mathrm{spec}}$. Adapted from [40,61].

the relation

$$E_{\mathrm{b}} = E_{\mathrm{f}}(n-1) - E_{\mathrm{i}}(n). \tag{2.59}$$

The observed binding energy of the emitted photoelectron is approximately equal to the negative orbital energy ε_{k} if no rearrangement of electrons occurs during the process. This approximation is called Koopmans theorem [62]. Using the Hartree-Fock method, the orbital energy can be calculated. In practice, there are some processes that are not considered in the theoretical calculations. These include the fact that electrons do not remain frozen during the photoemission process, but respond to the excitation process by minimizing or shielding the energy of the ionized atom. This energy reduction is called relaxation energy, differentiating between atomic relaxation and extra-atomic relaxation. In the former, one refers to atoms containing the core hole and in the latter, to surrounding atoms. Furthermore, the Koopmans/Hartree-Fock model does not take into account relativistic effects and electron correlations, which are in any case so small as to be negligible.

XPS is an element-specific measurement method, since the atomic binding energies are characteristic for the respective elements. Scattering processes (elastic and inelastic) take place as the electrons travel through the solid, with energy losses occurring during inelastic scattering. If the energy losses are small enough so that the electrons have sufficient kinetic energy to leave the sample, this results in a continuous background signal in the photoemission spectrum. Here, the so-called inelastic mean free path (IMFP) is an important factor. It is a material-specific parameter that is also significantly influenced by the kinetic energy of the electrons. If X-rays are used in the range of $h\nu < 3\,\mathrm{keV}$, soft XPS is referred to. This is a frequently used measurement method, especially in the laboratory environment. Since the inelastic mean free path length at the deployed

kinetic energies is very small, namely in the range of a few nanometers, it is a very surface-sensitive technique. This contrasts with the use of hard X-rays, having much higher kinetic energies. As indicated above, increasing the kinetic energy of the X-rays leads to an increase in IMFP. This makes the signal more sensitive to volume, providing additional information about the composition of the film in deeper layers. This is then referred to as hard X-ray photoelectron spectroscopy (HAXPES).

2.5.2 Spectral features

In the following subsection the spectral features like chemical shift, spin-orbit coupling, satellites and multiplet-splitting are briefly explained.

Chemical shift

Compared to the free atom, the binding energies of compounds can exhibit a shift in the XP spectrum. This is called a chemical shift and occurs because chemical bonds that change the electrostatic shielding of the nuclei charge because electrons are formally removed or added. This affects the binding energy of the core level electrons. Thus, from the chemical shift, a statement can be made about the valence state of a cation species. If electrons are removed from cations, the binding of the remaining electrons to the nucleus increases.

Spin-orbit coupling

As is known from the photoexcitation process, after the excitation of an electron, a hole is created at the same core level. This hole has a spin of $s = 1/2$ and an angular momentum of $l = 0, 1, 2, ...$ (corresponding to the $s, p, d, ...$ orbital). The combination of spin and angular momentum of the electron can be expressed in terms of the total angular momentum $j = l \pm s$. This in turn leads to a splitting of the energy into a double-peak structure, but only in the case $l > 0$. In practice, this leads to the Fe $2p$ state, for example, being split into the spin-orbit split photoelectron peaks Fe $2p_{3/2}$ and Fe $2p_{1/2}$ and being clearly distinguishable. Furthermore, an intensity ratio, from the degeneracy $2j + 1$, can be given between these two peaks. The relation

$$\frac{I_{l-s}}{I_{l+s}} = \frac{2j_{l-s} + 1}{2j_{l+s} + 1} = \frac{l}{l + 1} \tag{2.60}$$

yields ratios of $1 : 2$ (p-shell), $2 : 3$ (d-shell), and so on.

Satellites

When observing the XP spectra, in addition to the splitting of the photoelectron peaks, so-called satellites can occur, which typically are located at higher binding energies. A distinction is made between so-called shake-up, shake-off and charge-transfer satellites, which will be described in more detail below. Shake-up satellites occur when photoelectrons lose energy by excitation of valence electrons from an occupied state into an unoccupied, higher-energy state. When the photoelectron donates enough energy to the valence electron and excites it to the continuum, a shake-off satellite is present. The last type of satellite, so-called charge-transfer satellites usually occur in transition metal oxides or ferrites. The reason for this is the change of the electron configuration of the d-shell of the transition metal, which takes place by transfer of an electron from the ligand (oxygen) into mentioned shell.

Multiplet splitting

Multiplet splitting occurs due to spin coupling of unpaired electrons (or holes) in the core levels of the atom after photoemission with unpaired electrons in the valence band. This results in a variety

of final state configurations because additional effects must be considered as well. These include spin-orbit splitting and charge-transfer. Such effects can lead to a large number of photoemission lines, so-called multiplets. However, for electrons released from shells other than the s orbital ($l > 0$), these lines are usually close together and form the total photoemission lines by overlap.

2.5.3 Quantitative analysis and depth profiling

The main application of XPS, besides the analysis of valence states, is the determination of stoichiometry in the surface region of thin films. Here, the area under the photoemission spectrum is calculated and related to the amount of the respective element. As described above, however, the actual signal is overlaid by a background signal that must first be subtracted. A common method is the correction via the so-called Shirley background [63], which was used in this work. Albeit, the calculation is not that trivial, because parameters of the X-ray source and spectrometer must be taken into account and factors such as effective cross section and mean free path of the excited electrons must be included in the calculation. The signal for photoelectrons from the orbital j of element i from a thin film of thickness d_f is defined via [64, 65]

$$I_{ij} = S_i^j \int_0^{d_\mathrm{f}} e^{-z/\lambda_i^{'}} dz = S_i^j \lambda_i^{'} \left(1 - e^{-d_\mathrm{f}/\lambda_i^{'}}\right). \tag{2.61}$$

Here S_i^j denotes the sensitivity factor, z defines the depth from which the photoelectrons are emitted and λ_i the IMFP of the respective element. In addition, to establish a dependence with the angle φ between the detector and the surface normal, $\lambda_i^{'} = \lambda_i \cos(\varphi)$ can be defined (effective IMFP). To calculate the IMFP of the photoelectrons, the TPP-2M formula of Tanuma, Powell, and Penn has been established [66]. If the sample under investigation consists not only of one layer but of a multilayer system, the intensity attenuates exponentially through the overlying layers according to Lambert-Beer's law. The bulk intensity for a n-multilayer (m) system is calculated via

$$I_\mathrm{b}^\mathrm{m} = S_\mathrm{b}^j \lambda_\mathrm{b}^{'} \prod_{i=1}^{n} e^{-d_i/\lambda_i^{'}}, \tag{2.62}$$

where $S_\mathrm{b}^j \lambda_\mathrm{b}^{'}$ is the unattenuated intensity of the bulk material in the case of an infinitely thick layer (see Eq. (2.61)) and d_i the thickness of the respective layer. In addition, the intensity of a layer f covered by $(n - f)$ layers can also be calculated.

$$I_f^\mathrm{m} = S_f^j \lambda_f^{'} \left(1 - e^{-d_f/\lambda_i^{'}}\right) \prod_{i=f+1}^{n} e^{-d_i/\lambda_i^{'}} \tag{2.63}$$

is valid. Since the effective inelastic mean free path $\lambda_i^{'}$ is angle dependent, depth profiles can be obtained by varying the angle between the detector and the surface normal. For large angles φ, the effective IMFP decreases and thus the surface sensitivity increases. This allows the chemical compositions to be determined at the surface and also for deeper layers. In practice, the sample holder is tilted here and thus the desired angle is set. In this work, this was used especially for angle-resolved HAXPES measurements (see Chap. 4.3.2). In the previously mentioned equations, the so-called sensitivity factor S_i^j occurs, which is calculated for electrons from the orbital j of an element i (or in Eqs. (2.62) and (2.63) from the bulk and film, respectively) is given by

$$S_i^j = \Phi(h\nu) D(E_\mathrm{kin}) n_i A \sigma_i^j(h\nu). \tag{2.64}$$

In the equation, $\Phi(h\nu)$ is the flux of incoming X-rays with energy $h\nu$, and $D(E_{\mathrm{kin}})$ is the efficiency of the spectrometer. n_i indicates the number of atoms per unit volume and element i, and A is the effective area of the sample under investigation. $\sigma_i^j(h\nu)$ denotes the photoelectric cross section for subshells of photoelectrons, which in turn is defined via

$$\sigma_i^j(h\nu) = \int \frac{d\sigma_i^j(h\nu)}{d\Omega} d\Omega. \tag{2.65}$$

In it, $d\sigma_i^j/d\Omega$ denotes the differential photoelectric cross section and $d\Omega$ the differential solid angle. The variables of photon flux as well as sample area are usually constant and thus cancel out in the calculation of intensity ratios. They can therefore be neglected. Furthermore, it is only necessary to consider the transmission $D(E_{\mathrm{kin}})$ of the lens system, since in the fixed-analyzer-transmission mode of operation all incoming photoelectrons are decelerated to a constant transmission energy E_{p}. The factor depends on the kinetic energy, but this can also be neglected if the elements under consideration are close to each other. The transmission function of the lens system is usually given by the manufacturers. The differential photoelectric cross section $d\sigma_i^j/d\Omega$ from Eq. (2.65) can be described via the electric dipole approximation. In the following, a distinction is made between circularly polarized/unpolarized [67] (Eq. (2.66)) and linearly polarized [68] (Eq. (2.67)) X-rays. This results in an angle-dependent distribution of photoelectrons. The equations are as follows:

$$\frac{d\sigma_i^j(h\nu)}{d\Omega} = \frac{\tilde{\sigma}_i^j(h\nu)}{4\pi}\left[1 - \frac{\beta_i^j(h\nu)}{2} P_2\left(\cos(\vartheta^*)\right)\right] \tag{2.66}$$

$$= \frac{\tilde{\sigma}_i^j(h\nu)}{4\pi}\left[1 + \beta_i^j(h\nu) P_2\left(\cos(\vartheta)\right)\right]. \tag{2.67}$$

Wherein $\tilde{\sigma}_i^j(h\nu)$ is the total photoelectric cross section and $\beta_i^j(h\nu)$ is the dipolar angular distribution parameter. $P_2(\cos(\vartheta))$ and $P_2(\cos(\vartheta^*))$ are second-order Legendre polynomials, with ϑ and ϑ^* as the polarization angle and angle between incident X-ray beam and exit direction of photoelectrons, respectively. Usually, the angle between the X-ray source and spectrometer is set to a value of 54.7° and unpolarized X-rays are used. Thus, the factor $P_2(\cos(\vartheta^*))$ need not be considered. The effective cross sections σ_i^j according to Scofield are tabulated in reference [69]. In contrast to soft-XPS, for example, additional non-dipole parameters must be considered in HAXPES, where much higher photon energies are used [70]. From this, again distinguishing between circularly polarized/non-polarized (Eq. (2.68)) and linearly polarized (Eq. (2.69)) X-rays, the following relationships holds [71]:

$$\frac{d\sigma_i^j(h\nu)}{d\Omega} = \frac{\tilde{\sigma}_i^j(h\nu)}{4\pi}\left[1 - \frac{\beta_i^j(h\nu)}{2} P_2\left(\cos(\vartheta^*)\right) + \left(\frac{\gamma_i^j(h\nu)}{2}\sin^2\left(\vartheta^*\right) + \delta_i^j(h\nu)\right)\cos\left(\vartheta^*\right)\right] \tag{2.68}$$

$$= \frac{\tilde{\sigma}_i^j(h\nu)}{4\pi}\left[1 + \beta_i^j(h\nu) P_2\left(\cos(\vartheta)\right) + \left(\gamma_i^j(h\nu)\cos^2(\vartheta) + \delta_i^j\right)\sin(\vartheta)\cos(\vartheta)\right], \tag{2.69}$$

in which γ_i^j and δ_i^j are the non-dipole parameters and φ is the angle between the X-ray beam and the projection to the normal plane of the X-ray polarization of the exit direction of the photoelectrons. Values for the previously mentioned parameters can be found in the work of Trzhaskovskaya *et al.* [72, 73].

2.6 X-ray absorption spectroscopy

The X-ray absorption spectroscopy (XAS) measurement method is based on the internal photoelectric effect. This means that the core electrons are excited by X-rays into unoccupied states in the band structure of the respective material. Lambert-Beer's law defines how much intensity I is transmitted through a sample of thickness d. It is

$$I(h\nu) = I_0(h\nu)e^{-\mu(h\nu)d}. \tag{2.70}$$

Therein I_0 indicates the initial intensity and μ the energy-dependent absorption coefficient. Using this equation, the absorption coefficient can be determined, but it must be noted that the so-called X-ray effective attenuation length (EAL) is in the range of µm, for the case when the X-rays penetrate solids. The determination is therefore only possible for very thin samples without the beam being completely attenuated before it has completely penetrated the sample. Another way to perform XAS is to observe the decay (radiative or electronic) of excited core electrons. After excitation to a higher energy state, a hole is created which is filled by recombination. This energy excess is released again either via fluorescent X-rays or secondarily excited Auger electrons. Hence, the two measurement modes total fluorescence yield (TFY) or total electron yield (TEY) are obtained. For the evaluation, the latter case is preferably used, whereby here basically electrically conductive materials must be present. In fact, during the Auger decay, further electrons are excited and a sequence of electrons is formed, which is measured as a drain current. The disadvantage of the TFY mode is that saturation effects often occur [74, 75]. Nevertheless, this mode is well suited to study deeper layers because the mean free path of photons in fluorescence have about the same order of magnitude as the incident beams. This is in contrast to the TEY mode, because the mean free path of the electrons is relatively small, only the layers close to the surface are observed and less depth information is provided. The XAS process is shown schematically in Fig. 2.12.

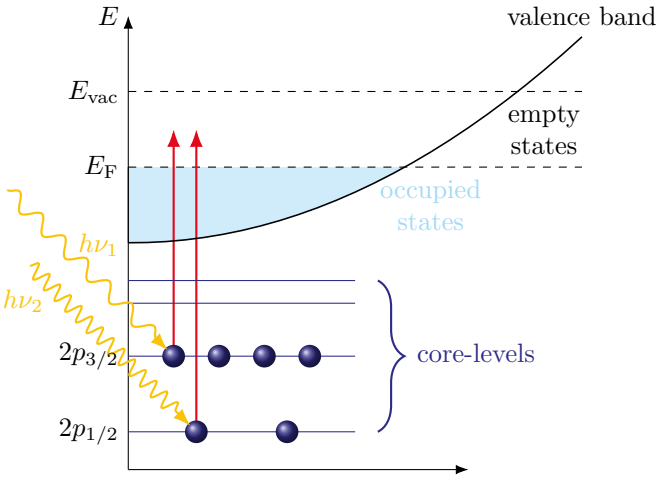

Fig. 2.12: Illustration of the XAS principle. Electrons are excited from the split $2p$ orbital into unoccupied states above the Fermi level (E_F) in the valence band. Depending on how large the excitation energy is, the electrons can be excited from the $2p_{3/2}$ or $2p_{1/2}$ state. For excitation from the energetically lower state ($2p_{1/2}$), a higher energy must be applied ($h\nu_2$) than for the $2p_{3/2}$ state ($h\nu_1$). Adapted from [40, 76].

The information for this chapter stems from [53, 77].

2.7 X-ray magnetic circular dichroism

X-ray magnetic circular dichroism (XMCD) refers to the difference in absorption (XAS) of circularly polarized X-rays with positive and negative helicity in magnetized ferro/ferrimagnetic samples. It

is valid

$$\Delta\mu = \mu_+ - \mu_-, \tag{2.71}$$

with μ_+ as absorption at right-circular (σ_+) and μ_- at left-circular (σ_-) polarized X-rays, respectively. The theoretical fundament for the XMCD principle was laid in 1975 by Erskine and Stern [78], before Schütz *et al.* confirmed it also experimentally [79]. The basis for this is the fact that absorption process is spin dependent. This can be explained with the help of the so-called two-step model [80]. This model is shown schematically in Fig. 2.13. First, photoelectrons are generated by absorption of the exciting circularly polarized X-rays. These photons have spin or angular momentum, which is transferred either partially or completely (in the case of s orbitals) to the orbital momentum of the electron. If split states are excited, such as the $2p_{3/2}$ state, the angular momentum is additionally transferred to the spin. The reason for this is the spin-orbit coupling. Thereby, preferential excitation of electrons of a special spin type occurs, resulting in spin-polarized, excited photoelectrons. This is called the Fano effect [81, 82]. At the absorption edges L_2 ($2p_{1/2}$) and L_3 ($2p_{3/2}$) there is an opposite spin polarization because of $l \pm s$. This is determined by the spin orientation of the polarized x-rays.

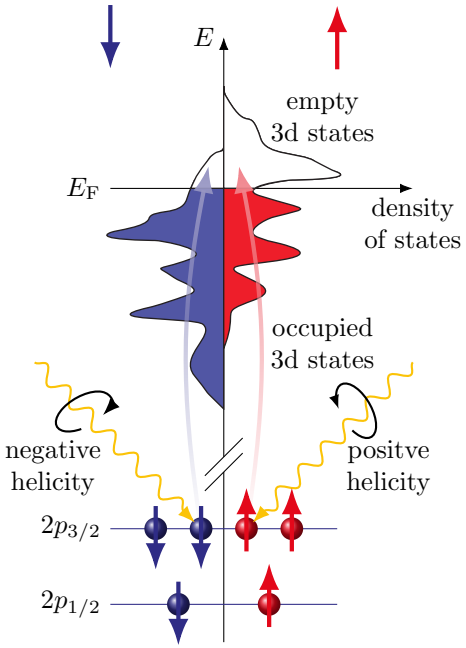

Fig. 2.13: Schematic sketch of the XMCD principle of a magnetized $3d$ transition metal. The illustration is based on the spin-up and spin-down orientation of the electrons at the L_3 absorption edge. Due to the different polarizations (left or right circular) of the X-rays, the released electrons are spin polarized. The conduction band is therefore split into spin-up and spin-down states, creating a type of spin detector. Adapted from [40, 83].

For the second step, the valence shell is considered first. In magnetized materials, there is an imbalance in the number of occupied states with spin-up or spin-down. Consequently, the valence shell always prefers electrons with a special spin orientation and this is then also visible in the XMCD signal. It can be concluded that the valence shell acts like a spin-sensitive detector. Thus, it follows directly from the considerations made previously that magnetic dichroism can only exist when there is an imbalance of spin-up and spin-down states. The largest XMCD signal is present if, for example, all spin-down states are complete and all spin-up states are unoccupied.

2.7.1 Sum rules

Using the so-called sum rules, the XMCD data can not only give indications about the chemical and electronic structure, but also provide the magnetic spin and orbital moment of the respective element. They were developed by Thole *et al.* and Carra *et al.* [84, 85] and finally verified by Chen

et al. [86]. As described above, the XMCD signal is directly related to the spin-up and spin-down states and therefore directly related to the magnetic spin moment m_s. Furthermore, the XMCD signal incorporate also the orbital moment m_o of the $3d$ shell, so that in consequence the two contributions overlap. The spin and orbital moments can be determined by simply integrating the L_2 and L_3 absorption edges from the XAS/XMCD data. For orbital moment,

$$m_o = -\frac{4\int_{L_3+L_2}(\mu_+ - \mu_-)dE}{3\int_{L_3+L_2}(\mu_+ + \mu_-)dE}(10 - n_{3d}) \tag{2.72}$$

$$= -\frac{4q}{3r}(10 - n_{3d}) \tag{2.73}$$

is obtained, where q is the integral over the $L_{3,2}$ edge of the XMCD signal and r in turn is the integral over the $L_{3,2}$ edge of the XAS signal. n_{3d} gives the number of holes of the $3d$ states of the respective transition metal. For the spin moment, the equation

$$m_s = -\frac{6\int_{L_3}(\mu_+ - \mu_-)dE - 4\int_{L_3+L_2}(\mu_+ - \mu_-)dE}{\int_{L_3+L_2}(\mu_+ + \mu_-)dE}(10 - n_{3d})\left(1 + \frac{7\langle T_z\rangle}{2\langle S_z\rangle}\right)^{-1} \tag{2.74}$$

$$= -\frac{6p - 4q}{r}(10 - n_{3d})\left(1 + \frac{7\langle T_z\rangle}{2\langle S_z\rangle}\right)^{-1} \tag{2.75}$$

is valid, in which p corresponds to the integral over the L_3-edge of the XMCD signal. With $\langle T_z\rangle$ and $\langle S_z\rangle$ the expectation values of the ground state of the magnetic dipole operator, respectively the spin operator are given. In the volume of cubic crystals, $\langle T_z\rangle$ is often so small that the factor $\langle T_z\rangle/\langle S_z\rangle$ can be neglected. The units of m_o and m_s are given in μ_B/atom. To correct the data, a step function is subtracted from the XAS signal before applying the sum rules, so it is assumed that only transitions from the $2p$ to the $3d$ state occur and the rest are excited into the continuum [77].

2.7.2 Charge-transfer multiplet theory

$3d$ Transition metal cations are surrounded by anions called ligands. This makes it difficult to describe their behavior with pure atomic multiplet theory, unlike for rare earths, for example. To reconcile transition metal oxides or ferrites with theoretical calculations of multiplet structure, additional effects such as crystal field (also called ligand field) and charge-transfer must be considered. Depending on the strength of the crystal field and the symmetry of the ligands, the crystal field causes the degenerate energetic states of the cation to split. The charge-transfer comes from charge fluctuations between the oxygen anions and the binding cations. The two effects are briefly described below. For more information on this topic, please refer to [77].

Ligand field splittings

In ligand field theory, two cases have to be differentiated. If a transition metal cation is isotropically surrounded by charges of, for example, oxygen ligands, this corresponds to the model idea of a spherical electrostatic field in the center where the cation is located. Compared to a free cation, this state is energetically more advantageous due to Coulomb repulsion of the electrons of cation and ligand. In addition, there is no splitting of the energy states. In the second case, however, it is assumed that the ligands reside at special positions such as octahedral or tetrahedral sites, and thus the electrostatic field is anisotropic. This results in energy splitting, which is called ligand field splitting or crystal field splitting. It causes a decrease in the energy of the orbitals between the bond directions and an increase in the energy of the orbitals directed toward ligands. In the present material systems (spinel-like ferrites) in octahedral coordination, the lower energy levels are called

t_{2g}-levels and the higher energy levels are called e_g-levels. Whereas in tetrahedral coordination, the higher states are called t-level and the lower states are called e-level. A very essential factor in the computation of multiplet calculations is the difference between the energetically degenerate states. It is denoted by $10Dq$. As a rough estimate, it is larger for octahedral coordination than for tetrahedral coordination.

Charge-transfer

As indicated above, there is a charge-transfer in transition metal oxides. In this case, there is the possibility that the $2p$ electron of ligand anions remains in its orbital and is not shifted into the $3d$ orbital of the respective cation, which corresponds to a partial charge-transfer. This can be achieved computationally by considering that N electrons in the $3d$ state are no longer described by the representation $3d^N L$ but rather must be expressed by a linear combination of $3d^N L$ and $3d^{N+1}L^{-1}$. The difference between the two states is Δ_i. An attractive potential U_{pd} is formed by the core hole in the $2p$ state due to the excitation to a higher state. This gives a new $3d$ final state composed of the $2p^5 3d^{N+1}L$ and $2p^5 3d^{N+2}L^{-1}$ states. The energy difference between these two states can be calculated via

$$\Delta_\mathrm{f} = \Delta_\mathrm{i} + U_{dd} - U_{pd}, \tag{2.76}$$

where U_{dd} is used to specify the Coulomb repulsion of the excited electron by the other $3d$ electrons. All previously mentioned parameters Δ_i, Δ_f, U_{pp} and U_{pd} are essential for the charge-transfer-multiplet calculations.

For further information please refer to [77].

2.8 Matter in magnetic fields

To describe magnetism, general principles are first introduced before magnetism in solids is discussed in more detail. Magnetization curves are then discussed. This is followed by a more detailed explanation of magnetic domains and domain walls.

2.8.1 Basic principles[1]

Naturally, all materials have atomic magnetic moments $\vec{m}$, which are responsible for the magnetism of a material. Either a material is already magnetized by this or it is yet to be magnetized. An external magnetic field $\vec{B}_\mathrm{ext}$ can align or initially create existing magnetic moments. On the macro level, the sum of all magnetic moments per volume V is called magnetization $\vec{M}$. Hence,

$$\vec{M} = \frac{1}{V}\sum_j \vec{m}_j. \tag{2.77}$$

Experiments have revealed that the magnetization for low fields is directly proportional to the magnetic field strength $\vec{H}$ with

$$\vec{M} = \chi \vec{H}. \tag{2.78}$$

The proportionality factor χ is called magnetic susceptibility. This is a material and temperature dependent factor and generally decreases with increasing temperature.

[1] Translated from [87].

Since magnetism is generally considered in matter, it is necessary to define the magnetic flux density, or magnetic induction $\vec{B}$. It is related to the magnetic field strength by the proportionality factor μ_0. For the case in vacuum,

$$\vec{B} = \mu_0 \vec{H}. \tag{2.79}$$

The proportionality factor is called permeability constant and has the numerical value $\mu_0 = 4\pi \times 10^{-7}\ \mathrm{V\,s\,A^{-1}\,m^{-1}}$. If the surrounding medium changes from vacuum to matter, the permeability constant is supplemented by a matter-dependent, dimensionless constant, the so-called relative permeability number μ. From this follows for the magnetic flux density

$$\vec{B} = \mu\mu_0 \vec{H} = \mu_0 \left(1 + \chi\right) \vec{H}. \tag{2.80}$$

Furthermore, this results in the relation

$$\mu = 1 + \chi \tag{2.81}$$

for the susceptibility χ and the relative permeability number μ. Finally, another expression for the magnetic flux density can be found by combining the previously mentioned equations. One obtains

$$\vec{B} = \mu_0 \left(\vec{H} + \vec{M}\right). \tag{2.82}$$

2.8.2 Magnetism in solids[2]

Depending on the sign and value of the magnetic susceptibility, materials are classified with respect to their magnetic properties. A distinction is made between

- diamagnetism $\left(10^{-9} < |\chi| < 10^{-6},\ \text{with } \chi < 0\right)$,
- paramagnetism $\left(10^{-9} < |\chi| < 10^{-4},\ \text{with } \chi > 0\right)$,
- ferromagnetism $\left(10^{2} \leq |\chi| \leq 10^{5},\ \text{with } \chi > 0\right)$ and
- antiferromagnetism $(0 \leq |\chi| \leq 10^{2}, \text{with } \chi > 0)$.

Another indication for the designation of the substances is provided by the orientation of the magnetic moments. The differentiation between ferro-, ferri- and antiferromagnetic materials can be determined according to this orientation. A schematic overview is shown in Fig. 2.14. In the following, an explanation of the different forms will be given.

Diamagnetism

In a diamagnetic material, the atoms or molecules do not have a permanent magnetic dipole moment. However, if this material is subjected to a magnetic field, induced dipoles result whose magnetic field is opposite to the external inducing magnetic field. This is because, due to Lenz's rule, the magnetic field of the induced dipole moments is opposite to the external magnetic field. Considering Eq. (2.78), this results in a negative susceptibility, which is temperature independent. This approximation of the proportionality of Eq. (2.78) is valid only for external magnetic fields which are small compared to the inner-atomic fields [32].

Paramagnetism

Paramagnetism is present in substances whose atoms have permanent magnetic dipoles, with the orientation split over all spatial directions in the absence of an external magnetic field. Therefore,

[2] Translated from [87].

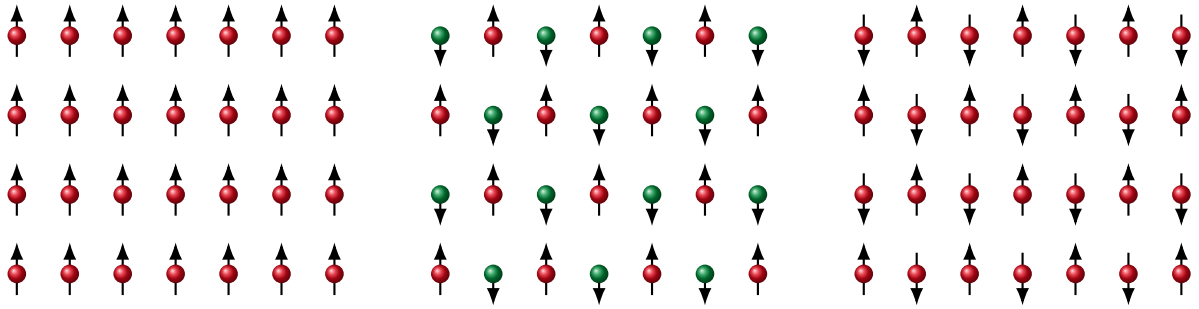

(a) ferromagnetism (b) ferrimagnetism (c) antiferromagnetism

Fig. 2.14: Schematic representation of the orientation and magnitudes of the magnetic moments for different magnetic orders. (a) ferromagnetic: all magnetic moments have the same magnitude and are identically oriented. (b) ferrimagnetic: opposite orientation, but different magnitudes. (c) antiferromagnetic: different orientation with identical magnitudes leads to an overall compensation. Adapted from [88].

on average, the magnetization is given by

$$\vec{M} = \frac{1}{V} \sum \vec{p}_{\mathrm{m}} = \vec{0}, \tag{2.83}$$

where $\vec{p}_{\mathrm{m}}$ is the magnetic dipole moment.

When an external magnetic field is applied, the dipoles partially align. The ratio of dipole potential energy to thermal energy indicates the degree of alignment. For the susceptibility one gets Curie'seasy law

$$\chi = \mu_0 \frac{M}{B} = \frac{\mu_0 N p_{\mathrm{m}}^2}{3 k_{\mathrm{B}} T}, \tag{2.84}$$

with N as the number of dipoles, p_{m}^2 the atomic or molecular dipole moment, and k_{B} the Boltzmann constant. Thus, the susceptibility is proportional to $1/T$. Since the order of moments is considered in the forms of magnetism, disorder occurs due to temperature dependence, resulting in a decrease in susceptibility.

Ferromagnetism

Ferromagnetism refers to a property of materials which, without being exposed to an external field, exhibit magnetic moments. They can therefore be spontaneously magnetized. In this case, the magnetic moments are all identically aligned on the microscopic level even without an external field (cf. Fig. 2.14 (a)). In contrast to paramagnetic materials, the magnetization here can be several orders of magnitude higher. Examples of ferromagnetic materials are, among others, the elements iron, nickel or cobalt used in this work. These are so-called $3d$-transition metals, i.e. they lack electrons to the noble gas configuration and thus the inner spherical shells are not filled up. The susceptibility results directly from the arrangement of the magnetic moments. For ferromagnetic materials the magnitude of the susceptibility is $\gg 1$ with $\chi > 0$. In temperature-dependent measurements, the so-called Curie temperature is of utmost importance. Above this temperature, the thermal energy is greater than the interaction of the atomic magnetic moments, which has the consequence that the order of these moments is destroyed. As a result, a previously ferromagnetic material becomes paramagnetic [32]. The susceptibility can be related to the Curie temperature

via the Curie-Weiss law. For $T \gg T_C$ it holds

$$\chi = \frac{C}{T - T_C}, \tag{2.85}$$

with C the material-dependent Curie constant and T_C as the ferromagnetic Curie temperature. In general, ferromagnetic solids always have a high Curie temperature when the exchange interaction is strong.

Ferrimagnetism

Ferrimagnetism exists when the magnitudes of the sublattice magnetizations are different and their orientations are opposite (cf. Fig. 2.14 (b)). Thus, in the absence of an external field, spontaneous magnetization still remains.

For the susceptibility in ferrimagnets one obtains for $T > T_C$

$$\chi = \frac{(C_A + C_B)\,T - 2\,|\gamma_{AB}|\,C_A C_B}{T^2 - T_C^2}, \tag{2.86}$$

with C_A, C_B the Curie constants and γ_{AB} the molecular field constants of two sublattices A and B. The latter indicates how strong the interaction of a molecular field in a solid with an ion is. For a more detailed derivation, please refer to [31]. Thus, unlike the other types of magnetism, for susceptibility, a curved function results when $\chi^{-1}(T)$ is applied. This is characteristic for ferrimagnets.

Antiferromagnetism

If the magnitudes of the magnetic moments are equal and the orientation is oppositely oriented, i.e., if there is a compensation of the magnetic moments, the substance is antiferromagnetic (cf. Fig. 2.14 (c)) [88]. If an antiferromagnetic material is present, the susceptibility is between $0 < |\chi| < 100$. The counterpart to the Curie temperature in ferromagnetic materials is the antiferromagnetic Néel temperature T_N in antiferromagnetic materials. This can also be related to susceptibility. One obtains for $T > T_N$

$$\chi = \frac{C}{T + \theta_N}, \tag{2.87}$$

with θ_N as the paramagnetic Néel temperature. The two Néel temperatures (antiferromagnetic and paramagnetic) can also be expressed as

$$T_N = \frac{C}{2}\,(\gamma_{AB} - \gamma_{AA}) \text{ and} \tag{2.88}$$

$$\theta_N = \frac{C}{2}\,(\gamma_{AB} + \gamma_{AA})\,, \tag{2.89}$$

with $C_A = C_B = C$. γ_{AA} and γ_{AB} denote the molecular field constants of two sublattices A and B. It turns out that, in general, the Curie-temperatures of the ferromagnets are significantly higher than the Néel temperatures of the antiferromagnets. It follows that the coupling energy is smaller for antiferromagnets than for ferromagnets.

The information for this chapter is taken from [31] and [32].

2.8.3 Magnetization curves[3]

Measuring the magnetic moment $\vec{M}$ of ferro(i)magnetic materials with respect to an external magnetic field $\vec{B}_{\text{ext}} = \mu_0 \vec{H}_{\text{ext}}$ results in so-called magnetization or hysteresis curves. Fig. 2.15 shows an example hysteresis curve with different characteristic points, such as (magnetic) remanence M_{r}, coercive field H_{c} and saturation magnetization M_{s}.

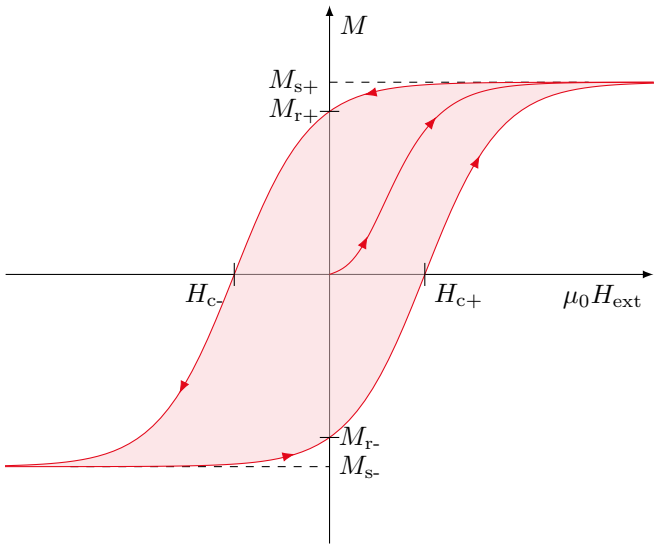

Fig. 2.15: Exemplary shape of a hysteresis curve. The magnetic moment M is measured as a function of the external magnetic field $B_{\text{ext}} = \mu_0 H_{\text{ext}}$. Characteristic points describing the respective material are the saturation magnetization M_{s}, the remanence M_{r} and the coercive field H_{c}. The saturation magnetization is the value approached by the moment for high magnetic fields. Remanence and coercive field describe the intersections with the ordinate, and abscissa, respectively. Adapted from [31].

If all magnetic domains are oriented in the same direction as the externally applied field $\vec{B}_{\text{ext}}$, the saturation magnetization M_{s} is set. The magnetic moment is then maximal and no longer underlies any change when the external field is varied. If the external field is reduced from the maximum value to 0, the remanence (or remanent magnetization) M_{r} describes the magnetic moment which then still remains in the sample. The last characteristic quantity is the coercive field (or coercive force) H_{c}. This is the field strength that must be applied to counteract the remanent magnetization. There are two possibilities that influence the coercive field strength. On the one hand, the coercive field depends on the content of impurities. If these decrease, the coercive field also decreases, since in magnetic films with high defect density higher fields have to be applied to reverse the direction of the magnetic moments in the domains [89]. On the other hand, defects as a result of tensions in the material can influence the coercive field.

A fundamental distinction is made between magnetically soft materials, in which the coercive field is rather low, and magnetically hard materials, which have a rather high coercive field. This also determines the course of the hysteresis. For the magnetically soft materials, these run narrower than for the hard materials, which have a wider opening of the hysteresis. Therefore, the energy that must be invested to force remagnetization is significantly lower for magnetically soft materials than for magnetically hard materials.

The information for this chapter is taken from [31], [90], [37] and [91].

2.8.4 Domain formation[4]

In a ferromagnet there are regions where the orientation of the magnetic moments is identical. These regions are called magnetic domains or Weiss domains. They are the reason why a measurement of the magnetization of a sample results in a moment smaller than the saturation magnetization. For

[3] Translated from [87].
[4] Translated from [87].

$T = 0$, one would expect all magnetic moments to be aligned in parallel, resulting in the saturation magnetization. Thermal fluctuations then also increase with increasing temperature. However, the presence of identical alignment is only within the respective domains, consequently it exists only at the microlevel. Here, the spontaneous magnetization corresponds to the saturation magnetization. Due to the fact that the domains can be aligned differently, there may be a compensation of the moments, which results in a smaller magnetization than the saturation magnetization on the macro level. A schematic representation can be found in Fig. 2.16.

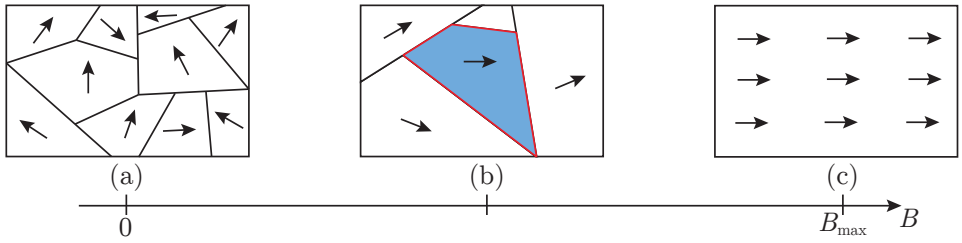

Fig. 2.16: Schematic illustration of Weiss domains. The closed regions are called Weiss domains (shown in blue in (b)). These domains are delimited by the Néel, respectively Bloch walls (shown in red in (b)). In (a) the original state of the material without external magnetic field is shown. From (a) over (b) to (c), the external magnetic field is successively increased. This causes the magnetic moments to align and the domain walls to shift, resulting in an increase in the size of the domains. Once the maximum magnetic field is reached, all magnetic moments are oriented in the same direction and the saturation magnetization M_s is established. The arrows represent the totality of magnetic moments within the domain.

Moreover, in addition to ferromagnetic materials, the phenomenon can also be observed in ferri- and antiferromagnetic materials. In the following, the differences between ferro- and antiferromagnetic domains and the different types of domain walls will be discussed in more detail.

Ferromagnetic domains

In a ferromagnet, domains form due to the minimization of the magnetic free enthalpy density. For this, various energy contributions have to be taken into account. These include contributions from the self-energy E_m due to shape anisotropy, magnetocrystalline anisotropy E_{ani}, and finally the Zeeman energy E_{Zeeman}, which describes the interaction of magnetic particles with external fields. The reason for the formation of domains will be explained by the following figure. In this Fig. 2.17(a) shows a single domain whose magnetization direction is determined based on magnetic anisotropy. It can also be seen that the self-energy associated with the scattered field is particularly large here. This self-energy leads to an increase of the total energy and is always positive. From Fig. 2.17(b) to (c), the formation of domains with antiparallel magnetization directions increases and the energy of the scattered fields decreases accordingly. On the other hand, the formation of domain walls also requires energy, since at their boundaries the spins are antiparallel aligned, leading to a reduction of the exchange energy. To minimize the scattering field energy, it is favorable from an energetic point of view if the antiparallel aligned domains are confined by so-called terminating domains (cf. Fig. 2.17(d)). Accordingly, the domain wall between perpendicular domain and terminating domain is arranged at 45° angle. As a result, the scattered magnetic field outside the solid disappears because the normal components of the magnetization of the domains continuously merge into each other. Furthermore, no magnetic poles appear.

The domain structure can be determined by the total free enthalpy of the system. For this purpose,

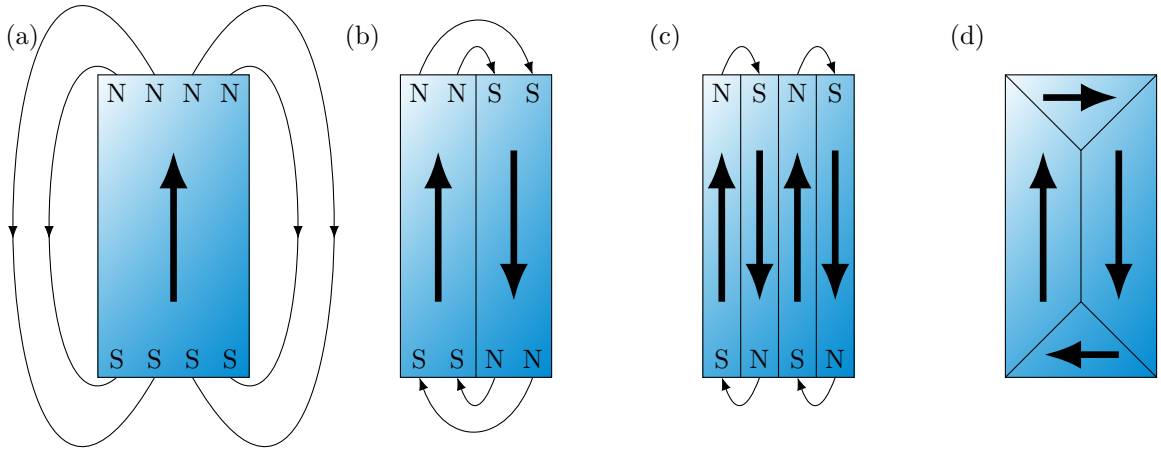

Fig. 2.17: Schematic diagram for the formation of ferromagnetic domains. In (a), a single domain is shown including the scattered field. From (b) to (c), the energy of the scattered fields decreases as more domains with antiparallel magnetization directions are formed. (d) shows antiparallel domains with so-called terminating domains. Adapted from [31].

the respective energy densities, indicated here by lower case letters, are integrated. This yields

$$G_{\text{tot}} = \int \left[e_{\text{shape}} + e_{\text{ani}} + e_{\text{wall}} + e_{\text{Zeeman}} \right] dV. \tag{2.90}$$

Moreover, the additional conditions $\nabla \cdot \vec{B}_{\text{S}} = 0$ and $\nabla \times \vec{B}_{\text{S}} = 0$ originating from the Maxwell equations [92] must be satisfied, resulting in a differential equation that can only be solved numerically.

Domain structures can always be justified by the fact that a magnetic system aims for the state of lowest energy and this can be achieved when a single-domain saturated state transitions to a configuration with a domain arrangement. The shape of the domain structure is ultimately determined by the total energy, which is composed of magnetic field energy, anisotropy energy, and Zeeman energy, and is minimized accordingly.

Antiferromagnetic domains

Since there are no scattered fields in antiferromagnets, a single-domain state is energetically most favorable here. Due to structural defects, such as grain boundaries, not only single-domain but also multi-domain states occur in reality. These structural defects provide a disturbance of the long-range order of the spins and can therefore cause a change in the spin direction. Even in ideal crystals, the entropy can increase due to the formation of domains. If the associated change in free energy is higher than that required to form the domain walls, this multi-domain state becomes thermodynamically stable.

Domain walls

Considering two neighboring magnetic domains, the alignment of the magnetic moments and thus the spins can be very different. The change of spin between two lattice atoms cannot occur abruptly, there are regions in which the alignment change is accomplished. These regions are called domain walls. Depending on the plane in which the change of spin occurs, a distinction is made between Bloch and Néel wall.

If the spin change is parallel to the domain wall plane, it is called a Bloch wall. Energy considerations can be used to make statements about the thickness of the Bloch wall. Ideally, the Bloch

wall is as thin as possible, and the sum of the anisotropy energy and the energy increase due to the exchange coupling is minimal. For example, for iron, the Bloch wall thickness is about 40 nm [31].

Thin films usually do not form Bloch walls because they are energetically unfavorable. The reason for this is that the magnetization direction would have to rotate out of the plane of the film in the region of the domain walls. This would result in a large scattered field (cf. Fig. 2.17), therefore Néel walls are more likely to be formed here. In contrast to Bloch walls, the spin change there is orthogonal to the domain wall plane. For very thin films, however, there is an exception. Since the surface contributions to the magnetocrystalline anisotropy are particularly large there, Bloch walls can still arise.

The information for this chapter is taken from [31]

2.8.5 Collective magnetic ordering

The reason for magnetic ordering is a quantum mechanical effect - the so-called exchange interaction. From the Pauli exclusion principle it follows that electrons with the same spin cannot stay at the same place at the same time, because otherwise their wave functions would overlap. Therefore, the exchange interaction is a quantum mechanical effect that can be interpreted as an electrostatic interaction of electrons close to each other (from neighboring atoms). Considering two electrons, as indicated above, a total wave function Ψ can be given, which consists of a spin part χ and a spatial part ψ. The total spin S of such an arrangement is either $S = 1$ (parallel spin alignment) or $S = 0$ (antiparallel spin alignment). This results in wave functions with a spin triplet state or a spin singlet state. The equations are

$$\Psi_\mathrm{S} = \psi_\mathrm{sym}(\vec{r})\chi_\mathrm{S}(\vec{s}) \text{ and} \tag{2.91}$$

$$\Psi_\mathrm{T} = \psi_\mathrm{asym}(\vec{r})\chi_\mathrm{T}(\vec{s}). \tag{2.92}$$

It can be seen that the wave functions in the triplet state are composed of an antisymmetric spatial part ψ_asym or a symmetric spatial part ψ_sym in the singlet state. With $\vec{r}$ and $\vec{s}$ as spatial and spin coordinates of the electrons, respectively. From the previously mentioned possible configurations, assuming electron-electron interaction, the energies E_S and E_T are also obtained, respectively. Over this the exchange constant J can be defined. It holds

$$J = \frac{E_\mathrm{S} - E_\mathrm{T}}{2}. \tag{2.93}$$

Comparing the two possible states, we see that the triplet state is preferred for $J > 0$ due to the lower energy. The spins are then aligned in parallel, leading to ferromagnetic ordering. The singlet state is energetically more favorable for $J < 0$, leading to antiferromagnetic interaction and antiparallel alignment of the spins. Nowadays, it is common to describe magnetic properties of materials via Hamiltonians. The most commonly used concepts for this purpose are the models of Hubbard [93] and Heisenberg [94], which will not be discussed in detail in the following but reference will be made to the literature. In the case of exchange interaction, one can also differentiate more precisely between direct and indirect exchange. Direct exchange is rather simple: If electrons are close to each other, their wave functions overlap and theoretically a direct interaction can take place, although this is rarely the case, since in many materials this overlap is not sufficient for an interaction. Indirect exchange is more likely to occur, especially in transition metal oxides. There, the exchange occurs via a diamagnetic oxygen ligand, as mentioned above. In indirect exchange, the $2p$ oxygen anion orbitals overlap with the orbitals of the cations of the respective element, thus enabling indirect exchange. It is in the compounds considered here that the special exchange

interactions double exchange [95] and superexchange [96,97] occur. For further information please refer to reference [83,98].

The information for this chapter stems from [32,83,98].

2.9 Superconducting quantum interference device

A superconducting quantum interference device (SQUID) is a highly sensitive instrument for measuring magnetic fields. Two basic effects are necessary for such a detector [31,99]. On the one hand the magnetic flux quantization [100] and on the other hand the so-called Josephson effect [101], which will be explained in the following chapter. First, a brief introduction to superconductivity is made.

2.9.1 Superconductivity

The electrical resistivity of metals depends on scattering processes. The underlying scattering processes are, on the one hand, the scattering of conduction electrons by lattice defects and phonons and, on the other hand, the scattering of electrons between each other. It follows that the resistance decreases with decreasing temperature, since the phonons are restricted in their ability to move and the phase space volume for any electron scattering processes decreases. Nevertheless, even at very low temperatures, there are still lattice defects, impurities, and impurity atoms on which electrons can be scattered, leaving a finite residual resistance. From the temperature-independent effects of Landau diamagnetism and Pauli spin susceptibility, it further follows that the magnetic susceptibility of a metal is also temperature-independent.

In 1911, Heike Kamerlingh Onnes [102] found that below a certain temperature, mercury jumps to an immeasurably small resistance. This temperature is called the transition temperature. Below this temperature a perfect conductor can be found, which gave rise to the term superconductivity. Later, Meißner and Ochsenfeld [103] discovered that superconducting materials are also perfect diamond magnets, i.e. have the susceptibility $\chi = -1$.

2.9.2 Flux quantization

Experiments of Doll [104] and Deaver [105] have shown that the magnetic flux in a superconducting hollow cylinder is quantized in units of the flux quantum

$$\Phi_0 = \frac{h}{2e} = 2.067\,833\,758\,(46) \times 10^{-15}\,\mathrm{V\,s} \tag{2.94}$$

and can only take integer multiples of it. The justification for this quantization is that the macroscopic wave function describing the superconducting state must reproduce itself when the enclosed magnetic flux region is circled once with a coordinate point of the wave function and returns to the starting point (cf. Fig. 2.18). The macroscopic wave function is

$$\Psi(\vec{r},t) = |\Psi(\vec{r},t)|\, e^{i\varphi(\vec{r},t)}, \tag{2.95}$$

where $|\Psi(\vec{r},t)|$ denotes the amplitude and $\varphi(\vec{r},t)$ denotes the phase of the wave function. To ensure exact reproduction after one period, the ring integral must satisfy the condition

$$\oint \nabla\, \varphi\, ds = n2\pi, \qquad \text{with } n \in \mathbb{Z}. \tag{2.96}$$

After introducing the general particle momentum in a magnetic field $m^*\vec{v}_s = \hbar\nabla\varphi - e^*\vec{A}$, with m^* the mass of Cooper pairs [106,107], $\vec{v}_s$ their mean velocity as well as their charge e^* and the vector potential $\vec{A}$ assuming always an integration path (in Fig. 2.18 shown in green) on which $\vec{v}_s = 0$, it follows with the help of the theorem of Stokes [108]

$$\oint \vec{A}\, d\vec{s} = \int \mathrm{rot}\ \vec{A}\, d\vec{a} = \int \vec{B}\, d\vec{a} = n\frac{h}{2e} = n\Phi_0. \tag{2.97}$$

This shows that a flux quantum can only ever occur in integer multiples. For a more detailed derivation please refer to [109].

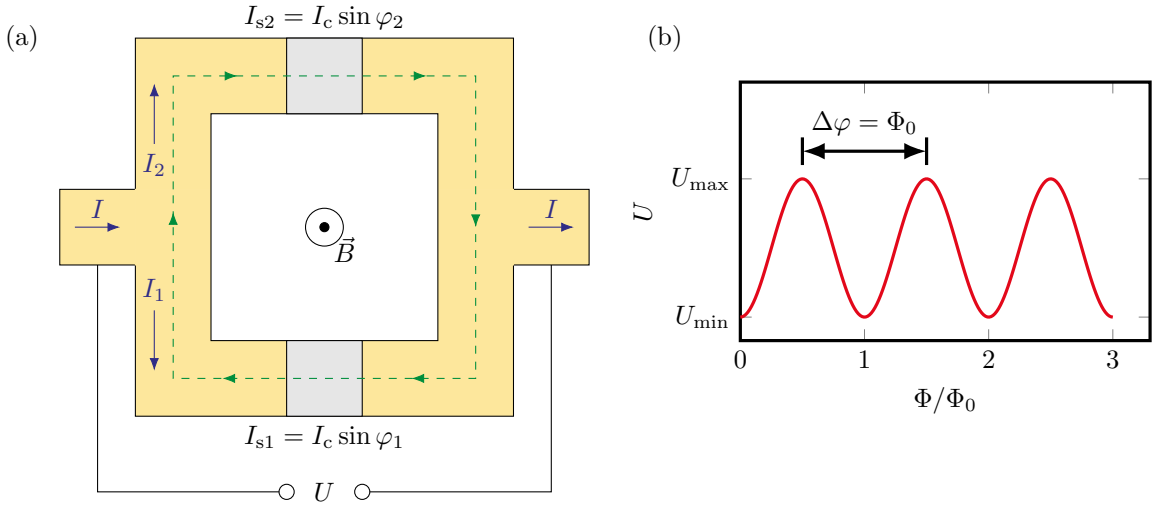

Fig. 2.18: (a) Illustration of a DC SQUID sensor. Two Josephson contacts (gray) are installed in a superconducting ring (yellow). A current I is introduced into the SQUID, which is equally divided into currents I_1 and I_2 in both parts of the SQUID. The applied external magnetic field $\vec{B}$ causes a phase shift at both Josephson contacts. The integration path introduced in chapter 2.9.2 is plotted here in green. (b) The period of the flux-voltage characteristic (shown in red) corresponds exactly to a magnetic flux quantum Φ_0. Adapted from [31,99,110].

2.9.3 Josephson effect

The Josephson effect describes the phenomenon that a superconducting state is a coherent many-body state. This can be described with the help of a macroscopic wave function. In the case of a weak coupling of two superconductors, the wave functions overlap finitely, and this overlap causes the two superconductors to form molecular-like bonds (Josephson coupling energy) and therefore interference effects occur. Josephson also postulated two equations that have been known as the Josephson equations ever since. The first equation is

$$I_S = I_C \sin(\chi), \tag{2.98}$$

which describes the electric current of Cooper pairs without electrical resistance. In it, I_S is the so-called supercurrent and $\chi = \varphi_2 - \varphi_1$ describes the phase difference. Due to the present contact geometry, I_C describes the resulting critical current at which the Cooper pairs crack in the tunnel barrier. Thus, the current is composed of tunneling single electrons and portions of Cooper pairs.

The second equation is

$$\frac{\partial \chi}{\partial t} = \frac{2e}{\hbar} U = \omega_{\mathrm{J}}, \tag{2.99}$$

where U is the electric voltage. The equation states that the voltage at a tunnel contact is always accompanied by a high-frequency, supra alternating current applied between the two superconductors. The frequency ω_{J} is the so-called Josephson oscillation and is proportional to the applied voltage.

The Josephson equations have their origin in the fact that superconductivity is a macroscopic quantum phenomenon, which is described by the wave function in Eq. (2.95). A more detailed derivation of the Josephson equations can be found in literature [109].

2.9.4 SQUID sensor

The SQUID detector consists of a small, closed superconducting ring interrupted by two parallel Josephson contacts. Magnetic flux quantization states that once the superconducting loop is permeated by a magnetic flux, the magnetic flux can exist only in integer multiples of units of a magnetic flux quantum. This quantization condition is achieved by injecting a circulating superconducting so-called shielding current into the loop, which in turn causes a magnetic flux. The combination of generated and externally applied magnetic flux results in just an integer multiple of the magnetic flux quantum Φ_0. Therefore, a periodic modulation of this shielding current is obtained, whose magnetic period length corresponds exactly to a flux quantum in the loop. It should be noted that a current flow originating from the outside must be added to the generated shielding current, which has the consequence that the resistance of the loop arrangement with the two Josephson contacts also appears periodic. Due to the fact that even fractions of a modulation period can be represented in resistance measurements, this results in highest sensitivity when measuring magnetic fields.

The information for this chapter is taken from [31] and [109].

3 Investigated materials

In this work, ultrathin $CoFe_2O_4$ single layers and $Fe_3O_4/CoFe_2O_4$ bilayers were deposited by thermal co-evaporation on single crystalline MgO(001) and $SrTiO_3$(001) substrates. Furthermore, $NiCo_2O_4$ ultra thin films were deposited on single crystalline MgO(001), $MgAl_2O_4$(001) and $SrTiO_3$(001) substrates. Therefore, the following chapter presents the properties of the investigated materials (Fe_3O_4, $CoFe_2O_4$ and $NiCo_2O_4$) on the respective substrates (MgO, $MgAl_2O_4$ and $SrTiO_3$).

3.1 Substrate material

The following subsection introduces the substrates used in this work. These are MgO, $SrTiO_3$ and $MgAl_2O_4$.

3.1.1 Magnesium oxide - MgO

Magnesium oxide (MgO) consists of oxygen $\left(O^{2-}\right)$ and magnesium ions $\left(Mg^{2+}\right)$ in a ratio of 1:1. It crystallizes in a rock salt structure with a bulk lattice constant of $a_{MgO} = 4.2117\,\text{Å}$ at room temperature [111]. The schematic structure of the bulk and surface unit cell is shown in Figure 3.1. Both types of ions each form a face-centered cubic crystal lattice, each shifted from the other by half of a unit cell. The square surface unit cell of MgO has a lattice constant of $a_S = a_{MgO}/\sqrt{2} = 2.9112\,\text{Å}$. Compared to the surface unit cell, the volume unit cell is rotated by an angle of 45°. Magnesium oxide shows diamagnetic behavior and exhibits a band gap of $\sim 7.8\,\text{eV}$ [112].

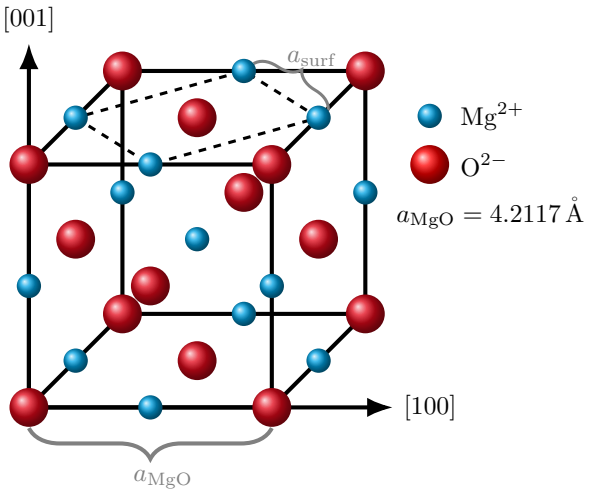

Fig. 3.1: Schematic illustration of the unit cell of the rock salt type crystal MgO with the bulk lattice constant a_{MgO}. It consists of two face-centered cubic sublattices occupied by either O^{2-} anions (red) or Mg^{2+} cations (blue). The surface unit cell of MgO, with lattice constant a_{surf}, is rotated 45° compared to the bulk unit cell.

3.1.2 Strontium titanate - $SrTiO_3$

At room temperature, strontium titanate ($SrTiO_3$, short: STO) crystallizes in a cubic perovskite structure with a bulk lattice constant of $a_{STO} = 3.905\,\text{Å}$ [113]. In the center of the cube is a Ti^{4+}-

ion surrounded by 6 O^{2-}-ions located on the faces of the cube each. The structure is consummate with Sr ions located on the corners of the cube (cf. Fig. 3.2). An interesting feature of the structure of the strontium titanate is that TiO_2- or SrO-layers alternate along the [001]-direction and, thus, the surface can be either TiO_2- or SrO-terminated. To reduce charging effects, it is possible to dope STO substrates with Nb, which makes the substrates conductive. In this work, the $SrTiO_3$ substrates are doped with 0.05 wt% Nb, making the substrates n-type conductive. In the undoped state, strontium titanate is an insulator with a band gap of 3.2 eV.

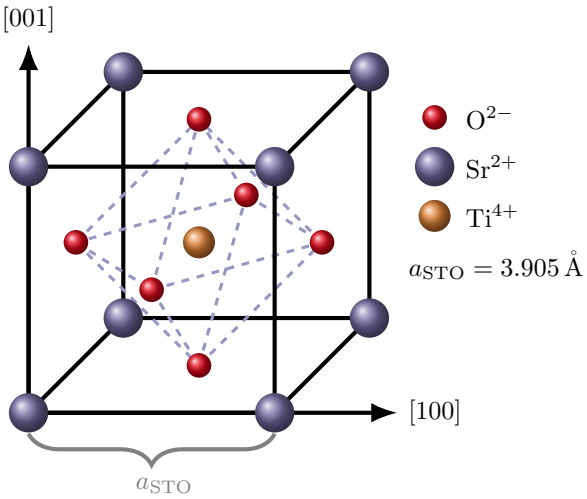

Fig. 3.2: Illustration of the cubic perovskite unit cell of $SrTiO_3$ with the bulk lattice constant a_{STO}. Six O^{2-} anions (red) form an octahedron with a Ti^{4+} cation (orange) in the center. The Sr^{2+} cations (purple) form the edges of the cube faces, each with an O^{2-} anion in the center. The $SrTiO_3(001)$ surface can be either SrO- or TiO_2-terminated, with each layer half a lattice constant apart in the [001] direction.

3.1.3 Magnesium aluminate - $MgAl_2O_4$

Magnesium aluminate ($MgAl_2O_4$, short: MAO) crystallizes in the normal spinel structure (cf. Fig. 3.3) with a bulk lattice constant of $a_{MAO} = 8.083$ Å [114]. The general structure of a spinel has the form AB_2O_4, where O^{2-} anions build a fcc sublattice with 1/8 of the tetrahedral sites occupied with Mg^{2+}-cations and half of the octahedral sites occupied with Al^{3+}-cations. $MgAl_2O_4$ is an isolator with a band gap of 5.2 eV [115].

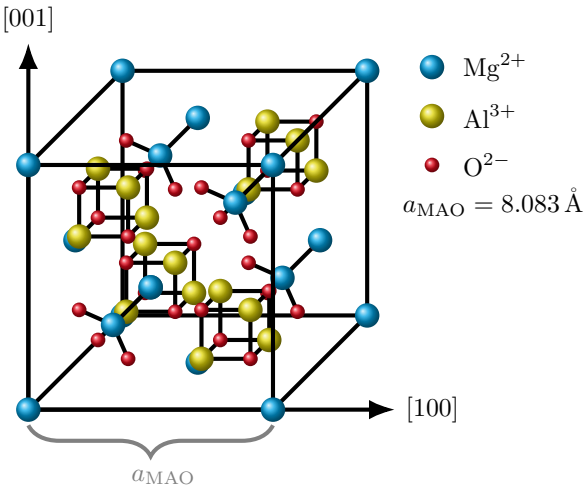

Fig. 3.3: Schematic sketch of the bulk spinel unit cell of $MgAl_2O_4$. O^{2-} anions form a fcc sublattice with Mg^{2+} cations on the tetrahedral and Al^{3+} cations on the octahedral sites.

3.2 Film material

In the following chapter, the film materials used in this thesis are explained in more detail. Only the spinels Fe_3O_4, $CoFe_2O_4$ and $NiCo_2O_4$ were used.

3.2.1 Magnetite - Fe_3O_4

Magnetite (iron(II,III) oxide) is a compound of oxygen and iron ions with the stoichiometry Fe_3O_4 (cf. Fig. 3.4(a)). It is the thermodynamically most stable iron oxide compound, which is the only one to contain both divalent and trivalent iron ions. Magnetite ideally crystallizes in an inverse spinel structure, with a lattice constant of $a_{Fe_3O_4} = 8.3963\,\text{Å}$ [116] although proportions of normal spinel were also observed. A general valid cationic order of

$$\left[Fe^{2+}_{1-\gamma}Fe^{3+}_{\gamma}\right]_T \left[Fe^{2+}_{\gamma}Fe^{3+}_{2-\gamma}\right]_O O^{2-}_4 \tag{3.1}$$

can be found, where γ describes the degree of inversion. $\gamma = 0$ denotes the normal spinel, whereas $\gamma = 1$ corresponds to the inverse spinel. The first bracket describes the occupancy of the tetrahedral sites and the second bracket therefore represents the octahedral occupancy. The tetrahedral sites (A) are occupied with Fe^{3+}-ions and the octahedral sites (B) are evenly occupied with Fe^{3+}- and Fe^{2+}-ions. Due to the antiferromagnetic coupling of the antiparallel spin moments of Fe^{3+}-ions on the tetrahedral and octahedral sites, there is a magnetic moment of $4\,\mu_B$/f.u. determined solely by the Fe^{2+} ions on the octahedral sites [47]. The magnetic order can be described as ferrimagnetic with a Curie temperature of 858 K [117]. The surface unit cell of the (001)-surface is rotated 45° with respect to the volume unit cell.

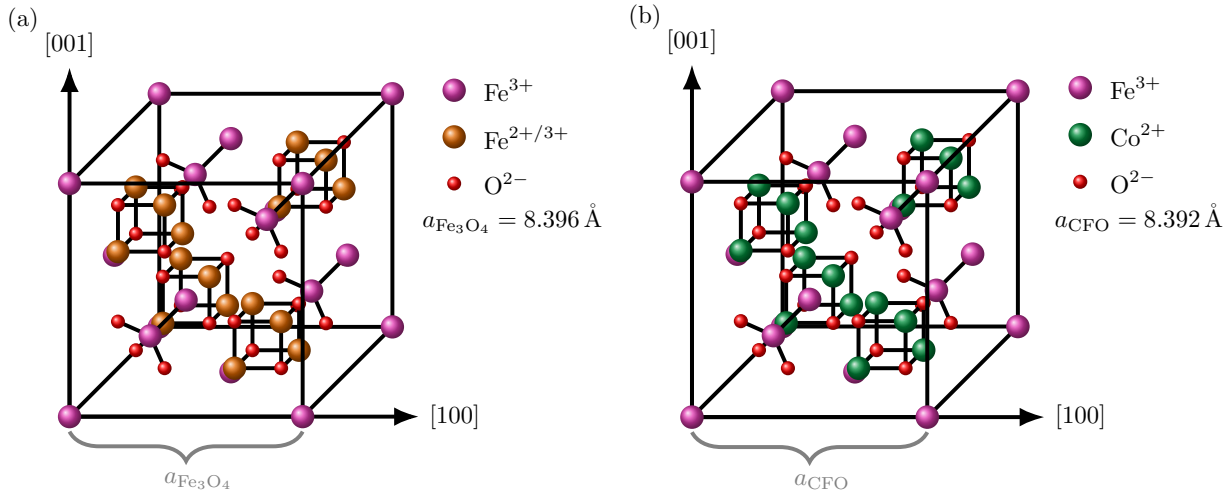

Fig. 3.4: Illustration of the bulk unit cell of (a) Fe_3O_4 and (b) $CoFe_2O_4$, each of which has an inverse spinel structure. This structure is typical of transition metal ferrites. In magnetite, the Fe^{3+} cations are equally distributed on tetrahedral and octahedral sites, whereas the Fe^{2+} cations are found only on the octahedral sites. In the case of $CoFe_2O_4$, the Fe^{2+} cations are replaced by Co^{2+}. The lattice constants are $a_{Fe_3O_4}$ and a_{CFO}.

3.2.2 Cobalt ferrite - $CoFe_2O_4$

Similar to magnetite, cobalt ferrite (CFO) crystallizes in the inverse spinel structure with a bulk lattice constant of $a_{CFO} = 8.392\,\text{Å}$ [118]. The fcc sublattice is formed by 32 O_2 ions, similar to

magnetite, whose tetrahedral sites are occupied by Fe^{3+}-ions, whereas the octahedral sites are occupied by Fe^{3+}- and Co^{2+}-ions. The occupation occurs thereby randomly. The cationic order can be described as

$$\left[Co^{2+}_{1-\gamma}Fe^{3+}_{\gamma}\right]_{T}\left[Co^{2+}_{\gamma}Fe^{3+}_{2-\gamma}\right]_{O}O^{2-}_{4}. \tag{3.2}$$

Cobalt ferrite is ferrimagnetic with a Curie temperature of 793 K [24]. Due to the antiferromagnetic coupling between the Fe^{3+}-ions on the octahedral sites and the tetrahedral sites, this leads to net saturation magnetization of $3\,\mu_B$/f.u., solely determined by the Co^{2+}-ions on the octahedral sites. The surface unit cell of the (001)-surface is rotated 45° with respect to the volume unit cell. A schematic illustration is shown in Fig. 3.4(b).

3.2.3 Nickel cobaltite - $NiCo_2O_4$

Usually $NiCo_2O_4$ crystallizes in the inverse spinel structure. Structural, magnetic and electrical properties depend mainly on stoichiometry and synthesis method [119]. In literature, lattice constants ranging from 8.11 Å to 8.185 Å [120–122] are observed. For magnetic ordering, metallic ferromagnets with transition temperatures in the range of 300 K to 400 K [121,122], as well as nonmagnetic insulators can be found [122, 123]. The ferrimagnetic Curie-temperature is 673 K [124]. The general cationic distribution can be expressed via $\left[Co^{2+}_{\gamma}Co^{3+}_{1-\gamma}\right]_{T}\left[Co^{3+}Ni^{2+}_{1-\gamma}Ni^{3+}_{\gamma}\right]_{O}O^{2-}_{4}$, with a net magnetization of $2\,\mu_B$/f.u.. This is independent of γ, assuming that the tetrahedrally coordinated cations are in high spin states and the octahedrally coordinated cations are in low spin states [122]. In the literature, metallic ferrimagnetic NCO films are usually observed with a mixed-valent structure, whereas for $\gamma \approx 0$ the structure tends to result in nonmagnetic insulators [122, 125, 126]. A schematic sketch of the bulk unit cell of $NiCo_2O_4$ is shown in Fig. 3.5.

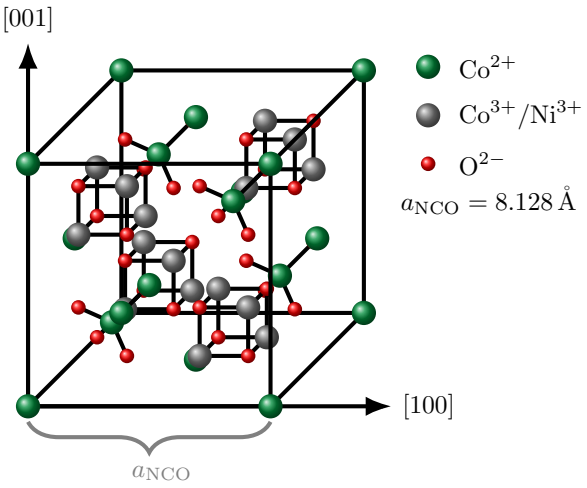

Fig. 3.5: Schematic sketch of the ideal bulk spinel unit cell of $NiCo_2O_4$. Co^{2+} cations are located on the tetrahedral and Co^{2+}/Ni^{3+} cations on the octahedral sites.

3.2.4 Antiphase boundaries in ferrites

If one part of the crystal is shifted by a translation with respect to the other part of the crystal and the translation is only a fraction of the lattice constant, the crystal is called antiphase domains. Between two adjacent antiphase domains so-called antiphase boundaries (APB) are formed. One possible reason for the presence, or the formation of antiphase domains (and antiphase boundaries) is due to the growth processes. The ordering of films can occur at arbitrary locations of the disordered lattice or nucleation centers of the substrate. Thus, the distance between two domains

is smaller than the original size of the unit cell. Antiphase boundaries are very common in inverse spinel ferrites, such as Fe_3O_4, CFO, or even NCO if grown on MgO or $SrTiO_3$ substrates, since the film lattice constant is approximately twice the substrate lattice constant [127–132]. Antiphase boundaries can affect the properties from the films in many ways. For example, influences on electrical conductivity [130,133] or magnetic properties [127–129,134–136] have been observed. The latter are manifested, for example, in the fact that either saturation magnetizations are significantly lower than for bulk structures [137] or saturation magnetization is reached only at significantly higher magnetic fields [127, 134]. With respect to structural properties, it has been reported that APBs can take the role of additional strain components in film growth and thus have an influence on the relaxation of films [138, 139].

4 Experimental setups

In the following, the different experimental setups used for the characterization of the films are described. In addition, a description of the preparation of samples and an introduction to the generation of synchrotron radiation follow. First, the in situ methods LEED and XPS are outlined, followed by a description of the ex situ methods. These are XRD, XRR, HAXPES, XAS and XMCD, all of which use synchrotron radiation. Finally, the measurement method SQUID is described, which is performed ex situ, but works independently of synchrotron radiation.

4.1 Sample preparation

All samples were prepared at the University of Osnabrück in a multi-chamber UHV system, and characterized using in situ measurement methods. The chamber system consists of a load-lock, into which substrates or prepared samples can be loaded or unloaded, and several UHV chambers connected by transfer paths. This allows samples to be moved around the system without breaking the vacuum. In the preparation chamber, substrates can be cleaned and films can be deposited. A rotary sample stage and an oxygen inlet are available for this purpose. A plasma source is also available for the generation of highly reactive oxygen. For sample preparation and substrate cleaning, high temperatures are required (here 400 °C), which is provided by a heating element on the sample holder. The temperature is monitored through a thermocouple. The base pressure in this chamber is approximately 1×10^{-9} mbar. A much lower pressure is achieved in the analysis chamber where the LEED and XPS systems are located. Here, the base pressure is about 1×10^{-10} mbar. The advantage of such a low pressure is that the mean free path length of the electrons to be detected increases. The measurement methods are described in more detail in section 4.2.1 and 4.2.2. The samples in this work were prepared using reactive molecular beam epitaxy (RMBE) and oxygen plasma assisted molecular beam epitaxy (OPA-MBE). In the first case, the fabrication process involves molecular oxygen, whereas in the second case, a plasma source is used to provide oxygen plasma. Using SPECS evaporators (cf. Fig. 4.1), the thermal evaporation process is used to produce thin films. For this purpose, pure metal rods, consisting of Co, Ni or Fe, are connected to high

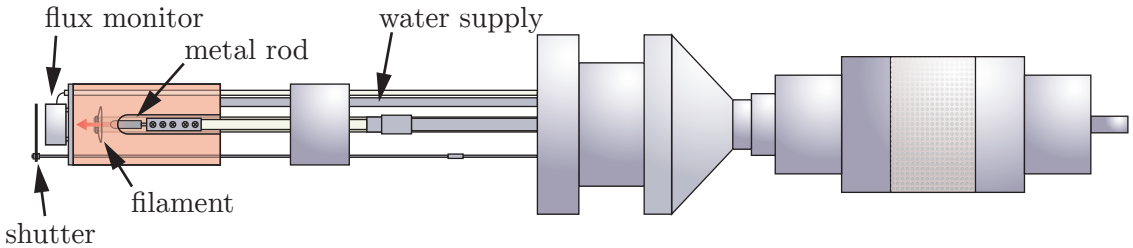

Fig. 4.1: Schematic sketch of an evaporator used in this work. Electrons are generated via a filament and accelerated to the metal rod by means of a high voltage. This causes the metal rod to heat up until the sublimation temperature is reached and the atoms to escape from the effusion cell. The amount of evaporated material can be determined via the flux monitor, and a shutter allows the precise setting of the evaporation time. Water cooling is used to prevent overheating. Taken from [110].

voltage and electrons are accelerated onto this rod with the help of a filament. When the sublimation temperature is reached, atoms/molecules are emitted and leave the evaporator in the form of a beam, which finally condenses on the surface of the samples due to temperature difference. A shutter in front of the evaporator can be used to precisely control the deposition time. Furthermore, a flux monitor is used to determine the deposition rate. This is only possible if a calibration sample is prepared beforehand and characterized by XRR. For CFO and NCO films, it is necessary to operate two evaporators simultaneously. This is called co-evaporation. The stoichiometry of the layers is determined by the ratio of the deposition rates relative to each other. The substrates used, MgO(001), MAO(001) and 0.05 wt% Nb-doped STO(001), are purchased from CrysTec GmbH or SurfaceNet GmbH. The surface orientation tolerance is specified by the manufacturers as $< 0.1°$. To remove impurities (such as carbon) from the substrates, they are cleaned for 1 h at 400 °C and an oxygen partial pressure of 1×10^{-4} mbar in the preparation chamber. The surface purity and crystallinity are then checked by LEED and XPS. After ensuring that only the desired elements are on the sample and that the diffraction pattern exhibits sharp diffraction reflexes with low background intensity, the substrates are returned to the preparation chamber, where film fabrication finally takes place. For this, the substrate is brought to a temperature of 250 °C and an oxygen partial pressure of 5×10^{-6} mbar is set. These parameters were found to be the best evaporation conditions for all films prepared here. For the NCO films, in addition to molecular oxygen, a series was prepared with oxygen plasma. As with the substrates, the stoichiometry and surface structure of the prepared films are analyzed in the analysis chamber using LEED and XPS.

4.2 Surface characterization

The following subsections describe the fundamentals of experimental setups that do not involve the application of synchrotron based X-rays. It thus describes the measurement methods that were carried out in situ, after sample preparation, at the University of Osnabrück.

4.2.1 LEED - Experimental setup

The schematic setup of the LEED measurement system is shown in figure 4.2. A 4-grid LEED optical system from SPECS (ErLEED 150) is used here for the low-energy electron diffraction measurements. The measurement system consists of two basic elements: First, the electron gun (cathode) to generate electron beam and second, the fluorescent screen to display the diffraction pattern. To generate the electrons, an accelerating voltage is applied to the cathode, producing a beam of low-energy electrons. This beam is focused by the combination of the Wehnelt cylinder and lens system and then hits the sample surface. There, the beam is diffracted and subsequently the diffracted beams pass through the multigrid system to the fluorescent screen, where the diffraction pattern is then finally visible. The grid systems consists of four grids, of which the first and fourth each are set to ground potential. Due to the fact that the grids are at ground potential together with the sample, a field-free space is created between the grid and the sample, which in turn causes the electrons to move in a straight line towards the screen. A negative potential is applied between the second and third grid so that inelastically scattered electrons do not hit the screen and only elastically scattered electrons reach the fluorescent screen. Typically, the fluorescent screen runs at a high voltage of 6 kV and the cathode at about 2.25 A. A CCD camera is used for visualization and data acquisition. Due to the fact that the camera is located behind the electron gun, the electron gun is always visible on the resulting images. It is therefore not possible to detect the beam diffracted perpendicular to the surface ((00) diffraction reflex).

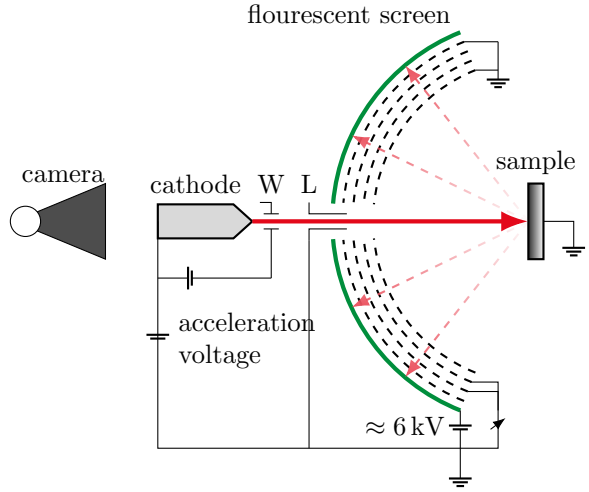

Fig. 4.2: Schematic structure of the LEED system. By applying an accelerating voltage to the cathode, an electron beam is generated which passes through the combination of Wehnelt cylinder (W) and lens system (L) and is focused before it hits the sample. Elastic and inelastic diffraction occurs at the surface of the sample. The grid arrangement is designed to allow the diffracted electrons to move in a straight line to the screen and to detect only elastically scattered electrons. On a fluorescent screen, the diffraction pattern can be seen, which is recorded using a camera. Leaned on [33, 140, 141].

4.2.2 XPS - Experimental setup

For the in situ characterization of the samples, an XPS measurement system from SPECS is used. A schematic representation is depicted in figure 4.3.

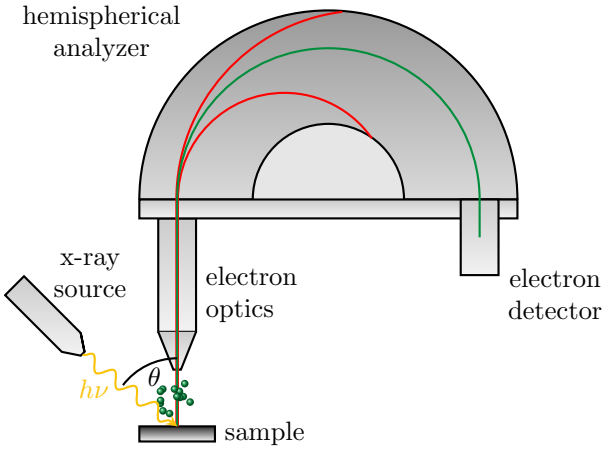

Fig. 4.3: Schematic sketch of the XPS setup used. The main components include an X-ray source, electron optics, a hemispherical analyzer and an electron detector. The sample is irradiated with X-rays of an energy $h\nu$, causing photoelectrons to be emitted, which in turn enter the electron optics, where they are subsequently focused and decelerated at a certain energy (E_p). Afterwards, the photoelectrons emerging from the sample enter the hemispherical analyzer, where an electrostatic field imposes a circular path on them. Only those electrons whose kinetic energy E_kin matches the pass energy E_p of the analyzer enter the detector.

The main components of the measurement system are on the one hand the X-ray source and on the other hand the detection system consisting of a hemispherical analyzer (Phoibos HSA 150, SPECS), a detector and electron optics.

Two different anode materials are available as X-ray source. Here, either a magnesium (Mg K_α, $h\nu = 1253.6\,\mathrm{eV}$) or an aluminum anode (Al K_α, $h\nu = 1486.6\,\mathrm{eV}$) is used. A fixed angle of 54.7° is set between the X-ray source and the entrance of the electron optics (cf. Fig. 4.3). The X-ray beam hits the sample and emits photoelectrons, which in turn leave the sample in many different directions and energies, so that only the photoelectrons incident at the above angle also enter the entrance of the hemisphere analyzer. In front of the entrance of the hemisphere analyzer, the electron optics are installed. These consist of a number of electronic lenses and apertures, ensuring that the emitted photoelectrons are collimated, focused and decelerated before they enter the analyzer. Inside the hemisphere analyzer, the electrons travel along a curved trajectory determined by the pass energy. Only electrons moving through the analyzer with this pass energy reach the detector and can be detected. The spectrum is recorded by keeping the field in the hemisphere analyzer constant and varying the kinetic energy of the photoelectrons through the electron optics.

Thus, all the different kinetic energies are decelerated to those kinetic energies that are fixed in the range of the pass energy. This measurement method is called fixed analyzer transmission (FAT) mode. A positive aspect here is that the same spectral resolution of the XP spectrum is ensured for all measurements. The absolute intensity of the spectra can be increased via the pass energy, which is associated with a more optimized signal-to-noise ratio. However, this has the consequence that the energy resolution decreases.

4.3 Experimental setups at synchrotron radiation facilities

When experiments on ultrathin films are to be taken to the next level, the use of synchrotron radiation for experiments on these films is indispensable. In contrast to laboratory-based experiments (see chap. 4.2), the use of synchrotron radiation offers a variety of advantageous properties, such as a small beam size, high beam intensity, low divergence, high brilliance, and highly variable setting of beam energies. Thus, it is possible to resolve even the smallest measurement signals well and also to achieve high excitation energies. For this reason, a large number of the experiments carried out in this thesis were performed at synchrotron radiation sources. At the Deutsches Elektronen Synchrotron (DESY) in Hamburg (Germany), the XRR and XRD measurements were performed at beamline P08, and the HAXPES experiments at beamlines P09/P22. The XAS, or XMCD experiments were performed at beamline 4.0.2 of the Advanced Light Source (ALS) at Lawrence Berkeley National Laboratory in Berkeley (USA).

4.3.1 Generation of synchrotron radiation

The basic principle to generate synchrotron radiation is the fact that charged particles emit electromagnetic radiation when they are accelerated. If the velocity of the particles is much smaller than the speed of light (non-relativistic), the dipole emission radiation has the shape of a toroid. The center of the toroid points in the direction of acceleration (see Fig. 4.4). However, since the velocities in synchrotron radiation sources are much higher, being in the range of the speed of light, effects like Doppler shift and relativistic effects have to be taken into account. This changes the shape of the emission radiation into a cone, as shown in figure 4.4. The center of the radiation then points tangentially to the direction of particle motion. In the generation of synchrotron ra-

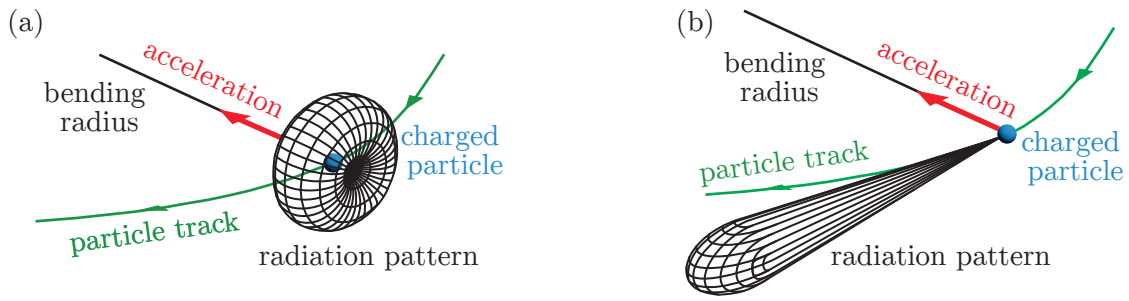

Fig. 4.4: Schematic sketch of an evaporator used in this work. Electrons are generated via a filament and accelerated to the metal rod by means of a high voltage. This causes the metal rod to heat up and therefore atoms to escape from the effusion cell. The amount of evaporated material can be determined via the flux monitor and a shutter allows the precise setting of the evaporation time. Due to the resulting temperatures, water cooling is used to prevent overheating. Adapted from [142, 143].

diation, the particles, mostly electrons or positrons, are first accelerated by a linear accelerator to

nearly the speed of light and then injected into a so-called accelerator ring. Here, the particles are further accelerated with the help of alternating electric fields at high frequencies before they are subsequently brought into the storage ring. There, they move at a constant speed along a (nearly) circular path and finally emit the highly brilliant synchrotron radiation. A closer look reveals that the circular path is a polygon, i.e. it consists of straight lines and curves. So-called bending magnets force the particles in the curves onto their circular paths. According to the Lorentz force, the electromagnetic radiation is emitted there tangentially to the direction of acceleration (cf. Fig. 4.4). The resulting spectrum of radiation ranges from microwaves to hard X-rays and depends on both the energy of the particles and the bending radius, i.e. in principle the geometry of the storage ring. In the straight sections of the storage ring, there is a periodic arrangement of dipole magnets with alternating polarity, which causes the particles to follow an wavelike path (cf. Fig. 4.5). This arrangement is called an insertion device and serves to increase the brilliance or intensity

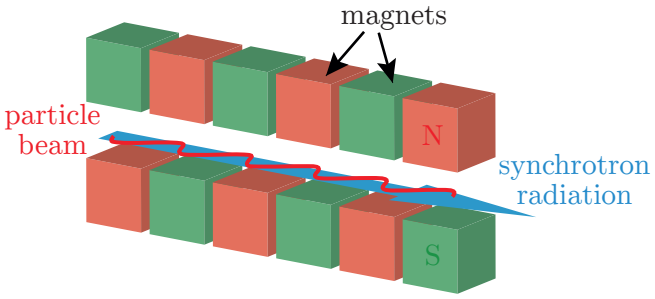

Fig. 4.5: Example of a wiggler/undulator. Electromagnets with alternating polarity force the particles onto an wavelike path. By superimposing the radiation on each pair of magnets, the total radiation also increases. Adapted from [143].

of the emitted beam. A distinction is made here between so-called wigglers and undulators. These differ basically only in the deflection of the particles. In the case of a wiggler, the deviation of the particles is relatively high, with the result that the radiation is superimposed incoherently. The result is a continuous emission spectrum, which is similar to the spectrum of a bending magnet, but with a much higher intensity. Compared to the bending magnet, which is limited by the storage ring geometry as described above, wigglers have much more freedom and can thus be adapted to experimental requirements. In contrast to the wiggler, a different phenomenon is observed with an undulator. Here only small amplitudes are generated and this in turn leads to interference of the radiation cones. The intensity is much larger and sharper than with the wiggler, where the intensity distribution is relatively broad. By changing the spacing between the rows of magnets, it is also possible to adjust the wavelength of the beam. When the beam leaves the storage ring, it is routed into the so-called optics hutch before it reaches the so-called end station, where the experiments are performed. The optics hutch houses the beamline optics consisting of monochromators, focusing lenses and mirrors as well as windows and slits. These serve to optimize the beam so that it has optimum conditions for the respective experiments.

4.3.2 HAXPES - Experimental setup

A schematic sketch of the setup is shown in Fig. 4.6. In the endstation of the beamline a UHV chamber, a multi-axis manipulator for the alignment of the samples and a high resolution photoelectron detector are located. After passing the electron detection system, the emitted photoelectrons move through a concentric hemispherical analyzer until they reach the detector. Using the manipulator, it is also possible to align the sample at different angles with respect to the X-ray beam and thus varying probing depths are achieved. Compared to laboratory-based X-ray sources, for HAXPES

experimenets in this work, photon energies of 4600 eV, 5945 eV, and 6000 eV were used, which in turn results in more bulk-sensitive measurements because the inelastic mean free path (IMFP) of the photoelectrons is larger. For the information depth D_{I}^{95} from which 95 % of the photoelectrons are detected, the following formula can be used:

$$D_{\mathrm{I}}^{95} = -\lambda \cos(\varphi) \ln\left(1 - \frac{95}{100}\right) \approx 3\lambda \cos(\varphi). \tag{4.1}$$

Therein, λ corresponds to the IMFP and φ corresponds to the off-normal emission angle (detection angle). An angle of 0° gives a maximum depth of information. This is approximately 22 nm for the orbitals Fe 2*p*, Co 2*p*, and Ni 2*p* considered here ($E = 6$ keV). At an angle of 60°, on the other hand, the information depth decreases to about 10 nm, which corresponds to an increasing surface-sensitivity. Indeed, if the detection angle is increased, more and more information from the layers close to the surface is incorporated, such that the surface sensitivity increases. The reason for this is that the electrons released from too deep layers have to overcome too long a path in the sample towards the detector and thus, due to the limited IMFP, cannot contribute to the signal of the spectrum.

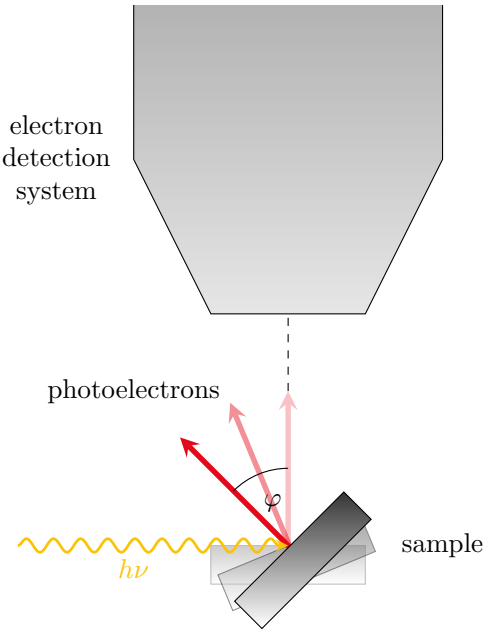

Fig. 4.6: Depicted is the (AR)-HAXPES measuring method. Only the cutout around the sample holder is shown. The sample is irradiated with X-rays of energy $h\nu$. As the sample holder can be tilted at an angle φ with respect to the entrance of the electron detection system, different penetration depths can be realized. The higher the φ, the more information can be obtained from the near-surface layers of the sample. Adapted from [110].

4.3.3 (GI)XRD and XRR - Experimental setup

Laboratory based XRR measurements were performed at the diffractometer of the University of Bielefeld, Germany. A lab based X-ray diffractometer (Phillips X'Pert Pro) with a photon energy (Cu K_α) of 8048 eV was used for this purpose. Measurements were made in $\theta - 2\theta$ geometry. The XRD and the synchrotron based XRR measurements of this work were performed at the beamline P08 of PETRA III at DESY in Hamburg, Germany. A six-circle diffractometer is located in the beamline endstation, allowing the samples and detector to be aligned relative to the incident X-ray beam. The photon energies used here are 15 keV, and 18 keV, respectively. A sketch of the setup is shown in Fig. 4.7. The diffractometer is of the 4S+2D type, which means that four degrees of freedom are available for the sample (S) and two for the diffractometer (D). An Euler cradle can be used to continuously adjust the surface orientation of the sample between vertical or horizontal, the latter being chosen in this work. The azimuth and polar angles are denoted

by φ, and ω, respectively. The detector is moved via the δ and γ angles (see Fig. 4.7). Three measurement methods were used for this work: specular x-ray diffraction (XRD), x-ray reflectivity (XRR), and grazing incidence x-ray diffraction (GIXRD). For the first two measurement methods, the angles $\omega = \theta$ and $\delta = 2\theta$ are set, which is why this is called $\theta - 2\theta$ geometry. The other angles $(\alpha, \gamma, \varphi)$ are set to zero, which makes the lateral components of the scattering vector also zero. In addition, the wave vectors of the incident, or outgoing, beam are in a plane orthogonal to the surface of the sample. With this method, measurements can be made along the $(00L)$ CTR. With grazing incidence X-ray diffraction, additional CTRs can be measured in addition to the $(00L)$ CTR. Furthermore, it is possible to perform so-called 'in-plane' measurements at L close to 0. To achieve grazing incidence, the angle of incidence ω is set to a fixed value, which is slightly above the critical angle of the material under investigation. In the present case $\alpha < 0.5°$. To set the diffraction condition this time, unlike the previously mentioned measurement methods, the angles α, γ and φ are adjusted. This measurement method is very sensitive to the surface, because only information from the regions close to the surface contribute to the signal due to the small angle.

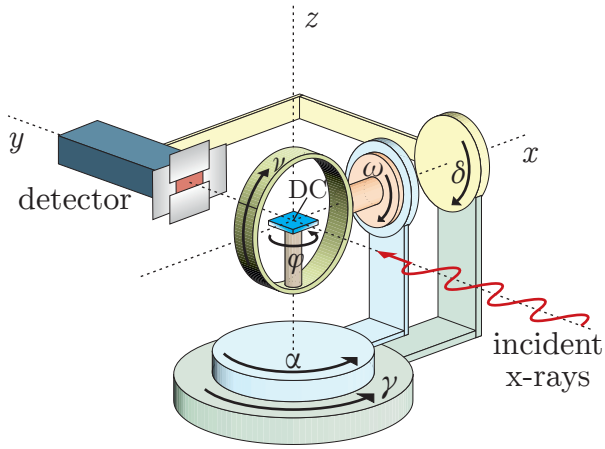

Fig. 4.7: Schematic sketch of the diffractometer used for the (GI)XRD and XRR measurements at beamline P08. The type of the diffractometer is a (4S+2D), i.e. two degrees of freedom for the orientation of the sample and four degrees of freedom for the orientation of the diffractometer. The sample holder is mounted on a Euler cradle. In the center of the diffractometer (DC) all rotation axes intersect. Taken from [40].

4.3.4 XAS/XMCD

The XAS and XMCD measurements, respectively, were performed at beamline 4.0.2 of ALS, Berkeley, USA. A superconducting vector magnet is placed in a UHV chamber, which can be used to provide a magnetic field of up to 4 T. The samples are attached to a rotatable sample holder (made of copper) using silver conductive paste. This ensures that the emitted electrons can drain off via the sample holder and thus the resulting measurement signal can be detected in TEY mode. An angle of 30° relative to the sample surface is set between the sample holder and the detector. This guarantees that the X-ray beam hits the samples without any obstacles. The incident X-ray beam is circularly polarized (left and right)for measurement. The same dichroic signal can be obtained if an absorption spectrum is measured with different magnetic fields, here ±4 T. For the analysis of the measurements, charge-transfer multiplet calculations and sum rules were performed using the software FMD [76]. This program is based on the Cowan code [84], and offers a considerably comfortable work due to the graphical user interface. To perform CTM calculations of the various cations, the program uses various multiplet parameters characteristic of the cation species (charge-transfer energies of the ground and final states, crystal field splitting (10Dq), and exchange splitting). Finally, the simulated data of each absorption edge are weighted and summed and then compared with the experimental measurements.

4.4 SQUID magnetometry

The magnetic properties of the prepared samples were analyzed using a SQUID magnetometer from Quantum Design (Model MPMS3). A schematic sketch is shown in Fig. 4.8. Inside the device is a superconducting magnet that can realize magnetic fields up to 7 T. It is important that the magnet is cooled, which is achieved via a cryogenic dewar filled with liquid helium. Temperatures of 1.8 K to 400 K can be achieved via a sample heater in combination with the cooling of the liquid helium. The sample, attached to a glass rod, is inserted into the measurement setup via a cryogenic insert (measuring tube). Inside the tube, at sample level, is a SQUID detection circuit, which in

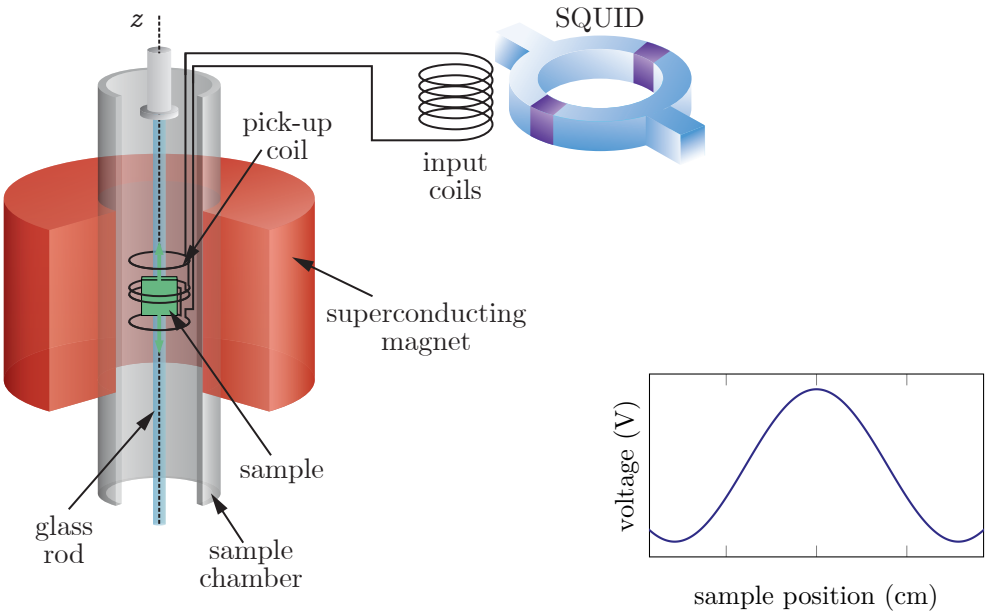

Fig. 4.8: Sketch of the main components of the SQUID system. The sample is attached to a glass rod which moves vertically up and down in a magnetic field inside the sample chamber. This causes a current to be induced in the superconducting flux transformer, which couples this current to the DC SQUID. The superconducting magnet delivers magnetic fields of up to 7 T. Temperatures from 1.8 K to 400 K can be realized using liquid helium and a heating element. The vertical sample movement changes the voltage of the SQUID as shown in the smaller graph. Taken from [40] and modified.

turn consists of a DC (direct current) SQUID and superconducting detection coils. A DC SQUID consists of two identical parallel connected Josephson junctions. The detection coils are themselves inductively coupled to the SQUID via a series of matching superconducting input coils. This is referred to as a flux transformer. As the magnetized sample is moved up and down the tube, the magnetic flux measured by the detection coils changes. Here, the sensitivity of the SQUID is approximately $\leq 1 \times 10^{-8}$ emu. To ensure this, the measurement signal must be shielded from any outside interference, which is guaranteed by a special winding of the coils. For additional protection, the DC SQUID is also magnetically shielded. After installation of the sample, an adjustment is made for ideal centering between the detection coils. This significantly maximizes the measurement signal. As described above, for this measurement principle it is important that the sample is magnetized, here by a superconducting magnet, and moves up and down the tube at a constant speed, causing the flux to change. According to the law of induction, a current is thus induced in the detection coils which is proportional to the magnetic flux change and is then passed on to the input coils. There, a magnetic flux is created, which generates an output voltage in the superconducting loop of the SQUID. Therefore, a voltage response is generated over the entire range

of motion of the sample, through which the magnetic moment of the sample can be determined. In order to obtain higher accuracy and save time, several small partial measurements are carried out for different field strengths, for example, and these are then averaged. This sometimes results in long measurement times per hysteresis and temperature. In the SQUID, the magnetic moment of the entire sample is always measured. This also includes unwanted components of the substrate and the sample holder. These have to be subtracted from the total signal to finally obtain the magnetic moment of the pure ferro/ferrimagnetic layer. For the substrates and the sample holder used here, a correction is easily performed, since these diamagnetic materials cause a linear background in the signal. The practical procedure is as follows: straight lines are assumed in the linear parts of the hystereses at high fields, ideally at magnetic saturation. The slopes of these straight lines are then averaged and then subtracted from the total signal. This results in the pure magnetic moment of the corresponding layer.

Original publication: The Journal of Physical Chemistry C **117**, 42, 23327–23337 (2021)
available at http://doi.org/10.1021/acs.jpcc.1c05274

Interface Magnetization Phenomena in Epitaxial Thin $Fe_3O_4/Co_xFe_{3-x}O_4$ Bilayers

K. Ruwisch[1], J. Thien[1], T. Pohlmann[1,2], M. Hoppe[1,2], F. Bertram[2], K. Kuepper[1], and J. Wollschläger[1]

[1] *Department of Physics, Osnabrück University, Barbarastrasse 7, D-49076 Osnabrück, Germany*
[2] *DESY, Photon Science, Notkestraße 85, D-22607 Hamburg, Germany*

Abstract

In this work, we present a study about the chemical and magnetic properties of thin magnetite/cobalt ferrite bi-layers deposited on MgO(001). Two series of samples with different $Co_xFe_{3-x}O_4$ stoichiometries (x=1 and x=0.5) in combination with Fe_3O_4 layers of varying thickness were prepared by reactive molecular beam epitaxy. The quality of the respective films were controlled by means of *in situ* x-ray photelectron spectroscopy and low energy electron diffraction. Stoichiometry and electronic structure were carried out by hard x-ray photoelectron spectroscopy. To determine the cationic distribution and magnetic moments, x-ray magnetic ciruclar dichroism measurements were performed and charge transfer multiplet and sum rule calculations were applied. Here we find an enhanced interface magnetization for the bilayers. Additionally, superconducting quantum interference device measurements showed characteristic exchange-spring behavior.

Original publication: Materials **2022**, 15, 2377
available at http://doi.org/10.3390/ma15072377

Real-time Monitoring the Growth of Epitaxial $Co_xFe_{3-x}O_4$ Ultrathin Films on Nb-Doped $SrTiO_3(001)$ via Reactive Molecular Beam Epitaxy by Means of Operando HAXPES

K. Ruwisch[1], T. Pohlmann[1,2], F. Bertram[2], C. Schlüter[2], A. Gloskovskii[2], K. Kuepper[1], and J. Wollschläger[1]

[1] *Department of Physics, Osnabrück University, Barbarastrasse 7, D-49076 Osnabrück, Germany*
[2] *DESY, Photon Science, Notkestraße 85, D-22607 Hamburg, Germany*

Abstract

In this work, we present a comprehensive study on real-time monitoring the growth of epitaxial $Co_xFe_{3-x}O_4$ thin films grown on $SrTiO_3(001)$ substrates via reactive molecular beam epitaxy. The growth process was monitored during evaporation by means of time resolved operando hard X-ray photoelectron spectroscopy (HAXPES). We prepared ultrathin ferrite films using different oxygen partial pressures, showing pure metallic, light oxidic, and cobalt ferrite-like growth. Additional X-ray diffraction measurements confirm HAXPES results.

6.1 Introduction

Transition metal oxides exhibit numerous properties, such as competition of spin, charge, and orbital degrees of freedom. More specifically, a lot of ferrites show a high Curie temperature T_C and a high magnetic saturation moment. Hence, these ferrites might be excellent materials for applications in the fields of spintronics [24, 144, 145] or spincaloritronics [146]. Many of these Fe based oxides exhibit varying electronic and magnetic properties and crystallize in the inverse spinel structure. Examples include the semimetallic and ferrimagnetic Fe_3O_4, the semiconducting $\gamma - Fe_2O_3$, and the more insulating ferrimagnets $NiFe_2O_4$ and $CoFe_2O_4$ (CFO). The latter mentioned oxides, i.e., $NiFe_2O_4$ and $CoFe_2O_4$ are in particular interesting for spin-filter applications [147–150]. The aim for spin-filter applications is generating highly spin-polarized currents due to spin polarization dependent tunneling of electrons. Because the structural quality of the tunnel barrier and its interfaces significantly affects the spin filter efficiency and is important for the transmission of spin currents, ferrites must be fabricated as thin films with low defect density, which appears to be one of the major obstacles as spintronic devices with $NiFe_2O_4$ and $CoFe_2O_4$ electrodes did not prove to be very successful yet. Only for $CoFe_2O_4$ a room temperature spin filtering effect with a spin-polarization value of $-8\,\%$ was obtained up to now [149]. These shortcomings have been associated to the structural quality and the chemical properties of the ferrite ultra thin films right at the substrate interface. Antiphase boundaries (APBs) and other interface effects might lead to the formation of a magnetic dead layer, for instance [72, 149]. Besides the above mentioned effects Ti diffusion into $CoFe_2O_4$ thin films grown on $SrTiO_3(001)$ substrates has been reported [151]. In addition to the interfacial effects mentioned above, the magnetic and structural properties strongly depend on other parameters such as thin film thickness [152], or growth conditions such as growth temperature or oxygen pressure [153]. Since ferrites are known to form different morphologies,

such as rock salt and spinel structure, it is of utmost interest to study the electronic structure during growth. Hence, we obtain information on the different stages of growth in real time and therefore develop a deeper understanding of the initial stages of the thin film formation. Moreover, for spin-filters, it is crucial to fabricate stochiometric $CoFe_2O_4$. Metallic Fe and Co is not used in the application, so here we are looking for the right parameters to produce stoichiometric $CoFe_2O_4$ and observe the evolution of the film during fabrication.

In the present work we perform a real time monitoring of the epitaxial growth of thin $Co_xFe_{3-x}O_4$ films on Nb-doped $SrTiO_3$(001) substrates with varying partial oxygen pressures employing hard X-ray photoelectron spectroscopy (HAXPES). Peak positions and satellites in the spectra of photoelectron spectroscopy measurements are unique features for the oxidation state. We exploit this feature to make deductions about the chemical composition. HAXPES is a powerful tool to investigate the electronic and chemical properties not only on the surface near regions of a sample in question but also in deeper layers due to excitation energies of several keV. Hence, we are able to collect valuable information from the whole ultra thin film during the overall growth process. We demonstrate that the different partial oxygen pressures lead to the formation of different Fe and Co valence states and final compounds but also that the Fe and Co oxidation processes may continue longer than the thin film deposition process itself.

6.2 Materials and Methods

Film preparation and analysis were carried out at beamline P22 of synchrotron radiation source PETRA III at the Deutsches Elektronen Synchrotron (DESY). As an endstation, we used a custom-made ultrahigh-vacuum (UHV) chamber which is equipped with iron and cobalt evaporators and a SPECS Phoibos 150 HV hemispherical analyzer with a delay line detector and wide-angle lens. This experimental setup allows us to perform hard X-ray photoelectron spectroscopy (HAXPES) measurements while growing thin CFO films. The $CoFe_2O_4$ thin films have been prepared on Nb-doped $SrTiO_3$(001) single crystalline substrates using reactive molecular beam epitaxy (RMBE) in an UHV system at a base pressure of 10^{-8} mbar in the deposition chamber. Since Nb-doped $SrTiO_3$ is conductive this substrate is very appropriate for this experimental setup in order to reduce charging effects. The substrates used in this study (SurfaceNet GmbH) have a surface orientation tolerance less than 0.1°. Before deposition, the substrates were cleaned by annealing at 400 °C for 1 h in an oxygen atmosphere of 1×10^{-4} mbar. The RMBE deposition process is done in the following steps: before the start of the deposition, the substrate is heated by electron bombardement to a deposition temperature T_{dep} (400 °C in this work) and the UHV chamber is filled with molecular oxygen up to a partial pressure of p_{O_2} (ranging from 1×10^{-7} to 5×10^{-6} mbar in this work). In two molecular beam evaporators with closed shutter, pure cobalt and iron rods are heated to evaporation temperature by electron bombardment. In order to keep the growth rate constant, the ion flux leaving the evaporators is monitored using a fluxmeter. Once the flux has stabilized, co-deposition of the $CoFe_2O_4$ films is started by opening the shutters of both evaporators. After the intended evaporation time, the deposition is stopped by closing both evaporator shutters. Next, the sample heater is switched off, so that the substrate starts cooling down. At a substrate temperature of 100 °C, the oxygen supply is cut and the UHV chamber returns to its base pressure. During growth, the Fe 2p and Co 2p core levels were rapidly measured (2 min per scan) by HAXPES measurements at an excitation energy of $h\nu = 4600$ eV. After deposition, low-binding energy scans in the range from 0 eV to 140 eV and high resolution Fe 2p and Co 2p scans were performed in-situ.

Additionally, after film growth X-ray diffraction (XRD) experiments were performed ex-situ at beamline P08 of synchrotron radiation source PETRA III at DESY. For these measurements, a photon energy of 15 keV and a six-circle diffractometer with a two-dimensional PILATUS 100k

detector was used.

Figure 6.1a shows reference spectra of metallic Co and CoO ultra thin films prepared by molecular beam epitaxy (MBE). In addition, Figure 6.1b shows the spectra of metallic Fe, as well as the various iron oxide compounds FeO, Fe_2O_3 and Fe_3O_4. The Fe spectrum stems from a 100 nm thin film prepared by MBE. The reference spectra of the iron oxides originate from single crystals cleaved in-situ directly before XPS measurements. Depending on the chemical composition, the spectra have characteristic shapes and properties. These are, as already described, the positions of the photoelectron peaks, as well as their satellites. Based on this, it is easy to make comparisons with the spectra obtained from prepared samples.

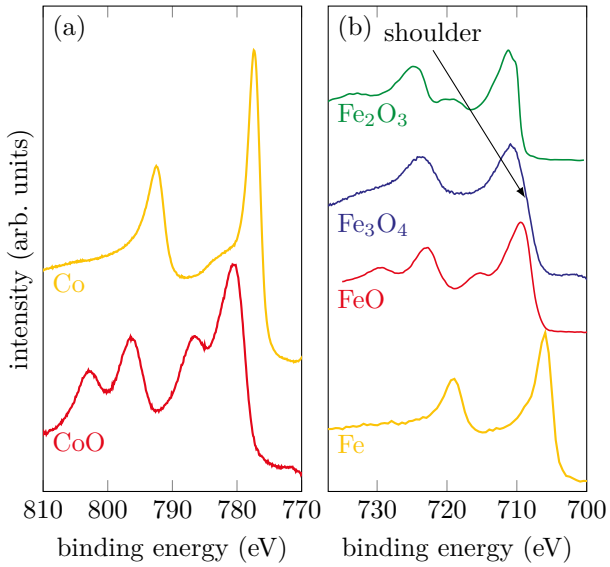

Fig. 6.1: Reference spectra of (**a**) metallic Co and CoO samples and (**b**) metallic Fe and different iron oxide compounds.

For metallic Co and Fe, it can be seen that there are no satellites and the peak shape is asymmetric. CoO, which consists only of Co^{2+} ions, has two shake-up satellites that are shifted to higher binding energies by 6.2 eV compared to the main peaks. For the iron oxides, the observation of the satellites, in addition to the different positions of the main peaks, provides information about the oxidation state. Considering FeO, which contains exclusively Fe^{2+} ions, a charge-transfer satellite can clearly be seen at still higher binding energies for both Fe 2p photoelectron peaks. If one compares this with Fe_2O_3, whose iron cations are exclusively trivalent, it can be seen that, in addition to different binding energies for the main peaks, the charge-transfer satellites are also shifted towards higher binding energies. For magnetite (Fe_3O_4), iron is present in both the Fe^{3+} and Fe^{2+} states. For this reason, the two satellites observed in the Fe_2O_3 and FeO spectra overlap and form a flat plateau between the main peaks of the Fe_3O_4 spectrum without any apparent satellite.

6.3 Results and Discussion

6.3.1 HAXPES

For this study, we prepared a series of three $Co_xFe_{3-x}O_4/SrTiO_3(001)$ samples grown under different conditions. Their oxygen partial pressures and growth rates are summarized in Table 6.1. In the following, we will separately examine them to investigate the influence of the growth parameters on the electronic structure. The spectra of all samples were calibrated to the binding energy of the O 1s peak ($E_B = 530$ eV).

Sample	p_{O_2} (mbar)	Growth Rate (pm s^{-1})	Co Content x
A	5×10^{-7}	6.4	1.18 ± 0.3
B	1×10^{-6}	5.5	1.18 ± 0.3
C	5×10^{-6}	10.5	1.07 ± 0.3

Tab. 6.1: Overview of the prepared samples with the respective oxygen partial pressure and the growth rate.

Sample A—Low Oxygen Pressure

Sample A was grown with a low oxygen partial pressure of 5×10^{-7} mbar. Figure 6.2a,b show the Co 2p and Fe 2p peaks, respectively, at selected steps during the RMBE process.

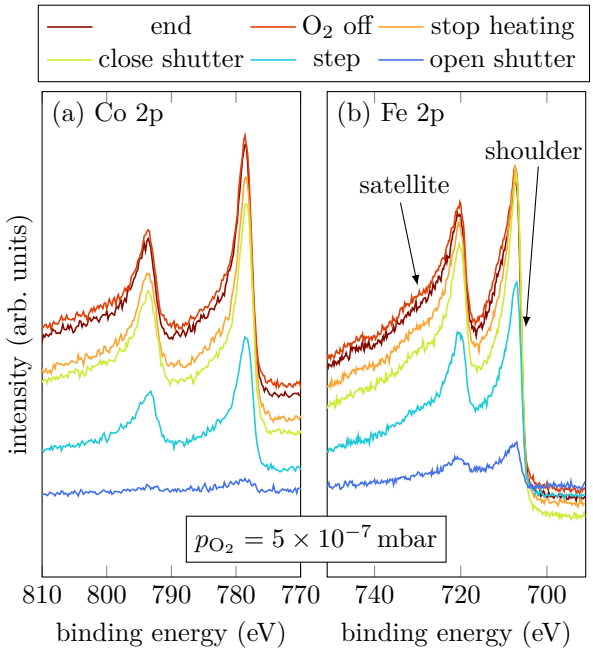

Fig. 6.2: HAXPES spectra of sample A for characteristic events, as displayed, of the Fe 2p and Co 2p core-levels.

The spectral shapes of both, Fe 2p and Co 2p, do not significantly change throughout the entire deposition process. In comparison with Figure 6.1, the last scan of the operando measurement shows that the spectra observed here indicate a major part of metallic Co and Fe as shown by the asymmetric peak shape. Nevertheless, oxidic contributions in Fe are recognizable, as indicated by the more pronounced shoulder and the emerging charge-transfer satellites at slightly higher binding energies than the main peaks.

Figure 6.3 summarizes the peak positions of the Fe 2p and Co 2p core-levels of all recorded spectra after fitting a Lorentzian function. It is obvious that all peaks except the Co $2p_{1/2}$ peak are shifted to lower binding energies within the very first scans. After the first few scans the peak positions remain constant within uncertainties. The Co $2p_{1/2}$ peak position remains constant from the very first scan. The observed peak positions of (793.6 ± 0.4) eV for the Co $2p_{1/2}$ and (778.6 ± 0.4) eV for the Co $2p_{3/2}$ peak agree well with the literature for metallic Co as reported by Betteridge [154]. For the Fe spectrum, the peak positions also agree well with observations for metallic Fe from the

literature [155].

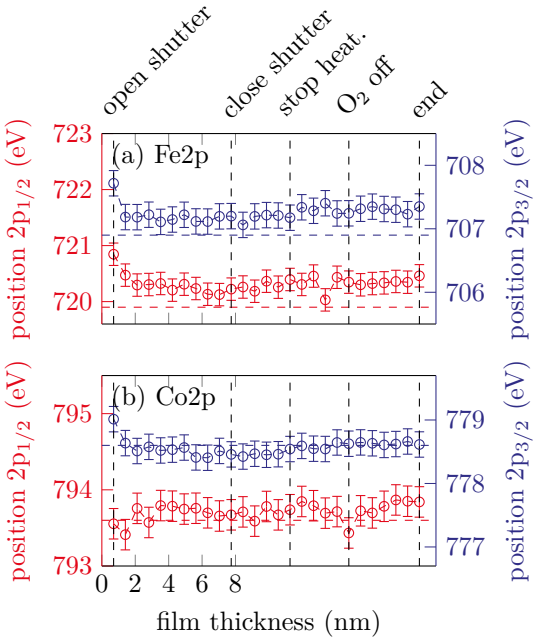

Fig. 6.3: Peak positions of the (**a**) Fe 2p and (**b**) Co 2p peaks for sample A. The horizontal dashed lines represent the respective literature values for metallic Fe and Co.

Sample B—Intermediate Oxygen Pressure

Sample B was grown with an intermediate oxygen partial pressure of 1×10^{-6} mbar. Figure 6.4a,b show the Co 2p and Fe 2p peaks, respectively, at selected steps during the RMBE process.

During evaporation, the spectra show that the cobalt atoms are mostly in a metallic Co^{0+} charge state, indicated by the absence of charge-transfer satellites (cf. Figure 6.1a). On the other hand, Fe grows oxidic with an amount of Fe^{2+}, indicated by the shoulder of the Fe $2p_{3/2}$ peak located at 705.8 eV (cf. Figure 6.4b) [156]. Once the shutter is closed, the Fe $2p_{3/2}$ and Fe $2p_{1/2}$ peaks are shifted to higher binding energies, which correlates to an increasing amount of Fe^{3+}. Moreover, a charge-transfer satellite between the Fe $2p_{1/2}$ and Fe $2p_{3/2}$ peak at around 717 eV becomes visible after the shutter is closed, suggesting a light increase of the Fe^{3+} amount due to stronger Fe oxidation than for low oxygen pressure. After heating is turned off, it is clearly visible that also Co oxidizes, indicated by the emergence of the satellites of the Co $2p_{1/2}$ and Co $2p_{3/2}$ peaks. Furthermore, there is only one satellite for the Co $2p_{1/2}$ peak clearly visible at (801.4 ± 0.8) eV, and the satellite for the Co $2p_{3/2}$ peak can only be guessed at around 786 eV (cf. Figure 6.4a).

Figure 6.5 shows the peak positions of the Fe $2p_{3/2}$, Fe $2p_{1/2}$, Co $2p_{3/2}$ and Co $2p_{1/2}$ peaks changing with film thickness.

It is clearly visible that both of the Fe 2p peak position remain constant for approximately the first 7.26 nm until the shutter is closed and then shift to higher binding energies with increasing scans, which corresponds to an increasing amount of Fe^{3+} valence states. After the heater is turned off, the peak positions remain constant at around (710.8 ± 0.4) eV for the Fe $2p_{3/2}$ and (723.7 ± 0.4) eV for the Fe $2p_{1/2}$ peak. The peak positions for both the Co $2p_{3/2}$ and Co $2p_{1/2}$ peaks remain constant within uncertainties until the heater is turned off, at around 778.5 eV and 793.7 eV, respectively. This indicates Co^{2+} valence states. After the heater is turned off, the peak positions shifting to

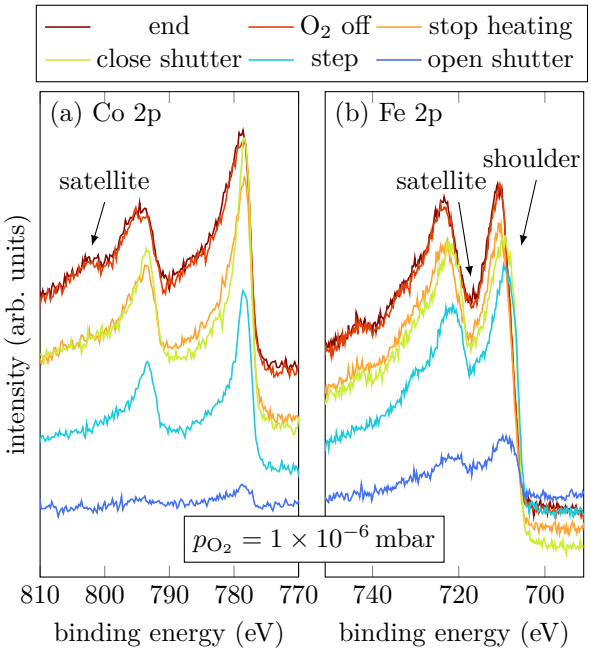

Fig. 6.4: HAXPES spectra of sample B for characteristic events, as displayed, of the Fe 2p and Co 2p core-leveles.

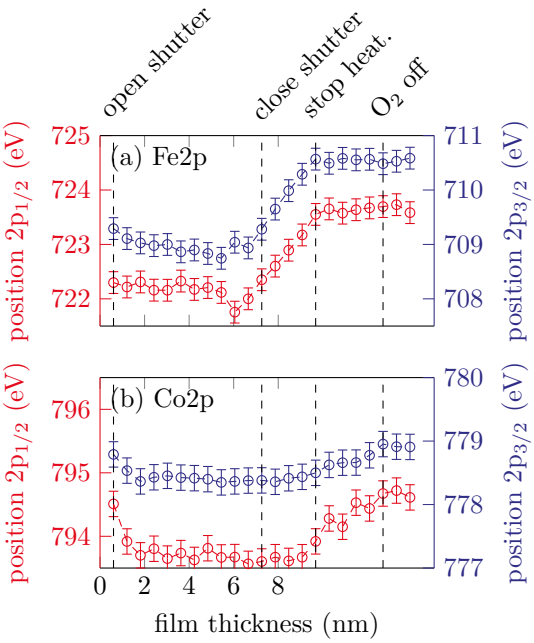

Fig. 6.5: Peak positions of the (**a**) Fe 2p and (**b**) Co 2p peaks for sample B.

higher binding energies until the oxygen valve is closed.

Sample C—High Oxygen Pressure

Sample C was grown with a high oxygen partial pressure of 5×10^{-6} mbar. Figure 6.6a,b show the Co 2p and Fe 2p peaks, respectively, at selected steps during the RMBE process.

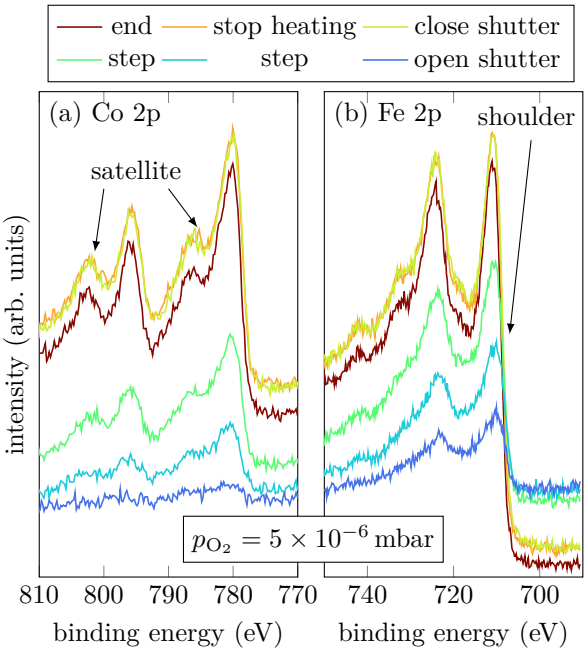

Fig. 6.6: HAXPES spectra of sample C for characteristic events, as displayed, of the Fe 2p and Co 2p core-leveles.

Looking at Co during growth, it is noticeable that immediately after the shutter is opened, the typical Co shape for Co^{2+} has formed. Two shake-up satellites of the Co $2p_{1/2}$ and Co $2p_{3/2}$ can be recognized, which are shifted to higher binding energies. The distance between main peaks and satellites is about (6.2 ± 0.5) eV, which indicates a Co^{2+} valence state [157–159]. During the whole evaporation process the satellites become more and more pronounced.

Interestingly, during the growth only divalent Fe seems to be present. This is indicated by the shoulder of the Fe $2p_{3/2}$ peak. Initially, the spectral region between the Fe $2p_{3/2}$ peak and the Fe $2p_{1/2}$ peak does not exhibit any satellite structure, which indicates mixed valences of Fe^{2+} and Fe^{3+}. However, starting at a film thickness of 4.6 nm, a satellite at 718.2 eV appears and becomes more and more pronounced with increasing thickness, but only in the spectra recorded after closing the shutter it is really pronounced indicating that Fe is only present in Fe^{3+} states.

Figure 6.7 shows the peak positions of the Fe $2p_{3/2}$, Fe $2p_{1/2}$, Co $2p_{3/2}$ and Co $2p_{1/2}$ peaks with respect to the film thickness.

The Fe peaks shifting to higher binding energies in the very first scans and then remain constant at around (710.8 ± 0.5) eV and (724.3 ± 0.5) eV for the Fe $2p_{3/2}$ and Fe $2p_{1/2}$, respectively. This is expected for the formation of cobalt ferrite with major Fe^{3+} content [157].

The Co 2p peak positions shift to lower binding energies with increasing film thickness. After the shutter is closed (12.6 nm) the peak positions remain constant at (780.3±0.4) eV and (795.8±0.4) eV for the Co $2p_{3/2}$ and Co $2p_{1/2}$, respectively. As mentioned before, this is an indicator for Co^{2+}, as expected for cobalt ferrite.

For a quantitative analysis of the HAXPES data, the intensities I_{Fe} and I_{Co} of the Fe 2p and Co 2p have been numerically integrated. For this purpose, the spectra were subtracted by a Shirley background and the relative photoelectron yield Y_{Fe} has been calculated by using the formula

$$Y_{Fe} = \frac{I_{Fe}/\sigma_{Fe}}{I_{Fe}/\sigma_{Fe} + I_{Co}/\sigma_{Co}}. \tag{6.1}$$

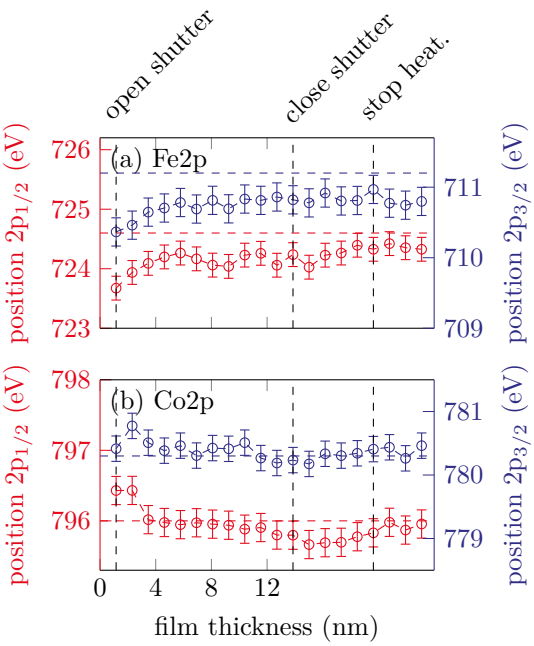

Fig. 6.7: Peak positions of the (**a**) Fe 2p and (**b**) Co 2p peaks for sample C. The horizontal dashed lines represent the respective literature values for CFO.

The photoionization cross sections σ were taken from Trzhaskovskaya et al. [72] with respect to the used excitation energy ($\sigma_{Fe} = 4024\,b$ and $\sigma_{Co} = 4513\,b$). For this sample we find a relative photoelectron yield of $Y_{Fe} = 0.644$. Using the relation $x = 3Y_{Fe}$, this leads to a stoichiometry of $Co_{1.07}\,Fe_{1.93}\,O_4$. For samples A and B we find a relative photoelectron yield of 0.606 and 0.607, respectively.

6.3.2 XRD

In order to control the structural properties of the samples, ex situ XRD measurements have been performed in $\theta-2\theta$ geometry after growth of the films. All data were scaled to the reciprocal lattice units (r.l.u.) of $SrTiO_3(001)$. Figure 6.8 shows the recorded XRD scans for all prepared samples.

For sample A grown with the lowest oxygen partial pressure, we find an addtional diffraction peak at a L-value of 2.729, which is in good agreement with a Co-Fe-alloy ($CoFe_2(002)$) as reported by Nishizawa and Ishida [160]. In addition, the first oscillation of very small Laue fringes, correlated to the peak of the Co-Fe-alloy, can be seen. This indicates a well-ordered crystalline film growth.

Comparing this to the sample with the intermediate oxygen partial pressure, we see that the peak at $L = 2.729$ remains with lower intensity, again indicating a $CoFe_2$ phase. In contrast to the sample discussed previously, a peak at $L = 1.881$ can now also be found, which can be attributed to CFO while, in principle, it can also be due to Fe_3O_4 [161]. Thus, the film is characterized by coexistence of metallic and oxidic phases.

For the sample grown with the highest oxygen partial pressure, which already shows CFO behavior in the HAXPES measurements, a diffraction peak is also seen in the XRD at $L = 1.878$, which points to the (004) Bragg reflex of $CoFe_2O_4$. The goal to produce crystalline epitaxial CFO is thus confirmed. For the samples with the medium and high oxygen partial pressure we find the (004) Bragg reflex of Fe_3O_4 and CFO at lower L values than the (002) Bragg reflex of the substrate due to its larger vertical atomic layer distances compared to $SrTiO_3(001)$.

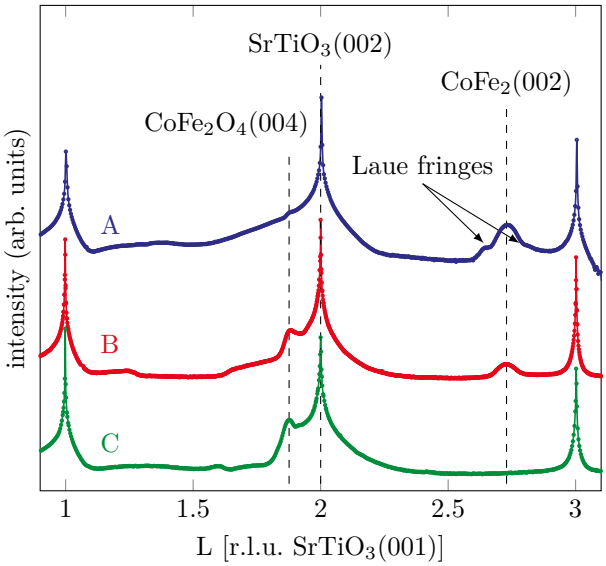

Fig. 6.8: XRD measurements after film deposition of the different samples with varying oxygen partial pressure.

6.4 Conlusions

In summary, three different $Co_xFe_{3-x}O_4$ samples with varying oxygen partial pressure were deposited on $SrTiO_3(001)$ substrates and chemically characterized in situ by means of time resolved operando HAXPES during film growth. For the lowest oxygen partial pressure of 5×10^{-7} mbar, the film grows almost exclusively metallic with only weak oxidic shoulders during the entire growth process. Increasing the oxygen partial pressure to 1×10^{-6} mbar, we see that cobalt first grows metallic and then oxidizes once heating is turned off. Iron grows first as Fe^{2+} states and then shows additional Fe^{3+} features after the shutter is closed. Increasing the oxygen partial pressure even further to 5×10^{-6} mbar the film appears to grow strictly as cobalt ferrite from the very beginning, as aimed for for spintronic applications.

Additional XRD measurements confirm the results obtained by the HAXPES measurements very well. For the sample with the lowest oxygen partial pressure, a Bragg peak can be seen which indicates formation of crystalline Co-Fe alloy. For the sample with the medium oxygen partial pressure, the Co-Fe alloy peak is still visible and another peak appears indicating a cobalt ferrite content. For the sample with the highest oxygen partial pressure, metallic contributions disappear and CFO Bragg peaks appear exclusively, indicating the growth of a CFO film of high structural quality.

Original publication: Materials **2022**, 15, 6911
available at http://doi.org/10.3390/ma15196911

Influence of Oxygen Plasma on the Growth and Stability of Epitaxial $NiCo_2O_4$ Ultrathin Films on Various Substrates

K. Ruwisch, A. Alexander, T. Pollenske, K. Kuepper, and J. Wollschläger

Department of Physics, Osnabrück University, Barbarastrasse 7, D-49076 Osnabrück, Germany

Abstract

In this work, we investigated the influence of oxygen plasma on the growth of nickel cobaltite ($NiCo_2O_4$) thin films compared to growth in a molecular oxygen atmosphere. The films were grown on MgO (001), $MgAl_2O_4$(001) and $SrTiO_3$(001) substrates by oxygen plasma (atmosphere of activated oxygen)-assisted and reactive molecular beam epitaxy (molecular oxygen atmosphere). Soft X-ray photoelectron spectroscopy showed that only the use of oxygen plasma led to a spectrum characteristic of $NiCo_2O_4$. Low energy electron diffraction measurements were conducted to obtain information on the structure of the film surfaces. The results proved the formation of a spinel surface structure for films grown with oxygen plasma, while the formation of a rock salt structure was observed for growth with molecular oxygen. To determine the film thickness, X-ray reflectivity measurements were performed. If oxygen plasma were used to grow $NiCo_2O_4$ films, this would result in lower film thicknesses compared to growth using molecular oxygen although the cation flux was kept constant during deposition. Additional X-ray diffraction experiments delivered structural information about the bulk structure of the film. All films had a rock salt bulk structure after exposure to ambient conditions. Angle-resolved hard X-ray photoelectron spectroscopy revealed a homogeneous depth distribution of cations of the grown film, but no typical $NiCo_2O_4$ spectrum anymore. Thus, on the one hand, $NiCo_2O_4$ films with a spinel structure prepared using activated oxygen were not stable under ambient conditions. The structure of these films was transformed into NiCo oxide with a rock salt structure. On the other hand, it was not possible to form $NiCo_2O_4$ films using molecular oxygen. These films had a rock salt structure that was stable under ambient conditions.

7.1 Introduction

In the rising field of spin-based electronics (e.g., spintronics or spincaloritronics) transition metal ferrites and cobaltite are of the utmost importance due to their high Curie temperature and significant magnetic saturation moments. To fabricate high quality spintronic devices, it is essential that highly spin-polarized electron currents be generated. Here, nickel cobaltite ($NiCo_2O_4$, NCO) is a very promising candidate for this application. NCO has a ferrimagnetic ordering and predicted half-metallic ground state [162]. NCO crystallizes in an inverse spinel structure with a lattice constant in the range of 8.114 and 8.185 Å with a ferrimagnetic Curie temperature of 673 K [122, 124, 163, 164]. Moreover, the tetrahedral sites could be occupied with Co^{2+} and Co^{3+} cations, while the octahedral sites are occupied with Ni^{2+}, Ni^{3+} and Co^{3+} cations. A coupling between conductivity and cationic distribution (the degree of inversion defined as a fraction of Co^{3+}

cations on tetrahedral sites) dependent on synthesis conditions has been reported [122], making p-type conducting NCO a promising candidate for future spintronic applications [121,122,165–167]. Further potential applications for NCO are, for example, infrared transparent electrodes [168,169] or supercapacitors [170,171] for energy storage [172–174].

In most studies, thin NCO films are deposited via sol-gel and thermal decomposition [175–177], pulsed laser deposition [122,125,168] or sputtering [178]. In this work, we used reactive molecular beam epitaxy (RMBE) and oxygen plasma-assisted molecular beam epitaxy (OPA-MBE) to prepare ultrathin NCO films. During the RMBE process, we used molecular oxygen while oxygen radicals were used during the OPA-MBE growth. In the following, we abbreviate RMBE prepared films with O_2 and OPA-MBE prepared films with O^*. Most commonly, NCO films are deposited on $MgAl_2O_4(001)$ ($a_{MAO} = 8.083\,Å$, MAO) due to its small lattice mismatch of only 0.4–1.2% and no expected antiphase boundaries (APB) due to growth of spinel on spinel structures. In this work, we also used MgO(001) ($a_{MgO} = 4.2117\,Å$) and $SrTiO_3(001)$ ($a_{STO} = 3.905\,Å$) substrates to investigate the influence of the crystal structure of the substrates (rock salt and perovskite, respectively) on the growth of NCO thin films. For these substrates, the lattice mismatch was -3.7 to -2.87% and 3.9 to 4.8%, respectively. Compared to previous studies that prepared NCO, we used both RMBE and OPA–MBE as a new fabrication pathway. Both MBE techniques are used to grow epitaxial films, which in turn are thermodynamically most stable, since the energy of the adatoms on the surface is much lower than in other processes, such as PLD or sputter deposition [179–181]. Since a plasma source (OPA–MBE) is highly expensive, it would be of the highest importance to produce NCO samples without such an additional source. Directly after deposition, the chemical composition in the near-surface region and the surface structure of the films were determined using in situ soft X-ray photoelectron spectroscopy (soft-XPS) and low energy electron diffraction (LEED), respectively. After transport under ambient conditions, ex situ X-ray reflectivity (XRR) and X-ray diffraction (XRD) measurements were performed to analyze the structural bulk properties. To analyze chemical properties not only in the near-surface region but also for the bulk properties of the films , hard X-ray photoelectron spectroscopy (HAXPES) experiments were also performed.

7.2 Materials and Methods

Ultrathin NCO layers were prepared on MgO(001), $MgAlO_2(001)$ and $SrTiO_3(001)$ single crystalline substrates by using reactive molecular beam epitaxy (RMBE) and oxygen plasma-assisted molecular beam epitaxy (OPA-MBE)in an ultrahigh vacuum system with a base pressure of 10^{-8} mbar in the deposition chamber. We prepared the films using molecular oxygen (O_2) and oxygen radicals (O^*) by means of a SPECS plasma source. For cleaning purposes, the substrates were annealed at 400 °C in an oxygen atmosphere of 1×10^{-4} mbar for 1 h. Subsequently, XPS and LEED measurements were performed to monitor the chemical cleanliness and crystallinity of the surface. To grow the NCO thin films, two evaporators with pure nickel and cobalt rods were used to deposit the material on the substrates at a temperature of 250 °C in an oxygen atmosphere of 5×10^{-6} mbar for both deposition types (RMBE, OPA-MBE).After film deposition, stoichiometry and surface structure were controlled by soft-XPS (Mg K_α, $h\nu = 1254$ eV) using a SPECS Phoibos HSA 150 hemispherical analyzer and a LEED.After transport under ambient conditions, XRR and XRD measurements were performed at beamline P08 of Deutsches Elektronensynchrotron (DESY) [182]. For these measurements, a photon energy of 18 keV and a six-circle diffractometer with a two-dimensional PILATUS 100k detector was used. Additional HAXPES experiments were also performed at DESY at beamline P22 [183] using a SPECS Phoibos 225 HV hemispherical analyzer with a delay line detector and a wide angle lens. With this setup, the chemical composition of the films was investi-

gated throughout the whole film, due to a high probing depth based on the energy of $h\nu = 6000\,\text{eV}$. The information depth D_I^{95} from where 95 % of the detected photoelectrons were emitted could be calculated using the equation

$$D_\text{I}^{95} \approx 3\lambda \cos\phi, \tag{7.1}$$

where λ is the inelastic mean free path (IMFP), and ϕ is the off-normal emission angle. With the Tanuma, Powell and Penn algorithm formula we estimated the IMFP for various atomic orbitals [66]. The maximum information depth was given for an angle of $\Phi = 0°$ and is 21.5 nm (Co 2p) and 21.2 nm (Ni 2p), respectively. Compared to soft-XPS where the probing depth was only 3.1 nm for Ni 2p and 3.4 nm for Co 2p, and therefore sensitive to the surface, HAXPES delivered more bulk information.

7.3 Results and Discussion

7.3.1 LEED

LEED measurements were made directly after deposition of the NCO films. Figure 7.1 presents the LEED patterns recorded at an electron energy of 151 eV of the initially cleaned substrate surfaces, as well as the films with oxide films prepared using O_2 or O^*.

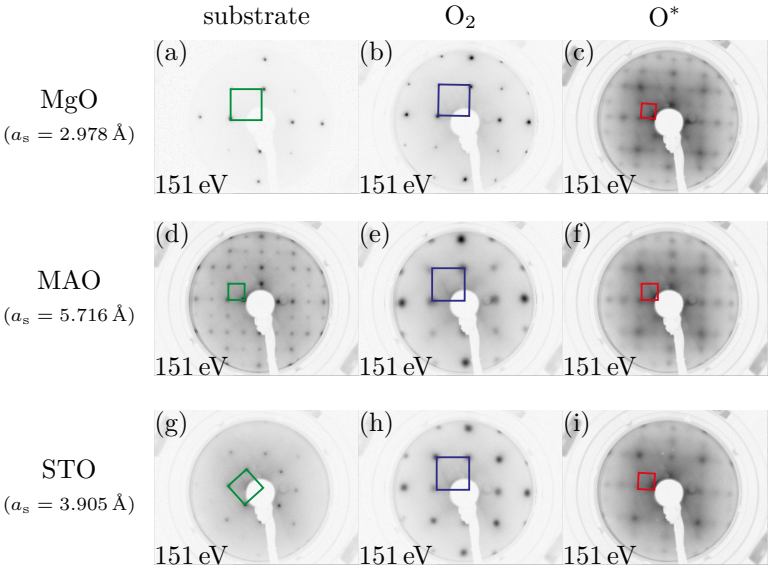

Fig. 7.1: LEED patterns recorded at 151 eV for the substrates (first column: (**a**,**d**,**g**), the films prepared with O_2 (second column: (**b**,**e**,**h**)) and the films prepared with O^* (third column: (**c**,**f**,**i**)). a_s are the surface lattice constants of the respective substrates. The squares represent reciprocal surface unit cells. The films prepared using O_2 showed a (1×1) surface structure, which is too large to be a spinel structure, whereas the films prepared using O^* showed a spinel structure.

The LEED patterns show sharp (1×1) diffraction spots for the substrates space.Looking at the films prepared with molecular oxygen, it was noticeable that the reciprocal surface unit cell was too large to be a spinel structure compared to the one in Figure 7.1d. Another indicator was that both the reciprocal unit cell of the MgO substrate (cf. Figure 7.1a) and that of the prepared film showed a comparable size (cf. Figure 7.1b). Therefore, the film with molecular oxygen could be either CoO with a surface constant of $a_\text{s} = 3.012\,\text{Å}$ or NiO with a surface constant of $a_\text{s} = 2.954\,\text{Å}$ or a mixture of both oxides. It was noticeable that sharp reflections were only discernible for the film

on MgO, whereas the other two films showed much blurrier reflections (cf. Figure 7.2a), indicating a less ordered structure. A (1×1) structure was also evident in the films prepared in an oxygen plasma atmosphere. Moreover, these films exhibited a reciprocal surface unit cell similar to that of the MAO substrate that has spinel structure. Thus, the films prepared with oxygen plasma showed a spinel structure as expected for NCO films. For both kinds of preparation, an analysis of the full width at half maximum (FWHM) of the reflexes, as shown in Figure 7.2a, both quantifies and confirms the visual impression from the LEED patterns.

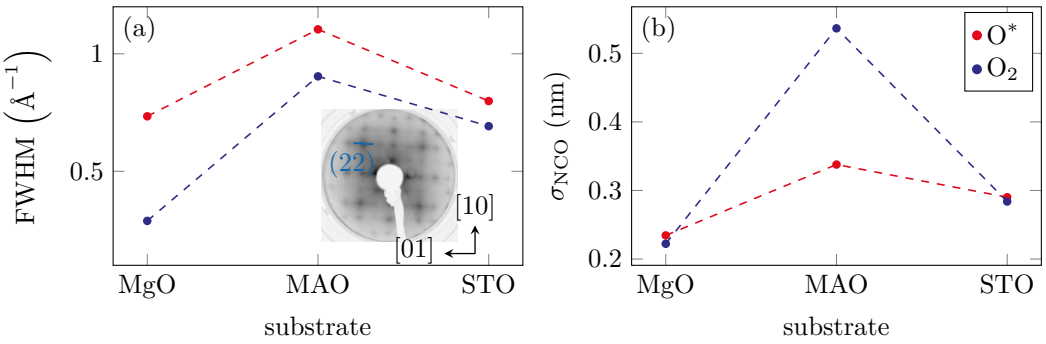

Fig. 7.2: (**a**) FWHM of the (22) reflex with respect to the substrate (cf. inset). The FWHM was the highest for the MAO substrates. In general, the films with molecular oxygen exhibit a smaller FWHM than those with oxygen radicals. (**b**) RMS surface roughness σ_{NCO} of NCO. Here, also the surface roughness was the highest for the MAO substrate. In contrast to the FWHM, the surface roughness was higher for the films prepared with O_2 than for the O^* films.

Obviously, the FWHM was much larger for the O^* than for the O_2 films. This indicated that more surface defects were created during the latter preparation. It could also be seen that the FWHM of the NCO film on the MAO substrate was generally higher than for the others. This seemed surprising since both the substrate and film have a spinel structure, and the lattice mismatch of the film and substrate was only 0.4 to 1.2 %. Furthermore, we expected high quality films due to the matching of spinel on spinel without the formation of antiphase boundaries.

7.3.2 Soft-XPS

Soft-XPS measurements were made directly after deposition of the NCO films to investigate both stoichiometry and valence states of the cation species. Since soft-XPS was used with a low excitation energy and therefore a small information depth, this method delivered insight into the near-surface region. Figure 7.3 shows the core-level spectra of the Ni 2p and Co 2p orbitals. All spectra were calibrated according to the binding energy of the O 1s peak ($E_B = 530\,eV$).

All of the Ni 2p spectra showed a similar shape regardless of deposition in O_2 or O^*. All main peaks and all satellites appeared at the same binding energy. We found binding energies of 872.3 ± 0.3 and 855.0 ± 0.5 eV for Ni $2p_{1/2}$ and Ni $2p_{3/2}$, respectively. The distance between the satellites and the main spin-orbit split peaks is about 7 eV indicating the presence of Ni^{2+} cations [159]. The presence of the high binding energy shoulder of the Ni $2p_{3/2}$ peak was reported for the formation of NiO and therefore another indicator of the existence of Ni^{2+} cations [184].

For the spectra of the Co 2p region, we found a different behavior concerning the shape of the shake-up satellites. All of the main peaks and satellites appeared at the same binding energy, even for the films prepared with a plasma source (O^*). The positions of the main spin-orbit split peaks were at 796.0 ± 0.4 eV and 780.1 ± 0.3 eV for Co $2p_{1/2}$ and Co $2p_{3/2}$, respectively. Furthermore, the shakeup satellites are around a 6.5 ± 0.5 eV higher binding energy than the correlated photoelectron

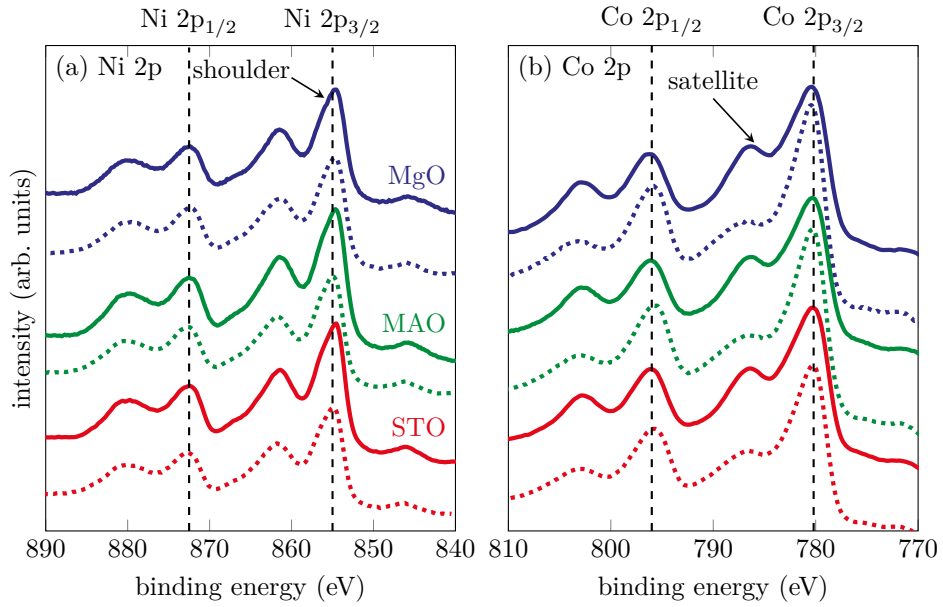

Fig. 7.3: Soft-XP spectra of the (**a**) Ni 2p and (**b**) Co 2p core-levels. The solid lines represent the films prepared with O_2 while the dashed lines represent the films prepared with O^*. The vertical dashed lines represent the literature values for the respective main spin-orbit split peaks. The highlighted satellite is less distinguished for the films prepared with O^*.

peaks, indicating a Co^{2+} valence state [157–159]. However, here we found a difference in the shape of the spectra with respect to growth in O_2 or O^*. The high binding energy satellites of the Co $2p_{3/2}$ and Co $2p_{1/2}$ peaks were less distinguished for the films grown in O^* than O_2. As reported in the literature, this is evidence for the presence of Co^{3+} cations, as expected for the formation of NCO [176, 185]. We could therefore state that using a plasma source changed the oxidation state of the Co valences because of exposure to O^*.

For a quantitative analysis of the XPS data, the intensities I_{Ni} and I_{Co} of the entire Ni 2p and Co 2p spectra shown in Figure 7.3 were numerically integrated after subtracting a Shirley background. The relative Ni photoelectron yield Y_{Ni} was calculated by using the formula

$$Y_{Ni} = \frac{I_{Ni}/\sigma_{Ni}}{I_{Ni}/\sigma_{Ni} + I_{Co}/\sigma_{Co}}, \tag{7.2}$$

after canceling the inelastic mean free path λ. The photoionization cross-sections σ_i were taken from Trzhaskovskaya et al. [72] with respect to the excitation energy. For all films we found a yield corresponding to a stoichiometry of Co–Ni = 2:1 within uncertainties and as expected for the formation of $NiCo_2O_4$.

7.3.3 XRR

XRR measurements were performed ex situ to determine film thickness as well as film roughness. Figure 7.4 shows the measured and calculated reflectivity curves after optimizing the structural parameters of the single-layer model using the Parratt algorithm [54] and the Névot–Croce roughness model [56]. The fitted curves were in good agreement with the experimental data. The resulting film thicknesses were depicted inside the figure. All samples grown in O^* showed comparable film thickness within uncertainties. We also obtained this result for all samples grown in O_2. Obviously,

with the same evaporation parameters, the use of oxygen radicals for the growth of the films led to a smaller film thickness than with molecular oxygen. This may point to partial ion etching of the films grown in an O^* atmosphere. Furthermore, the RMS roughnesses of the films were determined as presented in Figure 7.2b. We found values in the range between 0.2 nm and 0.6 nm and a similar behavior for the LEED FWHM, as significantly higher values occurred for the MAO substrate than for the others.

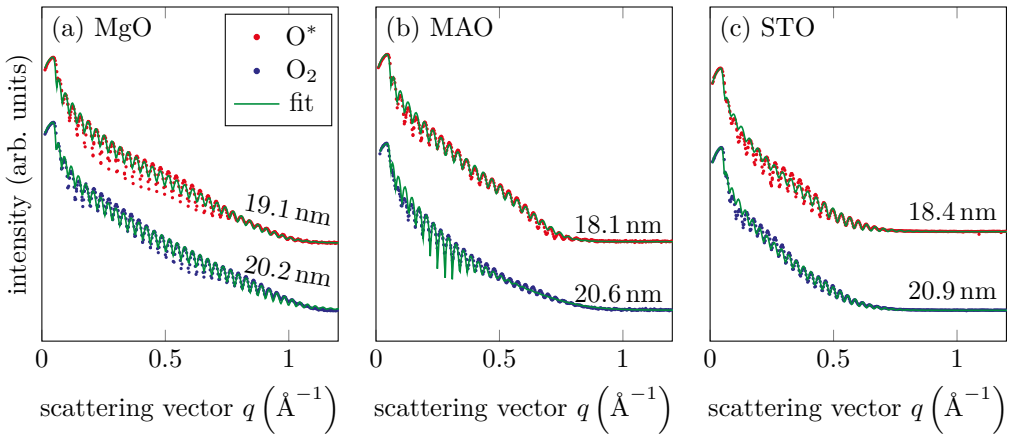

Fig. 7.4: XRR measurements and fitted intensity curves of all films for (**a**) MgO substrate, (**b**) MAO substrate and (**c**) STO substrate. The fitted film thicknesses are shown on the respective curves. The films prepared with O^* exhibited smaller film thicknesses compared to those prepared with molecular oxygen. All films prepared by the same technique showed comparable thicknesses.

7.3.4 XRD

XRD measurements in θ–2θ geometry were performed ex situ after the growth of the films to control their structural properties in detail. Figure 7.5 shows the results of the XRD measurements along the (00L) out-of-plane direction. The (00L) scans were measured along the MgO(002), MAO(004) and STO(002) Bragg reflections.

For the two films grown on the MgO(001) substrate using O_2 or O^* (cf. Figure 7.5a), we observed clear Laue fringes, indicating a high crystalline ordering and homogeneous thickness. The fringes were much less pronounced for films grown on the STO substrate (cf. Figure 7.5c) and nearly vanished for films grown on the MAO substrate (cf. Figure 7.5b). Therefore, we could state that the ordering of the oxide films depends heavily on the substrate. The ordering increases from films grown on MAO(001) to films grown on STO(001) while films deposited on MgO(001) had the highest ordering. This finding agreed well with our analysis of the FWHM of the LEED reflexes and of the surface roughness obtained from XRR. For a quantitative analysis, peak position and the FWHM of the oxide Bragg peaks were determined by fitting a Gaussian function. On the MAO substrate, we found next to the Bragg reflex of the substrate an additional diffraction peak of the oxide at a q-value of $2.821\,\text{Å}^{-1}$ (O^*) and $2.814\,\text{Å}^{-1}$ (O_2). The XRD data of the films on the STO substrate provided q-values of $2.726\,\text{Å}^{-1}$ (O^*) and $2.727\,\text{Å}^{-1}$ (O_2). For the films grown on MgO(001), we could only roughly estimate the film position to $q = 2.948\,\text{Å}^{-1}$ (O^*) and $2.943\,\text{Å}^{-1}$ (O_2) from the Laue fringes since the Bragg peaks of the film and substrate strongly overlapped.

In addition, the dashed lines in Figure 7.5 showed the expected position for bulk CoO(002) and NiO(002). For NCO(004), we provide a range for the expected position due to the different possible lattice constants. Obviously, we obtained the best agreement for CoO films grown on MgO(001), but the Bragg positions of the films deposited on MAO(001) and STO(001) were shifted to lower values,

indicating higher atomic layer spacings. This may have been attributed to an elastically distorted oxide film-to-lattice matching of film and substrate at the interface (pseudomorphic growth).

Figure 7.6 shows the vertical layer distances c_f obtained for the oxide films on the different substrates with respect to their lateral layer distances. The vertical layer distance c_f of the films increased with decreasing lateral layer distances a_{sub} of the used substrates, as was expected for elastic distortion of the films.

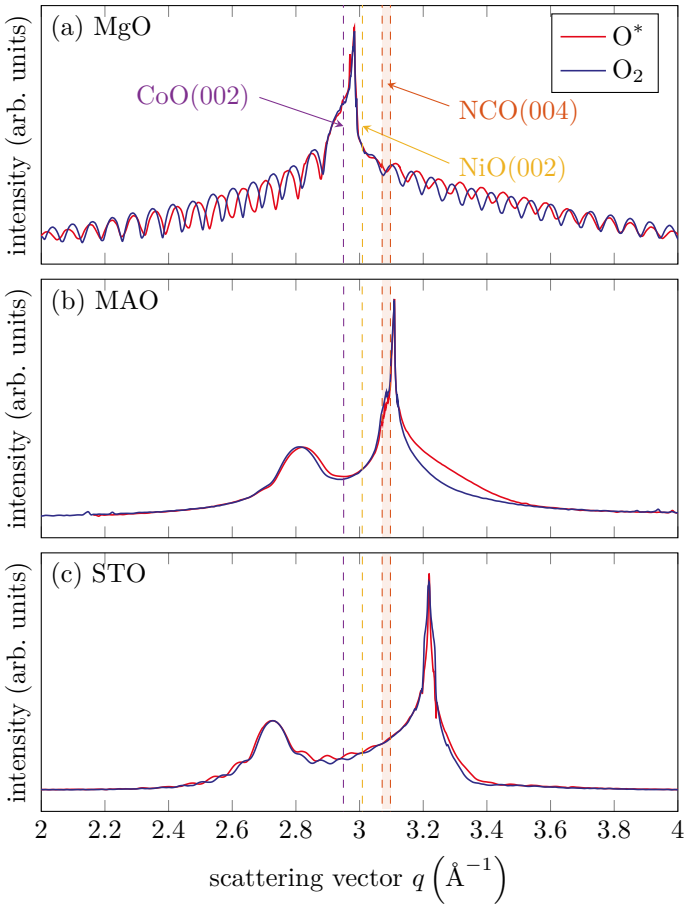

Fig. 7.5: XRD measurements of the (00L) CTR across the (**a**) MgO(002), (**b**) MAO(004) and (**c**) STO(002) Bragg reflections. Dashed lines indicate the theoretical CoO(002) and NiO(002) Bragg peak positions for bulk material. Due to the possible lattice constants, a range of potential Bragg peak positions emerges for NCO(004). For (**a**) the film peak position agreed well with the theoretical value of CoO(002). In contrast, the film peak position for (**b**,**c**) show no agreement with the theoretical values.

The elastic vertical distortion Δc_f of the film is related [34] to its lateral distortion Δa_f via

$$\frac{\Delta c_f}{c_{f,0}} = \frac{-2\nu}{1-\nu}\frac{\Delta a_f}{a_{f,0}}. \tag{7.3}$$

Here, $c_{f,0}$ and $a_{f,0}$ denote the bulk values of the vertical and lateral atomic layer spacing of the oxide film, and ν denotes the Poisson ratio. Assuming $\nu = \frac{1}{3}$ and pseudomorphic growth on the different substrates, the calculated vertical layer distances for the NCO, NiO and CoO films are presented in Figure 7.6 using triangles. Uncertainties of the calculated c_f marked in Figure 7.6 are due to assumed uncertainties of the Poisson ratio $\Delta\nu = \pm\frac{1}{15}$.

The best agreement to the measured data was obtained for CoO films. Therefore, it could be

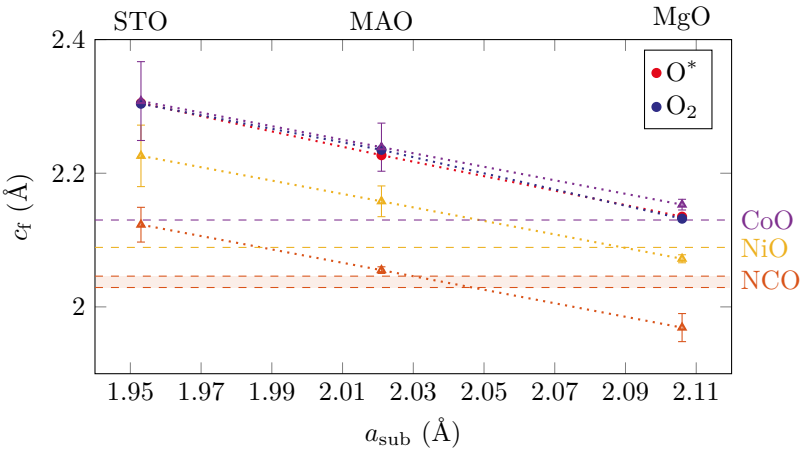

Fig. 7.6: Vertical layer distance c_f with respect to the lateral layer distance a_{sub} of the used substrates determined by the oxide film peak position. Furthermore, the theoretical vertical layer distances for bulk CoO, NiO and NCO are displayed with dashed horizontal lines along with the expected vertical layer distances for pseudomorphic growth on the different substrates (triangles).

speculated that the spinel structure of the NCO film grown in O* was transformed into a mixed CoNi oxide with a rock salt structure, as discussed in detail below.

The FWHM of the film Bragg peak was used to estimate the vertical crystallite size D^{vert}_{cryst} using the Scherrer equation [46]. Crystallite sizes of 64.9 Å (O*) and 67.3 Å (O_2) can be found for the films grown on the MAO substrate, which led to $\sim$ 33 % of the calculated film thicknesses. After evaluating the FWHM of the film Bragg peaks on the STO substrate, the values for D^{vert}_{cryst} of 77.4 Å (O*) and 84.1 Å (O_2) and around 40 % of the respective film thicknesses were. On the MgO substrate we estimated the vertical crystallite size using the distance between the Laue fringes and found 97.6 Å (O*) and 105.0 Å (O_2), which was nearly 50 % of the film thickness. Thus, the vertical crystallite size increased for growth on MAO(001) to STO(001) and was best for the growth on MgO(001). This result agreed well with the analysis of the surface roughness obtained by XRR as well as the analysis of the FWHM of the LEED reflexes.

Furthermore, XRD measurements were performed along the (11L) rod of each substrate to get information about the spinel structure of the oxide films. As an example, results for the STO substrate are shown in Figure 7.7.

On the STO substrate, we identified Bragg peaks close to the STO(111) and STO(113) reflex. However, there was no Bragg peak close to STO(112), indicating the absence of a spinel structure, but this finding can be explained by the formation of oxide films with a rock salt structure [186].

7.3.5 HAXPES

To get more information about the stoichiometry and chemical properties in bulk, HAXPES measurements were performed at different photoemission angles. Figure 7.8 shows sample HAXPES data for the films on the MAO and STO substrates for photoemission angles of 5°, 45° and 60°.

It was quite obvious that all the spectra had an identical shape. Only the background increased for higher photoemission angles, due to lower intensity. Compared with the soft-XPS measurements for films not exposed to ambient conditions, the satellite of the Co $2p_{3/2}$ peak (cf. Figure 7.8 dashed lines) was very distinctive and showed no difference in the two preparation methods. As explained before, the pronounced intensity of this satellite pointed to the formation of CoO. Therefore, we could assume that the formation of NCO with a spinel structure was only stable under vacuum

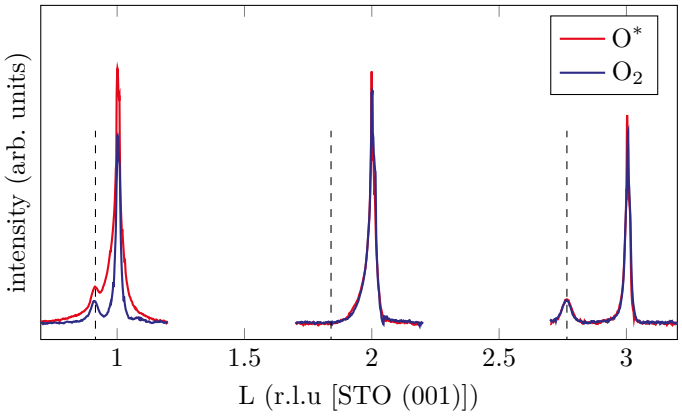

Fig. 7.7: XRD measurements along (11L) CTR across the STO(11L) Bragg reflection. The dashed lines represent the peak positions of the oxide film. Bragg peaks can be identified close to the STO(111) and STO(113) reflex but not the STO(112). Thus, the oxide films have rock salt structure and do not show spinel structure.

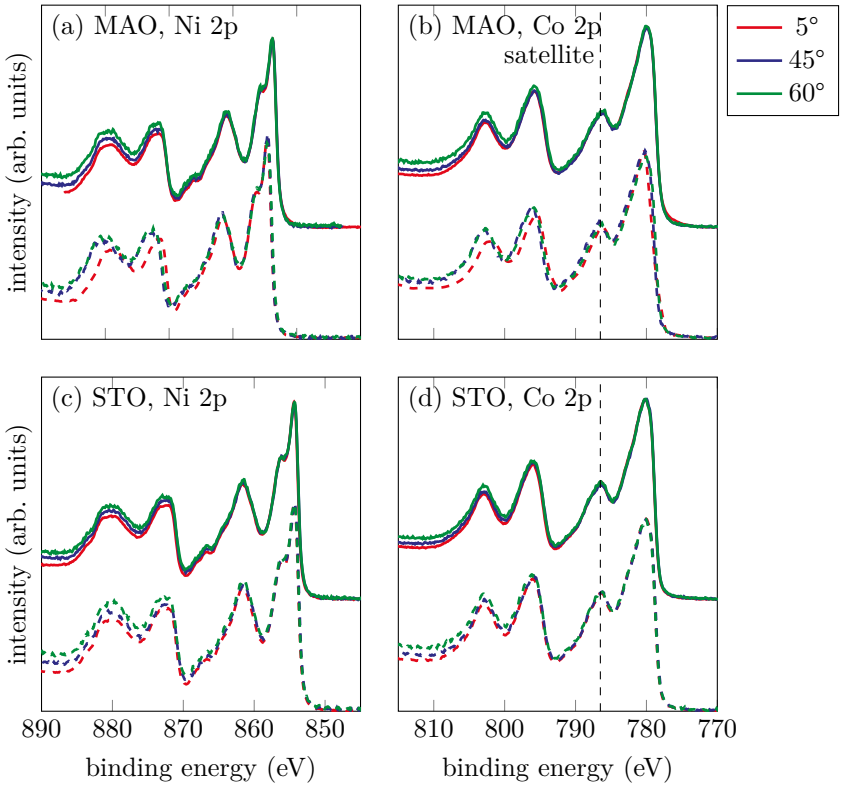

Fig. 7.8: HAXPES measurements for the films on MAO (**a**,**b**) and STO (**c**,**d**) substrates for several photoemission angles. The solid lines represent the films prepared with O_2 while the dashed lines represent the films prepared with O^*. All data were scaled to maximum intensity for better comparability. Regardless of the oxygen used, the shape of the spectra was identical for all films.

conditions, and exposure to ambient conditions reduced the film. By obtaining different depths of information in HAXPES, it was possible to conclude further that the Ni and Co cations were homogeneously distributed throughout the entire film.

7.4 Conclusions

We prepared stoichiometric NCO films on MgO(001), MAO(001) and STO(001) substrates by means of RMBE and OPA-MBE. In situ soft-XPS and LEED reveal high quality thin films. For the films prepared with oxygen plasma, we found a spinel surface structure in the LEED as well as low intensity for the Co $2p_{3/2}$ satellite in soft-XPS, which also indicated an NCO spinel structure. On the other hand, it was not possible to create NCO with a near-surface inverse spinel structure using RMBE. In this case, a NiCo oxide film with an apparent rock salt structure was formed. Thus, the high reactivity of atomic oxygen seemed to be necessary to obtain NCO films.

XRR measurements showed a comparable thickness for all prepared films with the same evaporation parameters. Using O^* during evaporation led to a smaller film thickness. Moreover, the RMS roughness was in good agreement with the FWHM of the NCO film reflexes, yet both values were the highest for the MAO substrate although the lattice mismatch was the lowest there.

XRD measurements after exposure to ambient conditions were performed in a θ–2θ geometry. We observed clear Laue fringes for films on the MgO substrate, indicating a highly crystalline ordering and a homogeneous film thickness. These Laue fringes were less distinguishable for the STO substrate and completely vanished for films on the MAO substrate. Therefore, the ordering of the oxide films depended highly on the substrate. The theoretical lattice mismatch of NCO on the various substrates was the lowest for MAO (0.4–1.2%), so it is surprising that the ordering was the worst here and the best for the MgO substrate with a lattice mismatch of -3.7 to -2.87%. After evaluating the oxide Bragg film peak positions we determined the vertical layer distances of the films, which was in good accordance with the pseudomorphic growth of CoNi oxide films with rock salt structure. Therefore, the best lattice matching was obtained for growth on MgO(001). The vertical crystallite grain sizes were calculated from the FWHM of the Bragg positions of the oxide films. The crystallite size was the most pronounced for the MgO substrate and the least for the MAO substrate. To evaluate the formation of the spinel structure of the oxide films, XRD measurements along the (11L) CTR of STO were performed. Whereas film peaks were visible close to the STO(111) and STO(113) Bragg peaks, no peak was visible close to the STO(112) Bragg peak, indicating the formation of a rock salt structure and thus no spinel structure. Additional HAXPES measurements confirmed the previous observations. The satellites of the Co $2p_{3/2}$ peak were very distinctive compared to the soft-XPS measurements, therefore pointing to an absence of Co^{3+} cations, which are a characteristic of stoichiometric NCO.

Thus, the preparation of stoichiometric $NiCo_2O_4$ with an inverse spinel structure was successful using a plasma source that formed oxygen radicals. When the films were prepared with molecular oxygen, a rock salt structure was seen in the LEED. However, after exposure to ambient conditions, the film is reduced with contracted crystalline structure and a rock salt structure was observed in all films. A possible solution to this effect could be to prepare a capping layer to protect the surface from external influences.

8 Summary and outlook

In this work, Fe_3O_4, $CoFe_2O_4$ and $NiCo_2O_4$ ultrathin films were grown on MgO(001), $MgAl_2O_4$(001) and $SrTiO_3$(001) substrates and investigated in terms of their structural, magnetic as well as electronic properties. For this purpose, the present work is divided into three parts.

In the first part (see Chap. 5), two series of $Fe_3O_4/Co_xFe_{3-x}O_4$ (x=0.5 and x=1) bilayers with different Fe_3O_4 layer thicknesses are grown on MgO(001). Here, the cobalt ferrite (CFO) layer thicknesses are kept constant and the magnetite layer thickness varies from 0 nm over ~ 3 nm up to ~ 13 nm. The first series incorporates stoichiometric CFO (x=1), whereas the other series contains unterstoichiometric CFO (x=0.5). The structural properties were carried out using XRR and in situ LEED measurements. To learn more about the electronic properties and stoichiometry of the films, in situ soft-XPS, HAXPES, and temperature-dependent XAS and XMCD measurements were also performed. Magnetic properties were investigated using the complementary measurement method SQUID. The in situ LEED and XPS measurements show high quality thin films. In the stoichiometric series, a clear charge-transfer satellite is seen in the soft-XP spectrum of the CFO film, indicating an increased Fe^{3+} content. With increasing Fe_3O_4 film thickness of the whole stack, the Fe $2p$ satellites shift to lower binding energies as seen in the HAXPES spectra, which is the reason why an increasing Fe^{2+} content can be concluded. After evaluation of the CTM calculations based on the XMCD data, the understoichiometric pure CFO sample shows a significantly higher magnetic moment due to the increased Fe content. For the stoichiometric bilayers, an increased magnetization is found at the interface, for which no clear explanation has been found so far. The typical exchange-spring behavior expected for this material system can be confirmed by SQUID measurements.

The second part of the experimental results (see Chap. 6) deals with the behavior in the early stages of the growth of $CoFe_2O_4$ layers on $SrTiO_3$(001) as a function of the oxygen partial pressure. For this purpose, in situ HAXPES measurements were performed during the deposition process and thus information about the electronic structure of the layers was obtained for each growth step. Furthermore, the influence on different stages of the evaporation process (closing of the shutter, switching off the heating, etc.) was analyzed. Final XRR and XRD measurements provide information about the structure of the films prepared. For the sample grown with the lowest oxygen partial pressure, only metallic growth with very weakly pronounced oxidic shoulders is obtained. For the sample with the medium oxygen partial pressure, two things are revealed. First, cobalt initially grows metallic and only after the heater is turned off it oxidizes and second, iron initially shows only Fe^{2+} features and after the shutter is closed additional Fe^{3+} features form. With the highest oxygen partial pressure used here, exactly the expected cobalt ferrite growth shows up from the beginning. The final XRD measurements confirm the previously observed findings from the HAXPES measurements.

In the third and last part of the experimental results (see Chap. 7), the material system is changed to the also cobalt-based spinel $NiCo_2O_4$ and here a novel procedure is chosen for the growth on the substrates MgO(001), $MgAl_2O_4$(001) and $SrTiO_3$(001). This approach consists of preparing the films using oxygen plasma assisted molecular beam epitaxy and reactive molecular beam epitaxy. Thus, the influence of these methods in combination with different chosen substrates can be investigated simultaneously. Using in situ LEED and XPS, the structural and electronic properties were already investigated directly after preparation. Only the samples using oxygen plasma show

a typical $NiCo_2O_4$ XP spectrum as well as a spinel structure in LEED. Additional ex situ XRR measurements confirm comparable film thicknesses. After the samples were transported under ambient conditions, all films show rock salt behavior in the XRD data and also in the HAXPES measurements no typical $NiCo_2O_4$ typical shapes can be seen anymore. Thus, it can be concluded that the films are stable only under UHV conditions and the transport under ambient conditions destroyed the spinel structure at the surface.

It can thus be stated that high-quality films were produced in this work, whose structural, electronic and magnetic properties were investigated in detail. In some cases, novel methods were used for film fabrication, although their final use still requires further adjustments and analysis.

In order to better understand the coupling phenomena between Fe_3O_4 and $CoFe_2O_4$ layers, further complementary calculations of the electronic structure would be helpful. To also obtain information regarding magnetism from deeper layers, XMCD experiments with fluorescence yield could provide a significant contribution. When performing x-ray resonant magnetic reflectivity (XRMR) measurements, important information about the magnetic behavior at the interface of these heterostructures could be obtained. Furthermore, from the preparation point of view, it would also be interesting to prepare stacks whose order is reversed, i.e. $CoFe_2O_4$ as top layer on Fe_3O_4 layers.

The growth of Fe_3O_4 layers can be studied even better if, for example, further oxygen partial pressures, i.e. a finer increment, are used. An additional important parameter is the temperature during growth. Again, additional temperatures can be used to gain ideas about the optimal vapor deposition temperature. In conclusion, additional XMCD and SQUID measurements would provide information about the magnetic and electronic structure, again very interesting for spintronics applications.

In order to exploit $NiCo_2O_4$ films for use in spintronic devices, it is important to investigate other growth parameters. For example, the time of cooling in oxygen atmosphere could have a crucial influence on growth of the films. Furthermore, parameters such as the general oxygen partial pressure and vapor deposition temperature should be investigated. Since research in the field of fabrication and characterization of ultrathin $NiCo_2O_4$ films using RMBE is not yet advanced, measurements regarding the magnetic and electronic structure are also of fundamental interest.

9 List of publications

1. **K. Ruwisch**, A. Alexander, T. Pollenske, K. Küpper, and J. Wollschläger
"Influence of Oxygen Plasma on the Growth and Stability of Epitaxial $NiCo_2O_4$ Ultrathin Films on Various Substrates"
Materials **15**(19), 6911 (2022);
doi:10.3390/ma15196911
2. T. Pohlmann, F. Bertram, J. Thien, J. Rodewald, **K. Ruwisch**, T. Kuschel, E. Weschke, K. Kuepper, and J. Wollschläger
"Structural and magnetic investigation of the interfaces of Fe_3O_4/MgO(001) with and without NiO interlayer"
Phys. Rev. B **105**, 235436 (2022);
doi:10.1103/PhysRevB.105.235436
3. **K. Ruwisch**, T. Pohlmann, F. Bertram, C. Schlueter, A. Gloskovskii, K. Küpper, and J. Wollschläger
"Real-Time Monitoring the Growth of Epitaxial $Co_x\,Fe_{3-x}O_4$ Ultrathin Films on Nb-Doped $SrTiO_3$(001) via Reactive Molecular Beam Epitaxy by Means of Operando HAXPES"
Materials **15**(7), 2377 (2022);
doi:10.3390/ma15072377
4. T. Pohlmann, M. Hoppe, J. Thien, A. Bikash Dey, A. Alexander, **K. Ruwisch**, O. Gutowski, J. Röh, A. Gloskovskii, C. Schlueter, K. Küpper, J. Wollschläger, and F. Bertram
"Time-resolved x-ray diffraction and photoelectron spectroscopy investigation of the reactive molecular beam epitaxy of Fe_3O_4 ultrathin films"
Phys. Rev. B **105**, 045412 (2022);
doi:10.1103/PhysRevB.105.045412
5. J. Thien, J. Bahlmann, A. Alexander, **K. Ruwisch**, J. Rodewald, T. Pohlmann, M. Hoppe, F. Alarslan, M. Steinhart, B. Altuncevahir, P. Shafer, C. Meyer, F. Bertram, P. Shafer, J. Wollschläger, and K. Küpper
"Cationic Ordering and Its Influence on the Magnetic Properties of Co-Rich Cobalt Ferrite Thin Films Prepared by Reactive Solid Phase Epitaxy on Nb-Doped $SrTiO_3$(001)"
Materials **15**(1), 46 (2022);
doi:10.3390/ma15010046
6. **K. Ruwisch**, T. Pohlmann, M. Hoppe, F. Bertram, P. Shafer, J. Wollschläger, and K. Küpper
"Interface Magnetization Phenomena in Epitaxial Thin $Fe_3O_4/Co_xFe_{3-x}O_4$ Bilayers"
J. Phys. Chem. C **125**(42), 23327–23337 (2021);
doi:10.1021/acs.jpcc.1c05274
7. G. Glavan, I.A. Belyaeva, **K. Ruwisch**, J. Wollschläger, and M. Shamonin
"Magnetoelectric Response of Laminated Cantilevers Comprising a Magnetoactive Elastomer and a Piezoelectric Polymer, in Pulsed Uniform Magnetic Fields"
Sensors **21**, 6390 (2021);
doi:10.3390/s21196390
8. T. Pohlmann, T. Kuschel, J. Rodewald, J. Thien, **K. Ruwisch**, F. Bertram, E. Weschke, P. Shafer, J. Wollschläger, and K. Kuepper

"Cation- and lattice-site-selective magnetic depth profiles of ultrathin Fe_3O_4(001) films"
Physical Review B **102**, 220411 (2020);
doi:10.1103/PhysRevB.102.220411

9. J. Thien, J. Bahlmann, A. Alexander, M. Hoppe, T.Pohlmann, **K. Ruwisch**, C. Meyer, F. Bertram, and K. Kuepper and J. Wollschläger
"Effects of Post-deposition Annealing on Epitaxial CoO/Fe_3O_4 Bilayers on $SrTiO_3$(001) and Formation of Thin High-Quality Cobalt Ferrite-like Films"
J. Phys. Chem. C **124**(43), 23895 (2020);
doi:10.1021/acs.jpcc.0c05503

10. J. Rodewald, J. Thien, **K. Ruwisch**, F. Bertram, K. Kuepper, and J. Wollschläger
"Enhanced magnetization of ultrathin $NiFe_2O_4$ films on $SrTiO_3$(001) related to cation disorder and anomalous strain"
Physical Review Materials **4**, 064404 (2020);
doi:10.1103/PhysRevMaterials.4.064404

11. P. Thakur, V. Sharma, R. Sharma, J. Wollschläger, **K. Ruwisch**, A. Dashan, S. Thakur, P. Sharma
"Transformation in the structural and optical properties with the phase change from hematite (Fe_2O_3) to pure spinel structure in Mn-Zn nanoferrites)"
Physica B: Condensed Matter **584**, 412107 (2020);
doi:10.1016/j.physb.2020.412107

12. O. Kuschel, N. Pathé, T. Schemme, **K. Ruwisch**, J. Rodewald, R. Buß, F. Bertram, T. Kuschel, K. Kuepper, and J. Wollschläger
"Impact of strain and morphology on magnetic properties of Fe_3O_4/NiO bilayers grown on Nb:$SrTiO_3$(001) and MgO(001)"
Materials **11**, 1122 (2018);
doi:10.3390/ma11071122

Literature

[1] A. Hirohata, K. Yamada, Y. Nakatani, I.-L. Prejbeanu, B. Diény, P. Pirro and B. Hillebrands. "Review on spintronics: Principles and device applications". *Journal of Magnetism and Magnetic Materials*, 509, 166711, 2020. ISSN 0304-8853. doi:https://doi.org/10.1016/j.jmmm.2020.166711.

[2] B. Dieny, P. Gambardella and et al. "Opportunities and challenges for spintronics in the microelectronics industry". *Nature Electronics*, 3(8), 446 – 459, 2020. ISSN 2520-1131. doi:10.1038/s41928-020-0461-5.

[3] E. E. Fullerton and J. R. Childress. "Spintronics, Magnetoresistive Heads, and the Emergence of the Digital World". *Proceedings of the IEEE*, 104(10), 1787–1795, 2016. doi:10.1109/JPROC.2016.2567778.

[4] M. Pinarbasi and A. D. Kent. "Perspectives on spintronics technology development: Giant magnetoresistance to spin transfer torque magnetic random access memory". *APL Materials*, 10(2), 020901, 2022. doi:10.1063/5.0075945.

[5] M. N. Baibich, J. M. Broto, A. Fert, F. N. Van Dau, F. Petroff, P. Etienne, G. Creuzet, A. Friederich and J. Chazelas. "Giant Magnetoresistance of (001)Fe/(001)Cr Magnetic Superlattices". *Phys. Rev. Lett.*, 61, 2472–2475, 1988. doi:10.1103/PhysRevLett.61.2472.

[6] G. Binasch, P. Grünberg, F. Saurenbach and W. Zinn. "Enhanced magnetoresistance in layered magnetic structures with antiferromagnetic interlayer exchange". *Phys. Rev. B*, 39, 4828–4830, 1989. doi:10.1103/PhysRevB.39.4828.

[7] C. Chappert, A. Fert and F. N. Van Dau. "The emergence of spin electronics in data storage". *Nature Materials*, 6, 813–823, 2007.

[8] M. Julliere. "Tunneling between ferromagnetic films". *Physics Letters A*, 54(3), 225–226, 1975. ISSN 0375-9601. doi:https://doi.org/10.1016/0375-9601(75)90174-7.

[9] J. S. Moodera, L. R. Kinder, T. M. Wong and R. Meservey. "Large Magnetoresistance at Room Temperature in Ferromagnetic Thin Film Tunnel Junctions". *Phys. Rev. Lett.*, 74, 3273–3276, 1995. doi:10.1103/PhysRevLett.74.3273.

[10] T. Miyazaki and N. Tezuka. "Spin polarized tunneling in ferromagnet/insulator/ferromagnet junctions". *Journal of Magnetism and Magnetic Materials*, 151(3), 403–410, 1995. ISSN 0304-8853. doi:https://doi.org/10.1016/0304-8853(95)00563-3. Spin Polarized Electron Transport.

[11] Z. Zhang and S. Satpathy. "Electron states, magnetism, and the Verwey transition in magnetite". *Phys. Rev. B*, 44, 13319–13331, 1991. doi:10.1103/PhysRevB.44.13319.

[12] P. van der Zaag, P. Bloemen, J. Gaines, R. Wolf, P. van der Heijden, R. van de Veerdonk and W. de Jonge. "On the construction of an Fe3O4-based all-oxide spin valve". *Journal of Magnetism and Magnetic Materials*, 211(1), 301–308, 2000. ISSN 0304-8853. doi:https://doi.org/10.1016/S0304-8853(99)00751-9.

[13] F. Greullet, E. Snoeck, C. Tiusan, M. Hehn, D. Lacour, O. Lenoble, C. Magen and L. Calmels. "Large inverse magnetoresistance in fully epitaxial Fe/Fe3O4/MgO/Co magnetic tunnel junctions". *Applied Physics Letters*, 92(5), 053508, 2008. doi:10.1063/1.2841812.

[14] X. W. Li, A. Gupta, G. Xiao, W. Qian and V. P. Dravid. "Fabrication and properties of heteroepitaxial magnetite (Fe3O4) tunnel junctions". *Applied Physics Letters*, 73(22), 3282–3284, 1998. doi:10.1063/1.122745.

[15] R. Bliem, E. McDermott, P. Ferstl, M. Setvin, O. Gamba, J. Pavelec, M. A. Schneider, M. Schmid, U. Diebold, P. Blaha, L. Hammer and G. S. Parkinson. "Subsurface cation vacancy stabilization of the magnetite(001) surface". *Science*, 346, 1215, 2014. doi:10.1126/science.1260556.

[16] G. S. Parkinson, U. Diebold, J. Tang and L. Malkinski. "Tailoring the Interface Properties of Magnetite for Spintronics". In L. Malkinski (Editor), "Advanced Magnetic Materials", chapter 3. IntechOpen, Rijeka, 2012. doi:10.5772/39101.

[17] Y. Shen, D. Kan, I. Lin, M.-W. Chu, I. Suzuki and Y. Shimakawa. "Perpendicular magnetic tunnel junctions based on half-metallic NiCo2O4". *Applied Physics Letters*, 117, 042408, 2020.

[18] X. Chen, Q. Wu, L. Zhang, Y. Hao, M.-G. Han, Y. Zhu and X. Hong. "Anomalous Hall effect and perpendicular magnetic anisotropy in ultrathin ferrimagnetic NiCo2O4 films". *Applied Physics Letters*, 120(24), 242401, 2022. doi:10.1063/5.0097869.

[19] J. S. Moodera, X. Hao, G. A. Gibson and R. Meservey. "Electron-Spin Polarization in Tunnel Junctions in Zero Applied Field with Ferromagnetic EuS Barriers". *Phys. Rev. Lett.*, 61, 637–640, 1988. doi:10.1103/PhysRevLett.61.637.

[20] B. B. Nelson-Cheeseman, A. B. Shah, T. S. Santos, S. D. Bader, J.-M. Zuo and A. Bhattacharya. "Cation-ordering effects in the single layered manganite La2/3Sr4/3MnO4". *Appl. Phys. Lett.*, 98(7), 072505, 2011. doi:10.1063/1.3554387.

[21] J. V. Ahlburg, C. Granados-Miralles, F. H. Gjørup, H. L. Andersen and M. Christensen. "Exploring the direct synthesis of exchange-spring nanocomposites by reduction of CoFe2O4 spinel nanoparticles using in situ neutron diffraction". *Nanoscale*, 12, 9440–9451, 2020. doi:10.1039/D0NR00912A.

[22] E. Negusse and C. M. Williams. "Magnetically Induced Enhanced Exchange Spring Effect in $CoFe_2O_4/CoFe_2/CoFe_2O_4$ Films". *IEEE Trans. Magn.*, 56(7), 7516705, 2020. doi:10.1109/TMAG.2019.2961989.

[23] T. Kado. "Large room-temperature inverse magnetoresistance in tunnel junctions with a Fe_3O_4 electrode". *Appl. Phys. Lett.*, 92, 092502, 2008. doi:10.1063/1.2890852.

[24] J.-B. Moussy. "From epitaxial growth of ferrite thin films to spin-polarized tunnelling". *J. Phys. D: Appl. Phys.*, 46(14), 143001, 2013. doi:10.1088/0022-3727/46/14/143001.

[25] L. Marnitz, K. Rott, S. Niehörster, C. Klewe, D. Meier, S. Fabretti, M. Witziok, A. Krampf, O. Kuschel, T. Schemme, K. Kuepper, J. Wollschläger, A. Thomas, G. Reiss and T. Kuschel. "Sign change in the tunnel magnetoresistance of Fe3O4/MgO/Co-Fe-B magnetic tunnel junctions depending on the annealing temperature and the interface treatment". *AIP Adv.*, 5, 047103, 2015. doi:10.1063/1.4917018.

[26] Y. Zhang, Q. Zhou, J. Ding, Z. Yang, B. Zhu, X. Yang, S. Chen and J. Ou-Yang. "Electric field control of exchange-spring behavior". *Journal of Applied Physics*, 117(12), 124105, 2015. doi:10.1063/1.4916242.

[27] K. Ruwisch, T. Pohlmann, M. Hoppe, F. Bertram, P. Shafer, J. Wollschläger and K. Küpper. "Inferface Magnetization Phenomena in Epitaxial Thin Fe3O4/CoxFe3–xO4 Bilayers". *The Journal of Physical Chemistry C*, 125(42), 23327–23337, 2021. doi:10.1021/acs.jpcc.1c05274.

[28] K. Ruwisch, T. Pohlmann, F. Bertram, C. Schlüter, A. Gloskovskii, K. Küpper and J. Wollschläger. "Real-Time Monitoring the Growth of Epitaxial $Co_xFe_{3-x}O_4$ Ultrathin Films

on Nb-Doped $SrTiO_3$(001) via Reactive Molecular Beam Epitaxy by Means of Operando HAXPES". *Materials*, 15(7), 2022. ISSN 1996-1944. doi:10.3390/ma15072377.

[29] K. Ruwisch, A. Alexander, T. Pollenske, K. Küpper and J. Wollschläger. "Influence of Oxygen Plasma on the Growth and Stability of Epitaxial NiCo2O4 Ultrathin Films on Various Substrates". *Materials*, 15(19), 2022. ISSN 1996-1944. doi:10.3390/ma15196911.

[30] O. Kuschel. *From initial growth of ultrathin* Fe_3O_4 *films up to* $NiFe_2O_4$ *formation through interdiffusion of* Fe_3O_4/NiO *bilayers on Nb:*$SrTiO_3$*(001)*. Ph.D. thesis, Osnabrück University, 2020.

[31] R. Gross and A. Marx. *Festkörperphysik*. Oldenbourg Verlag, 2014.

[32] W. Demtröder. *Experimentalphysik 2*. Springer-Verlag Berlin Heidelberg, 2013. doi:10.1007/978-3-642-29944-5.

[33] K. Oura, V. Lifshits, A. Saranin, A. Zotov and M. Katayama. *Surface Science - An Introduction*. Springer-Verlag Berlin Heidelberg New York, 2003.

[34] S. Hashimoto, J.-L. Peng, W. M. Gibson, L. J. Schowalter and R. W. Fathauer. "Strain measurement of epitaxial CaF2 on Si(111) by MeV ion channeling". *Applied Physics Letters*, 47(10), 1071–1073, 1985. doi:10.1063/1.96383.

[35] J. Matthews and A. Blakeslee. "Defects in epitaxial multilayers: I. Misfit dislocations". *Journal of Crystal Growth*, 27, 118–125, 1974. ISSN 0022-0248. doi:https://doi.org/10.1016/S0022-0248(74)80055-2.

[36] N. W. Ashcroft and D. N. Mermin. *Festkörperphysik*. Oldenburg Wissenschaftsverlag GmbH, 4 edition, 2013.

[37] C. Kittel. *Einführung in die Festkörperphysik*. Oldenbourg, 2006. ISBN 9783486577235.

[38] K. N. Tu, J. W. Mayer and L. C. Feldman. *Electronic Thin Film Science: For Electrical Engineers and Materials Scientists*. Macmillan Publishing Company, New York, 1992.

[39] W. Friedrich, P. Knipping and M. Laue. "Interferenzerscheinungen bei Röntgenstrahlen". *Annalen der Physik*, 346(10), 971–988, 1913. doi:https://doi.org/10.1002/andp.19133461004.

[40] J. Rodewald. *Advancement of growth and characteristics of ultrathin ferrite films*. Ph.D. thesis, Osnabrück University, 2020.

[41] J. D. Jackson. *Classical Electrodynamics*. John Wiley & Sons, Inc., New York, 2 edition, 1975.

[42] R. W. James. *The Crystalline State - Vol II*, chapter The Optical Principles of the Diffraction of X-rays. G. Bell and Sons Ltd., London, 1962.

[43] B. E. Warren. *X-ray diffraction*. Dover Publications, Inc., New York, 1990.

[44] I. K. Robinson and D. J. Tweet. "Surface X-ray diffraction". *Reports on Progress in Physics*, 55(5), 599, 1992. doi:10.1088/0034-4885/55/5/002.

[45] *International tables for x-ray crystallography*. ynoch Press for the International Union of Crystallography, Birmingham, 1952-1974.

[46] P. Scherrer. "Bestimmung der Größe und der inneren Struktur von Kolloidteilchen mittels Röntgenstrahlen". *Nachrichten von der Gesellschaft der Wissenschaften zu Göttingen, Mathematisch-Physikalische Klasse*, 1918, 98–100, 1918.

[47] F. Bertram. *The structure of ultrathin iron oxide films studied by x-ray diffraction*. Ph.D. thesis, Osnabrück University, 2012.

[48] C. Deiter. *Röntgenstrukturanalyse von Halbleiter-Isolator-Schichtsystemen*. Ph.D. thesis, Bremen University, 2005.

[49] R. Feidenhans'l. "Surface structure determination by X-ray diffraction". *Surface Science Reports*, 10(3), 105–188, 1989. ISSN 0167-5729. doi:https://doi.org/10.1016/0167-5729(89)90002-2.

[50] I. K. Robinson. "Crystal truncation rods and surface roughness". *Phys. Rev. B*, 33, 3830–3836, 1986. doi:10.1103/PhysRevB.33.3830.

[51] S. Macke and E. Goering. "Magnetic reflectometry of heterostructures". *Journal of Physics: Condensed Matter*, 26(36), 363201, 2014. doi:10.1088/0953-8984/26/36/363201.

[52] M. Tolan. *X-ray scattering from soft-matter thin films. Materials science and basic research.* Springer-Verlag, Berlin, Heidelberg, 1999. doi:10.1007/BFb0112834.

[53] J. Als-Nielsen and D. McCorrow. *Elements of Modern X-ray Physics.* John Wiley & Sons Ltd, 2011. ISBN 9781119998365. doi:10.1002/9781119998365.

[54] L. G. Parratt. "Surface studies of solids by total reflection of x-rays". *Rev. Mod. Phys.*, 95, 359, 1954. doi:10.1103/PhysRev.95.359.

[55] F. Bertram. *Röntgenreflektometrie an ultradünnen Schichten.* Bachelor's thesis, Osnabrück University, 2007.

[56] L. Névot and P. Croce. "Caractérisation des surfaces par réflexion rasante de rayons X. Application à l'étude du polissage de quelques verres silicates". *Rev. Phys. Appl.*, 15, 761, 1980. doi:10.1051/rphysap:01980001503076100.

[57] L. Spieß, G. Teichert, R. Schwarzer, H. Behnken and C. Genzel. *Moderne Röntgenbeugung - Röntgendiffraktometrie für Materialwissenschaftler, Physiker und Chemiker.* Springer Spektrum Wiesbaden, 3 edition, 2019. doi:10.1007/978-3-8348-8232-5.

[58] J. C. Vickerman and I. S. Gilmore. *Surface Analysis: The Principal Techniques.* John Wiley & Sons Ltd, 2 edition, 2009.

[59] H. Hertz. "Ueber einen Einfluss des ultravioletten Lichtes auf die electrische Entladung". *Annalen der Physik*, 267(8), 983–1000, 1887. doi:https://doi.org/10.1002/andp.18872670827.

[60] A. Einstein. "Über einen die Erzeugung und Verwandlung des Lichtes betreffenden heuristischen Gesichtspunkt". *Ann. Phys.*, 322(6), 132–148, 1905. doi:10.1002/andp.19053220607.

[61] V. I. Nefedov. *X-ray photoelectron spectroscopy of solid surfaces.* VSP, 1988.

[62] T. Koopmans. "Über die Zuordnung von Wellenfunktionen und Eigenwerten zu den Einzelnen Elektronen Eines Atoms". *Physica*, 1(1), 104–113, 1934. ISSN 0031-8914. doi:https://doi.org/10.1016/S0031-8914(34)90011-2.

[63] D. A. Shirley. "High-Resolution X-Ray Photoemission Spectrum of the Valence Bands of Gold". *Phys. Rev. B*, 5, 4709–4714, 1972. doi:10.1103/PhysRevB.5.4709.

[64] P. J. Cumpson and M. P. Seah. "Elastic scattering corrections in AES and XPS. II. Estimating attenuation lengths and conditions required for their valid use in overlayer/substrate experiments". *Surf. Interface Anal.*, 25, 430, 1997. doi:10.1002/(SICI)1096-9918(199706)25:6<430::AID-SIA254>3.0.CO;2-7.

[65] D. Briggs and M. P. Seah (Editors). *Practical surface anlysis.* John Wiley & Sons, Hoboken, 1990.

[66] S. Tanuma, C. J. Powell and D. R. Penn. "Calculation of electron inelastic mean free paths (IMFPs) VII. Reliability of the TPP-2M IMFP predictive equation". *Surf. Interface Anal.*, 35, 268–275, 2003. doi:10.1002/sia.1526.

[67] J. W. Cooper and S. T. Manson. "Photo-Ionization in the Soft X-Ray Range: Angular Distributions of Photoelectrons and Interpretation in Terms of Subshell Structure". *Phys. Rev.*, 177, 157–163, 1969. doi:10.1103/PhysRev.177.157.

[68] J. Cooper and R. N. Zare. "Angular Distribution of Photoelectrons". *The Journal of Chemical Physics*, 48(2), 942–943, 1968. doi:10.1063/1.1668742.

[69] J. H. Scofield. "Hartree-Slater subshell photoionization cross-sections at 1254 and 1487 eV". *Journal of Electron Spectroscopy and Related Phenomena*, 8, 129, 1976. doi:10.1016/0368-2048(76)80015-1.

[70] J. H. Scofield. "Angular distribution of photoelectrons from polarized X-rays". *Physica Scripta*, 41(1), 59, 1990. doi:10.1088/0031-8949/41/1/015.

[71] J. W. Cooper. "Photoelectron-angular-distribution parameters for rare-gas subshells". *Phys. Rev. A*, 47, 1841, 1993. doi:10.1103/PhysRevA.47.1841.

[72] M. B. Trzhaskovskaya, V. I. Nefedov and V. G. Yarzhemsky. "Photoelectron angular distribution parameters for elements Z=1 to Z=54 in the photoelectron energy range 100-5000 eV". *At. Data Nucl. Data Tables*, 77(1), 97–159, 2001. doi:10.1006/adnd.2000.0849.

[73] M. B. Trzhaskovskaya, V. K. Nikulin, V. I. Nefedov and V. G. Yarzhemsky. "Non-dipole second order parameters of the photoelectron angular distribution for elements $Z = 1$–100 in the photoelectron energy range 1–10 keV". *At. Data Nucl. Data Tables*, 92, 245, 2006. doi:10.1016/j.adt.2005.12.002.

[74] S. Eisebitt, T. Böske, J.-E. Rubensson and W. Eberhardt. "Determination of absorption coefficients for concentrated samples by fluorescence detection". *Phys. Rev. B*, 47, 14103–14109, 1993. doi:10.1103/PhysRevB.47.14103.

[75] Z. Tan, J. I. Budnick and S. M. Heald. "Structural parameter determination in fluorescence EXAFS of concentrated samples". *Review of Scientific Instruments*, 60(6), 1021–1025, 1989. doi:10.1063/1.1140311.

[76] T. Pohlmann. *Structural and magnetic properties of ultrathin Fe_3O_4 films: cation- and latticesite-selective studies by synchrotron radiation based techniques*. Ph.D. thesis, Osnabrück University, 2021.

[77] F. De Groot and A. Kotani. *Core Level Spectroscopy of Solids*. Advances in Condensed Matter Science. Taylor & Francis Group, 2008. doi:10.1201/9781420008425.

[78] J. L. Erskine and E. A. Stern. "Calculation of the M_{23} magneto-optical absorption spectrum of ferromagnetic nickel". *Phys. Rev. B*, 12, 5016–5024, 1975. doi:10.1103/PhysRevB.12.5016.

[79] G. Schütz, P. Fischer, E. Goering, K. Attenkofer, D. Ahlers and W. Rößl. "X-ray magnetic circular dichroism". *Synchrotron Radiation News*, 10(4), 13–26, 1997. doi:10.1080/08940889708260897.

[80] J. Stöhr and Y. Wu. *X-Ray Magnetic Circular Dichroism: Basic Concepts and Theory for 3D Transition Metal Atoms*, pages 221–250. Springer Netherlands, Dordrecht, 1994. ISBN 978-94-011-0868-3. doi:10.1007/978-94-011-0868-3_9.

[81] U. Fano. "Spin Orientation of Photoelectrons Ejected by Circularly Polarized Light". *Phys. Rev.*, 178, 131–136, 1969. doi:10.1103/PhysRev.178.131.

[82] U. Fano. "Spin Orientation of Photoelectrons: Erratum and Addendum". *Phys. Rev.*, 184, 250–251, 1969. doi:10.1103/PhysRev.184.250.

[83] J. Stöhr and H. C. Siegmann. *Magnetism*. Springer Berlin, Heidelberg, 2006.

[84] B. T. Thole, P. Carra, F. Sette and G. van der Laan. "X-ray circular dichroism as a probe of orbital magnetization". *Phys. Rev. Lett.*, 68, 1943–1946, 1992. doi:10.1103/PhysRevLett.68.1943.

[85] P. Carra, B. T. Thole, M. Altarelli and X. Wang. "X-ray circular dichroism and local magnetic fields". *Phys. Rev. Lett.*, 70, 694–697, 1993. doi:10.1103/PhysRevLett.70.694.

[86] C. T. Chen, Y. U. Idzerda, H.-J. Lin, N. V. Smith, G. Meigs, E. Chaban, G. H. Ho, E. Pellegrin and F. Sette. "Experimental Confirmation of the X-Ray Magnetic Circular Dichroism Sum Rules for Iron and Cobalt". *Phys. Rev. Lett.*, 75(152), 1995. doi:10.1103/PhysRevLett.75.152.

[87] K. Ruwisch. *Charakterisierung des Exchange Bias-Systems* Fe_3O_4/CoO *mit SQUID und VSM*. Master's thesis, Osnabrück University, 2018.

[88] S. Hunklinger. *Festkörperphysik*. De Gruyter Studium. De Gruyter, 2014. ISBN 9783486989687.

[89] T. Kuschel. *Magnetic anisotropy of transition metal based thin films investigated by magnetooptic Kerr effect*. Ph.D. thesis, Osnabrück University, 2011.

[90] D. Ginacoli. *Physik*. Pearson Studium, 2010.

[91] H. Kuchling. *Taschenbuch der Physik*. Carl Hanser Verlag GmbH & Co. KG, 2011.

[92] J. C. Maxwell. "VIII. A dynamical theory of the electromagnetic field". *Philosophical Transactions of the Royal Society of London*, 155, 459–512, 1865. doi:10.1098/rstl.1865.0008.

[93] J. Hubbard and B. H. Flowers. "Electron correlations in narrow energy bands". *Proceedings of the Royal Society of London. Series A. Mathematical and Physical Sciences*, 276(1365), 238–257, 1963. doi:10.1098/rspa.1963.0204.

[94] W. Heisenberg. "Zur Theorie des Ferromagnetismus". *Zeitschrift für Physik*, 49, 619–636, 1928. doi:10.1007/BF01328601.

[95] C. Zener. "Interaction between the *d*-Shells in the Transition Metals. II. Ferromagnetic Compounds of Manganese with Perovskite Structure". *Phys. Rev.*, 82, 403–405, 1951. doi:10.1103/PhysRev.82.403.

[96] H. Kramers. "L'interaction Entre les Atomes Magnétogènes dans un Cristal Paramagnétique". *Physica*, 1(1), 182–192, 1934. ISSN 0031-8914. doi:https://doi.org/10.1016/S0031-8914(34)90023-9.

[97] P. W. Anderson. "Antiferromagnetism. Theory of Superexchange Interaction". *Phys. Rev.*, 79, 350–356, 1950. doi:10.1103/PhysRev.79.350.

[98] S. Blundell. *Magnetism in Condensed Matter*. Oxford University Press, Oxford, 2001.

[99] J. Clarke and A. I. Braginski (Editors). *The SQUID Handbook: Fundamentals and Technology of SQUIDs and SQUID systems*, volume 1. John Wiley & Sons, Ltd, 2004. doi:10.1002/3527603646.

[100] F. London. *Superfluids*, volume 1. Wiley, New York, 1950.

[101] B. Josephson. "Possible new effects in superconductive tunnelling". *Physics Letters*, 1(7), 251–253, 1962. ISSN 0031-9163. doi:https://doi.org/10.1016/0031-9163(62)91369-0.

[102] H. Onnes. *Akad. van Wetenschappen (Amsterdam)*, 14(113), 818, 1911.

[103] W. Meissner and R. Ochsenfeld. "Ein neuer Effekt bei Eintritt der Supraleitfähigkeit". *Naturwissenschaften*, 21, 787–788, 1933. doi:10.1007/BF01504252.

[104] R. Doll and M. Näbauer. "Experimental Proof of Magnetic Flux Quantization in a Superconducting Ring". *Physical Review Letters*, 7(2), 51–52, 1961.

[105] J. B. S. Deaver and W. M. Fairbank. "Experimental Evidence for Quantized Flux in Superconducting Cylinders". *Physical Review Letters*, 7(2), 43–46, 1961.

[106] L. N. Cooper. "Bound Electron Pairs in a Degenerate Fermi Gas". *Phys. Rev.*, 104, 1189–1190, 1956. doi:10.1103/PhysRev.104.1189.

[107] J. Bardeen, L. N. Cooper and J. R. Schrieffer. "Theory of Superconductivity". *Phys. Rev.*, 108, 1175–1204, 1957. doi:10.1103/PhysRev.108.1175.

[108] V. J. Katz. "The History of Stokes' Theorem". *Mathematics Magazine*, 52(3), 146–156, 1979. doi:10.1080/0025570X.1979.11976770.

[109] R. Huebener. *Leiter, Halbleiter, Supraleiter - Eine kompakte Einführung in die Geschichte, Entwicklung und Theorie der Festkörperphysik*. Springer Spektrum, 2017.

[110] J. Thien. *From Magnetite to Cobalt Ferrite Thin Films: New Perspectives for the Growth of Thin Ferrite Films for their Application in Spintronics*. Ph.D. thesis, Osnabrück University, 2022.

[111] M. Bass (Editor). *Handbook of Optics: Devices, measurements, and properties*, volume 2. McGraw-Hill, Inc., 1995.

[112] D. M. Roessler and W. C. Walker. "Electronic spectrum and ultraviolet optical properties of crystalline MgO". *Phys. Rev.*, 159, 733, 1967. doi:10.1103/PhysRev.159.733.

[113] J. M. D. Coey, M. Venkatesan and P. Stamenov. "Surface magnetism of strontium titanate". *Journal of Physics: Condensed Matter*, 28(48), 485001, 2016. doi:10.1088/0953-8984/28/48/485001.

[114] T. Majdi, G.-z. Zhu, J. Carvalho, V. Jarvis, K. Meinander, J. F. Britten, G. Botton and J. S. Preston. "Evidence for an equilibrium epitaxial complexion at the Au-$MgAl_2O_4$ interface". *Applied Physics Letters*, 107(24), 241601, 2015. doi:10.1063/1.4937430.

[115] S. M. Hosseini. "Structural, electronic and optical properties of spinel $MgAl_2O_4$ oxide". *physica status solidi (b)*, 245(12), 2800–2807, 2008. doi:https://doi.org/10.1002/pssb.200844142.

[116] R. Cornell and U. Schwertmann. *The Iron Oxides: Structure, Properties, Reactions, Occurences and Uses*. Wiley-VCH GmbH & Co. KGaA, 2003.

[117] M. Ziese, R. Hohne, K. Zimmer and P. Esquinazi. "Step edge magnetoresistance of magnetite films". In "2002 IEEE International Magnetics Conference (INTERMAG)", pages EE2–. 2002. doi:10.1109/INTMAG.2002.1001143.

[118] Z. Li, E. S. Fisher, J. Z. Liu and M. V. Nevitt. "Single-crystal elastic constants of Co-Al and Co-Fe spinels". *J. Mater. Sci.*, 26(10), 2621–2624, 1991. ISSN 1573-4803. doi:10.1007/BF00545546.

[119] J. Marco, J. Gancedo, M. Gracia, J. Gautier, E. Ríos and F. Berry. "Characterization of the Nickel Cobaltite, NiCo2O4, Prepared by Several Methods: An XRD, XANES, EXAFS, and XPS Study". *Journal of Solid State Chemistry*, 153(1), 74–81, 2000. ISSN 0022-4596. doi:https://doi.org/10.1006/jssc.2000.8749.

[120] A. Tsujie, Y. Hara, T. Yanase, T. Shimada and T. Nagahama. "NiCo2O4 films fabricated by reactive molecular beam epitaxy and annealing in various oxygen atmospheres". *Applied Physics Letters*, 116(23), 232404, 2020. doi:10.1063/5.0008677.

[121] Y. Shen, D. Kan, Z. Tan, Y. Wakabayashi and Y. Shimakawa. "Tuning of ferrimagnetism and perpendicular magnetic anisotropy in $NiCo_2O_4$ epitaxial films by the cation distribution". *Phys. Rev. B*, 101, 094412, 2020. doi:10.1103/PhysRevB.101.094412.

[122] Y. Bitla, Y.-Y. Chin, J.-C. Lin, C. N. Van, R. Liu, Y. Zhu, H.-J. Liu, Q. Zhan, H.-J. Lin, C.-T. Chen et al. "Origin of metallic behavior in NiCo2O4 ferrimagnet". *Scientific reports*, 5(1), 1–8, 2015. doi:10.1038/srep15201.

[123] P. Silwal, L. Miao, I. Stern, X. Zhou, J. Hu and D. Ho Kim. "Metal insulator transition with ferrimagnetic order in epitaxial thin films of spinel NiCo2O4". *Applied Physics Letters*, 100(3), 032102, 2012. doi:10.1063/1.3676439.

[124] S. Holgersson and A. Karlsson. "Über einige neue Kobaltite vom Spinelltypus". *Zeitschrift für anorganische und allgemeine Chemie*, 183(1), 384–394, 1929.

[125] K. Zhang, C. Zhen, W. Wei, W. Guo, G. Tang, L. Ma, D. Hou and X. Wu. "Insight into metallic behavior in epitaxial half-metallic NiCo2O4 films". *RSC Adv.*, 7, 36026–36033, 2017. doi:10.1039/C7RA03136J.

[126] D. Kan, M. Mizumaki, M. Kitamura, Y. Kotani, Y. Shen, I. Suzuki, K. Horiba and Y. Shimakawa. "Spin and orbital magnetic moments in perpendicularly magnetized $Ni_{1-x}Co_{2+y}O_{4-z}$ epitaxial thin films: Effects of site-dependent cation valence states". *Phys. Rev. B*, 101, 224434, 2020. doi:10.1103/PhysRevB.101.224434.

[127] D. T. Margulies, F. T. Parker, M. L. Rudee, F. E. Spada, J. N. Chapman, P. R. Aitchison and A. E. Berkowitz. "Origin of the Anomalous Magnetic Behavior in Single Crystal Fe_3O_4 Films". *Phys. Rev. Lett.*, 79, 5162–5165, 1997. doi:10.1103/PhysRevLett.79.5162.

[128] F. C. Voogt, T. T. M. Palstra, L. Niesen, O. C. Rogojanu, M. A. James and T. Hibma. "Superparamagnetic behavior of structural domains in epitaxial ultrathin magnetite films". *Phys. Rev. B*, 57, R8107–R8110, 1998. doi:10.1103/PhysRevB.57.R8107.

[129] T. Hibma, F. C. Voogt, L. Niesen, P. A. A. van der Heijden, W. J. M. de Jonge, J. J. T. M. Donkers and P. J. van der Zaag. "Anti-phase domains and magnetism in epitaxial magnetite layers". *Journal of Applied Physics*, 85(8), 5291–5293, 1999. doi:10.1063/1.369857.

[130] W. Eerenstein, T. T. M. Palstra, T. Hibma and S. Celotto. "Origin of the increased resistivity in epitaxial Fe_3O_4 films". *Phys. Rev. B*, 66, 201101, 2002. doi:10.1103/PhysRevB.66.201101.

[131] C. Zhen, X. Zhang, W. Wei, W. Guo, A. Pant, X. Xu, J. Shen, L. Ma and D. Hou. "Nanostructural origin of semiconductivity and large magnetoresistance in epitaxial NiCo2O4/Al2O3 thin films". *Journal of Physics D: Applied Physics*, 51(14), 145308, 2018. doi:10.1088/1361-6463/aab2a3.

[132] P. Li, C. Xia, D. Zheng, P. Wang, C. Jin and H. Bai. "Observation of large low-field magnetoresistance in spinel cobaltite: A new half-metal". *physica status solidi (RRL) – Rapid Research Letters*, 10(2), 190–196, 2016. doi:10.1002/pssr.201510402.

[133] R. J. M. van de Veerdonk, M. A. M. Gijs, P. A. A. van der Heijden, R. M. Wolf and W. J. M. de Jonge. "Study of the Verwey Transition of Fe3O4 Films and Fe3O4/MgO Multilayers Grown by Mbe". *MRS Online Proceedings Library*, 401, 455–460, 1995. doi:10.1557/PROC-401-455.

[134] J.-B. Moussy, S. Gota, A. Bataille, M.-J. Guittet, M. Gautier-Soyer, F. Delille, B. Dieny, F. Ott, T. D. Doan, P. Warin, P. Bayle-Guillemaud, C. Gatel and E. Snoeck. "Thickness dependence of anomalous magnetic behavior in epitaxial Fe_3O_4(111) thin films: Effect of density of antiphase boundaries". *Phys. Rev. B*, 70, 174448, 2004. doi:10.1103/PhysRevB.70.174448.

[135] G. J. Strijkers, J. T. Kohlhepp, P. A. A. van der Heijden, H. J. M. Swagten, W. J. M. de Jonge and J. M. Gaines. "Magnetization of Fe3O4/MgO multilayers studied with Mössbauer spectroscopy". *Journal of Applied Physics*, 85(8), 5294–5296, 1999. doi:10.1063/1.369858.

[136] J. D. Wei, I. Knittel, U. Hartmann, Y. Zhou, S. Murphy, I. V. Shvets and F. T. Parker. "Influence of the antiphase domain distribution on the magnetic structure of magnetite thin films". *Applied Physics Letters*, 89(12), 122517, 2006. doi:10.1063/1.2356308.

[137] P. van der Heijden, P. Bloemen, J. Gaines, J. van Eemeren, R. Wolf, P. van der Zaag and W. de Jonge. "Magnetic interface anisotropy of MBE-grown ultra-thin (001) Fe3O4 layers". *Journal of Magnetism and Magnetic Materials*, 159(3), L293–L298, 1996. ISSN 0304-8853. doi:https://doi.org/10.1016/0304-8853(96)00376-9.

[138] K. Balakrishnan, S. K. Arora and I. V. Shvets. "Strain relaxation studies of the Fe3O4/MgO (100) heteroepitaxial system grown by magnetron sputtering". *J. Phys.: Condens. Matter*, 16(30), 5387–5393, 2004. doi:10.1088/0953-8984/16/30/001.

[139] S. K. Arora, R. G. S. Sofin, I. V. Shvets and M. Luysberg. "Anomalous strain relaxation behavior of Fe3O4/MgO (100) heteroepitaxial system grown using molecular beam epitaxy". *Journal of Applied Physics*, 100(7), 073908, 2006. doi:10.1063/1.2349468.

[140] S. Speller, W. Heiland and M. Schleberger. "Chapter 1 - SURFACE CHARACTERIZATION: COMPOSITION, STRUCTURE AND TOPOGRAPHY". In H. S. Nalwa (Editor), "Handbook of Surfaces and Interfaces of Materials", pages 1–53. Academic Press, Burlington, 2001. ISBN 978-0-12-513910-6. doi:10.1016/B978-012513910-6/50020-7.

[141] H. Lüth. *Solid Surfaces, Interfaces and Thin Films*. Springer Berlin, Heidelberg, 5 edition, 2010. doi:10.1007/978-3-642-13592-7.

[142] S. Hüfner. *Photoelectron Spectroscopy*. Springer Berlin, Heidelberg, 3 edition, 2003. doi:10.1007/978-3-662-09280-4.

[143] K. Wille. *Physik der Teilchenbeschleuniger und Synchrotronstrahlungsquellen*. Vieweg+Teubner Verlag Wiesbaden, 2 edition, 1996. doi:10.1007/978-3-663-11039-2.

[144] J. Cibert, J.-F. Bobo and U. Lüders. "Development of new materials for spintronics". *Comptes Rendus Physique*, 6(9), 977–996, 2005. ISSN 1631-0705. doi:https://doi.org/10.1016/j.crhy.2005.10.008. Spintronics.

[145] A. Hoffmann and S. D. Bader. "Opportunities at the Frontiers of Spintronics". *Phys. Rev. Applied*, 4, 047001, 2015. doi:10.1103/PhysRevApplied.4.047001.

[146] G. Bauer, E. Saitoh and B. van Wees. "Spin caloritronics". *Nature Materials*, 11(5), 391–399, 2012. ISSN 1476-4660. doi:10.1038/NMAT3301.

[147] A. V. Ramos, M.-J. Guittet, J.-B. Moussy, R. Mattana, C. Deranlot, F. Petroff and C. Gatel. "Room temperature spin filtering in epitaxial cobalt-ferrite tunnel barriers". *Appl. Phys. Lett.*, 91(12), 122107, 2007. doi:10.1063/1.2787880.

[148] U. Lüders, A. Barthélémy, M. Bibes, K. Bouzehouane, S. Fusil, E. Jacquet, J.-P. Contour, J.-F. Bobo, J. Fontcuberta and A. Fert. "NiFe2O4: A Versatile Spinel Material Brings New Opportunities for Spintronics". *Advanced Materials*, 18(13), 1733–1736, 2006. doi:https://doi.org/10.1002/adma.200500972.

[149] S. Matzen, J.-B. Moussy, P. Wei, C. Gatel, J. C. Cezar, M. A. Arrio, P. Sainctavit and J. S. Moodera. "Structure, magnetic ordering, and spin filtering efficiency of NiFe2O4(111) ultrathin films". *Applied Physics Letters*, 104(18), 182404, 2014. doi:10.1063/1.4871733.

[150] S. Matzen, J.-B. Moussy, R. Mattana, K. Bouzehouane, C. Deranlot and F. Petroff. "Nanomagnetism of cobalt ferrite-based spin filters probed by spin-polarized tunneling". *Applied Physics Letters*, 101(4), 042409, 2012. doi:10.1063/1.4738790.

[151] J. M. Rebled, M. Foerster, S. Estradé, F. Rigato, C. Kanamadi, F. Sánchez, F. Peiró and J. Fontcuberta. "Ti diffusion in (001) SrTiO3–CoFe2O4 epitaxial heterostructures: blocking role of a MgAl2O4 buffer". *Phys. Chem. Chem. Phys.*, 15, 18274–18280, 2013. doi:10.1039/C3CP00001J.

[152] F. Rigato, J. Geshev, V. Skumryev and J. Fontcuberta. "The magnetization of epitaxial nanometric CoFe2O4(001) layers". *J. Appl. Phys.*, 106(11), 113924, 2009. doi:10.1063/1.3267873.

[153] F. Eskandari, S. B. Porter, M. Venkatesan, P. Kameli, K. Rode and J. M. D. Coey. "Magnetization and anisotropy of cobalt ferrite thin films". *Phys. Rev. Materials*, 1, 074413, 2017. doi:10.1103/PhysRevMaterials.1.074413.

[154] W. Betteridge. "The properties of metallic cobalt". *Prog. Mater. Sci.*, 24, 51–142, 1980. doi:https://doi.org/10.1016/0079-6425(79)90004-5.

[155] M. C. Biesinger, B. P. Payne, A. P. Grosvenor, L. W. Lau, A. R. Gerson and R. S. Smart. "Resolving surface chemical states in XPS analysis of first row transition metals, oxides and

hydroxides: Cr, Mn, Fe, Co and Ni". *Applied Surface Science*, 257(7), 2717–2730, 2011. ISSN 0169-4332. doi:https://doi.org/10.1016/j.apsusc.2010.10.051.

[156] J. Rodewald, J. Thien, T. Pohlmann, M. Hoppe, F. Timmer, F. Bertram, K. Kuepper and J. Wollschläger. "Formation of ultrathin cobalt ferrite films by interdiffusion of Fe_3O_4/CoO bilayers". *Phys. Rev. B*, 100(15), 155418, 2019. doi:10.1103/PhysRevB.100.155418.

[157] S. A. Chambers, R. F. C. Farrow, S. Maat, M. F. Toney, L. Folks, J. G. Catalano, T. P. Trainor and G. E. Brown Jr. "Molecular beam epitaxial growth and properties of $CoFe_2O_4$ on MgO(001)". *J. Magn. Magn. Mater.*, 246, 124–139, 2002. doi:10.1016/S0304-8853(02)00039-2.

[158] T. J. Chuang, C. R. Brundle and D. W. Rice. "Interpretation of the x-ray photoemission spectra of cobalt oxides and cobalt oxide surfaces". *Surf. Sci.*, 59, 413–429, 1976. doi:10.1016/0039-6028(76)90026-1.

[159] N. S. McIntyre and M. G. Cook. "X-ray photoelectron studies on some oxides and hydroxides of cobalt, nickel and copper". *Anal. Chem.*, 47(13), 2208–2213, 1975. doi:10.1021/ac60363a034.

[160] T. Nishizawa and K. Ishida. "The Co-Fe (Cobalt-Iron) system". *Bull. Alloy Phase Diagr.*, 5(250), 1984. doi:10.1007/BF02868548.

[161] J. Thien, J. Bahlmann, A. Alexander, M. Hoppe, T. Pohlmann, K. Ruwisch, C. Meyer, F. Bertram, K. Küpper and J. Wollschläger. "Effects of Post-deposition Annealing on Epitaxial CoO/Fe3O4 Bilayers on SrTiO3(001) and Formation of Thin High-Quality Cobalt Ferrite-like Films". *The Journal of Physical Chemistry C*, 124(43), 23895–23904, 2020. doi:10.1021/acs.jpcc.0c05503.

[162] P. F. Ndione, Y. Shi, V. Stevanovic, S. Lany, A. Zakutayev, P. A. Parilla, J. D. Perkins, J. J. Berry, D. S. Ginley and M. F. Toney. "Control of the Electrical Properties in Spinel Oxides by Manipulating the Cation Disorder". *Advanced Functional Materials*, 24(5), 610–618, 2014. doi:10.1002/adfm.201302535.

[163] O. Knop, K. I. G. Reid, Sutarno and Y. Nakagawa. "Chalkogenides of the transition elements. VI. X-Ray, neutron, and magnetic investigation of the spinels Co3O4, NiCo2O4, Co3S4, and NiCo2S4". *Canadian Journal of Chemistry*, 46(22), 3463–3476, 1968. doi:10.1139/v68-576.

[164] X. Chen, X. Zhang, M.-G. Han, L. Zhang, Y. Zhu, X. Xu and X. Hong. "Magnetotransport Anomaly in Room-Temperature Ferrimagnetic NiCo2O4 Thin Films". *Advanced Materials*, 31(4), 1805260, 2019. doi:10.1002/adma.201805260.

[165] P. Silwal, C. La-o vorakiat, E. E. M. Chia, D. H. Kim and D. Talbayev. "Effect of growth temperature on the terahertz-frequency conductivity of the epitaxial transparent conducting spinel NiCo2O4 films". *AIP Advances*, 3(9), 092116, 2013. doi:10.1063/1.4821548.

[166] X. Xu, C. Mellinger, Z. G. Cheng, X. Chen and X. Hong. "Epitaxial $NiCo_2O_4$ film as an emergent spintronic material: Magnetism and transport properties". *Journal of Applied Physics*, 132(2), 020901, 2022. doi:10.1063/5.0095326.

[167] P. Kang, G. Zhou, H. Ji, Z. Li, Z. Li and X. Xu. "Emergence of room-temperature perpendicular magnetic anisotropy in metallic $NiCo_2O_4$ thin film". *Journal of Magnetism and Magnetic Materials*, 553, 169293, 2022. ISSN 0304-8853. doi:https://doi.org/10.1016/j.jmmm.2022.169293.

[168] P. Silwal, L. Miao, J. Hu, L. Spinu, D. Ho Kim and D. Talbayev. "Thickness dependent structural, magnetic, and electronic properties of the epitaxial films of transparent conducting oxide NiCo2O4". *Journal of Applied Physics*, 114(10), 103704, 2013. doi:10.1063/1.4820930.

[169] C. Windisch, G. Exarhos, K. Ferris, M. Engelhard and D. Stewart. "Infrared transparent spinel films with p-type conductivity". *Thin Solid Films*, 398-399, 45–52, 2001. ISSN 0040-6090. doi:10.1016/S0040-6090(01)01302-5. Proceedings of the 28th International Conference on Metallurgic Coatings and Thin Films.

[170] D. P. Dubal, P. Gomez-Romero, B. R. Sankapal and R. Holze. "Nickel cobaltite as an emerging material for supercapacitors: An overview". *Nano Energy*, 11, 377–399, 2015. ISSN 2211-2855. doi:10.1016/j.nanoen.2014.11.013.

[171] R. K. Gupta, J. Candler, S. Palchoudhury, K. Ramasamy and B. K. Gupta. "Flexible and High Performance Supercapacitors Based on $NiCo_2O_4$ for Wide Temperature Range Applications". *Scientific Reports*, 5(1), 2015. ISSN 2045-2322. doi:10.1038/srep15265.

[172] W. Yang, Z. Gao, J. Ma, X. Zhang, J. Wang and J. Liu. "Hierarchical NiCo2O4@NiO core–shell hetero-structured nanowire arrays on carbon cloth for a high-performance flexible all-solid-state electrochemical capacitor". *J. Mater. Chem. A*, 2, 1448–1457, 2014. doi:10.1039/C3TA14488G.

[173] S. A. Khalid, C. Cao, L. Wang and Y. Zhu. "Microwave Assisted Synthesis of Porous NiCo2O4 Microspheres: Application as High Performance Asymmetric and Symmetric Supercapacitors with Large Areal Capacitance". *Scientific Reports*, 6, 22699, 2016. doi:10.1038/srep22699.

[174] F.-X. Ma, L. Yu, C.-Y. Xu and X. W. D. Lou. "Self-supported formation of hierarchical NiCo2O4 tetragonal microtubes with enhanced electrochemical properties". *Energy Environ. Sci.*, 9, 862–866, 2016. doi:10.1039/C5EE03772G.

[175] J.-G. Kim, D. Pugmire, D. Battaglia and M. Langell. "Analysis of the NiCo2O4 spinel surface with Auger and X-ray photoelectron spectroscopy". *Applied Surface Science*, 165(1), 70–84, 2000. ISSN 0169-4332. doi:https://doi.org/10.1016/S0169-4332(00)00378-0.

[176] Y. E. Roginskaya, O. V. Morozova, E. N. Lubnin, Y. E. Ulitina, G. V. Lopukhova and S. Trasatti. "Characterization of Bulk and Surface Composition of CoxNi1-xOy Mixed Oxides for Electrocatalysis". *Langmuir*, 13(17), 4621–4627, 1997. doi:10.1021/la9609128.

[177] J. F. Marco, J. R. Gancedo, M. Gracia, J. L. Gautier, E. I. Ríos, H. M. Palmer, C. Greaves and F. J. Berry. "Cation distribution and magnetic structure of the ferrimagnetic spinel NiCo2O4". *J. Mater. Chem.*, 11, 3087–3093, 2001. doi:10.1039/B103135J.

[178] R. Zhang, M. Liu, W. Liu and H. Wang. "Highly conductive n-type NiCo2O4-δ epitaxial thin films grown by RF sputtering". *Materials Letters*, 199, 164–167, 2017. ISSN 0167-577X. doi:https://doi.org/10.1016/j.matlet.2017.04.076.

[179] J. Son, P. Moetakef, B. Jalan, O. Bierwagen, N. Wright, R. Engel-Herbert and S. Stemmer. "Epitaxial $SrTiO_3$ films with electron mobilities exceeding 30,000 cm2 V-1s-1". *Nature Materials*, 9(6), 482–484, 2010. ISSN 1476-1122. doi:10.1038/nmat2750.

[180] C. M. Brooks, L. F. Kourkoutis, T. Heeg, J. Schubert, D. A. Muller and D. G. Schlom. "Growth of homoepitaxial SrTiO3 thin films by molecular-beam epitaxy". *Applied Physics Letters*, 94(16), 162905, 2009. doi:10.1063/1.3117365.

[181] F. Wrobel, A. F. Mark, G. Christiani, W. Sigle, H.-U. Habermeier, P. A. van Aken, G. Logvenov, B. Keimer and E. Benckiser. "Comparative study of LaNiO3/LaAlO3 heterostructures grown by pulsed laser deposition and oxide molecular beam epitaxy". *Applied Physics Letters*, 110(4), 041606, 2017. doi:10.1063/1.4975005.

[182] O. H. Seeck, C. Deiter, K. Pflaum, F. Bertam, A. Beerlink, H. Franz, J. Horbach, H. Schulte-Schrepping, B. M. Murphy, M. Greve and O. Magnussen. "The high-resolution diffraction beamline P08 at PETRA III". *Journal of Synchrotron Radiation*, 19(1), 30–38, 2012. doi:10.1107/S0909049511047236.

[183] C. Schlueter, A. Gloskovskii, K. Ederer, I. Schostak, S. Piec, I. Sarkar, Y. Matveyev, P. Lömker, M. Sing, R. Claessen, C. Wiemann, C. M. Schneider, K. Medjanik, G. Schönhense, P. Amann, A. Nilsson and W. Drube. "The new dedicated HAXPES beamline P22 at PETRAIII". *AIP Conf. Proc.*, 2054(1), 040010, 2019. doi:10.1063/1.5084611.

[184] S. Uhlenbrock, C. Scharfschwerdt, M. Neumann, G. Illing and H. J. Freund. "The influence of defects on the Ni 2p and O 1s XPS of NiO". *Journal of Physics: Condensed Matter*, 4(40), 7973–7978, 1992. doi:10.1088/0953-8984/4/40/009.

[185] M. Nydegger, G. Couderc and M. Langell. "Surface composition of $Co_xNi_{1-x}O$ solid solutions by X-ray photoelectron and Auger spectroscopies". *Applied Surface Science*, 147(1), 58–66, 1999. ISSN 0169-4332. doi:https://doi.org/10.1016/S0169-4332(99)00077-X.

[186] F. Bertram, C. Deiter, T. Schemme, S. Jentsch and J. Wollschläger. "Reordering between tetrahedral and octahedral sites in ultrathin magnetite films grown on MgO(001)". *Journal of Applied Physics*, 113(18), 184103, 2013. doi:10.1063/1.4803894.

Danksagung

Auf dem Weg durch meine Promotion haben mich viele Menschen begleitet. Ihnen möchte ich in diesem Kapitel danken.

Zunächst möchte ich mich bei allen Personen bedanken, die zum Gelingen dieser Doktorarbeit beigetragen haben. In erster Linie bei meinem Doktorvater Herrn Prof. Dr. Joachim Wollschäger, der sich immer Zeit für meine Fragen genommen hat und immer als Ansprechpartner für meine Probleme zur Verfügung stand. Ich konnte mit ihm jederzeit über die verschiedensten Themen diskutieren. Vielen Dank für das Vertrauen und die Möglichkeit diese Dissertation zu erstellen. Ein weiterer Dank gilt Herrn Dr. Karsten Küpper, für die Übernahme des Zweitgutachtens und die Hilfe bei den XAS/XMCD Daten und die damit verbundene Mutliplett-Auswertung. Außerdem sei noch Herrn Prof. Dr. Robin Steinigeweg und Dr. Monika Wesner gedankt, die sich sofort bereit erklärt haben, die Promotionskommission zu vervollständigen.

Des Weiteren möchte ich mich bei allen aktuellen und ehemaligen Mitgliedern der Arbeitsgruppe "Dünne Schichten und Grenzflächen" im Fachbereich Physik der Universität Osnabrück bedanken. Viele haben mir sowohl inhaltlich enorm geholfen, aber auch die Hilfestellung im Labor ist nicht zu verachten. Die wichtigste Hilfe war allerdings die entspannte Arbeitsatmosphäre im Büro als auch auf den ganzen Messzeiten. Insbesondere zu erwähnen sind meine langjährigen Bürokollegen Jannis Thien, Andreas Alexander und Jascha Bahlmann. Aber auch Jari Rodewald und Olga Kuschel haben mich über viele Jahre begleitet und standen mir mit ihrer Erfahrung stets bei. Auch Tobias Pohlmann und Martin Hoppe, die mich sowohl bei der Arbeit im Labor, als auch bei etlichen Synchrotronmesszeiten und der Datenauswertung unterstützt haben, sei an dieser Stelle herzlich gedankt. Ein weiterer Dank gilt Florian Bertram für die Unterstützung bei Messzeiten und Diskussionen über Messergebnisse. Ich möchte hier die Gelegenheit nutzen und insbesondere Jannis Thien für die enorme Hilfe und die unvergessliche Zeit in New York danken. Nicht zu vergessen sind unsere Techniker Gregor Steinhoff und Alexander Weißbach, die mir sowohl im Labor, als auch in privaten Gesprächen immer sehr geholfen haben. Ein ganz großer Dank an euch! Ich möchte mich auch bei Eugenia Miller für all die organisatorische Hilfe danken. Ihr alle habt dazu beigetragen, dass ich mich in der Arbeitsgruppe immer wohl gefühlt habe.

Ich danke auch der feinmechanischen Werkstatt und der Werkstatt für Elektronik der Universität Osnabrück für die Hilfen und Reperaturen während meiner Promotion. Alle Anliegen wurden immer schnell und unkompliziert gelöst.

Den wichtigsten Menschen möchte ich zum Schluss danken. Von Herzen möchte ich meinen Eltern und meiner Schwester für die jahrelange Unterstützung während des gesamten Studiums danken. Ihr habt es möglich gemacht, dass ich diesen Weg gehen konnte. Danke dafür! Der letzte und wichtigste Dank gilt meiner Frau Angelique, die all meine Launen und Abwesenheiten ertragen hat. Du hast mir den Halt gegeben meine Promotion abzuschließen und mir immer den Rücken freigehalten. Insbesondere in der stressigen Endphase meiner Promotion warst du eine wahnsinnige Stütze für mich. Ohne dich wäre das alles nicht möglich gewesen. Danke für alles!

Erklärung über die Eigenständigkeit der erbrachten wissenschaftlichen Leistung

Ich erkläre hiermit, dass ich die vorliegende Arbeit ohne unzulässige Hilfe Dritter und ohne Benutzung anderer als der angegebenen Hilfsmittel angefertigt habe. Die aus anderen Quellen direkt oder indirekt übernommenen Daten und Konzepte sind unter Angabe der Quelle gekennzeichnet.

Bei der Auswahl und Auswertung folgenden Materials haben mir die nachstehend aufgeführten Personen in der jeweils beschriebenen Weise entgeltlich / unentgeltlich geholfen.

1. .....

   .....

2. .....

   .....

3. .....

   .....

Weitere Personen waren an der inhaltlichen materiellen Erstellung der vorliegenden Arbeit nicht beteiligt. Insbesondere habe ich hierfür nicht die entgeltliche Hilfe von Vermittlungs- bzw. Beratungsdiensten (Promotionsberater oder andere Personen) in Anspruch genommen. Niemand hat von mir unmittelbar oder mittelbar geldwerte Leistungen für Arbeiten erhalten, die im Zusammenhang mit dem Inhalt der vorgelegten Dissertation stehen.

Die Arbeit wurde bisher weder im In- noch im Ausland in gleicher oder ähnlicher Form einer anderen Prüfungsbehörde vorgelegt.

....

(Ort, Datum) (Unterschrift)